

ABSTRACT

MCAFEE, TERRY RICHARD. Investigation and Control of “Sphere-Like” Buckminsterfullerene C₆₀ and “Disk-Like” Copper(II) Phthalocyanine. (Under the direction of Harald Ade and Daniel Dougherty).

Due to the growing global need for cheap, flexible, and portable electronics, numerous research groups from mechanical and electrical engineering, material science, chemistry, and physics have increasingly turned to organic electronics research over the last ~5-10 years. Largely, the focus of researchers in this growing field have sought to obtain the next record holding device, allowing a heuristic approach of trial and error to become dominant focus of research rather than a fundamental understanding. Rather than working with the latest high performance organic semiconducting materials and film processing techniques, I have chosen to investigate and control the fundamental self-assembly interactions of organic photovoltaic thin films using simplified systems. Specifically, I focus on organic photovoltaic research using two of the oldest and well studied semiconducting materials, namely “sphere-like” electron donor material Buckminsterfullerene C₆₀ and “disk-like” electron acceptor material Copper(II) Phthalocyanine. I manufactured samples using the well-known technique of physical vapor deposition using a high vacuum chamber that I designed and built to accommodate my need of precise material deposition control, with co-deposition capability. Films were characterized using microscopy and spectroscopy techniques locally at NCSU, including Atomic Force Microscopy, scanning tunneling microscopy, X-ray photoelectron spectroscopy, and Ultraviolet-visible spectroscopy, as well as at National Laboratory based synchrotron x-ray techniques, including Carbon and Nitrogen k-edge Total Electron Yield and Transmission Near Edge X-ray absorption fine

structure spectroscopy, Carbon k-edge Resonant Soft x-ray Microscopy, Resonant Soft x-ray reflectivity, and Grazing Incidence Wide-Angle X-ray scattering.

© Copyright 2015 by Terry Richard McAfee

All Rights Reserved

Investigation and Control of “Sphere-Like” Buckminsterfullerene C₆₀ and “Disk-Like”
Copper(II) Phthalocyanine

by
Terry Richard McAfee

A dissertation submitted to the Graduate Faculty of
North Carolina State University
in partial fulfillment of the
requirements for the degree of
Doctor of Philosophy

Physics

Raleigh, North Carolina

2015

APPROVED BY:

Harald Ade
Co-Chair of Advisory Committee

Daniel Dougherty
Co-Chair of Advisory Committee

Robert Riehn

Brendan O'Connor

DEDICATION

Dedicated to my family and friends.

BIOGRAPHY

Terry Richard McAfee was born July 7th, 1987 in Arcata California. He attended Gridley Unified School District for the majority of his K-12 education. He received his high school diploma in 2005 from Gridley High School. He continued his education by attending California State University, where he received a Bachelor of Science in Physics in 2010. He began his pursuit of a Ph.D in Physics in 2010 at North Carolina State University. His Ph.D research focused on morphology characterization of organic thin films related to the field of organic electronics under co-advisement by Harald Ade and Daniel Dougherty.

ACKNOWLEDGMENTS

I would like to thank everyone that has assisted me in my pursuit of a Ph.D in Physics.

Special thanks to my co-advisors Harald Ade and Daniel Dougherty, as well as my many group members.

TABLE OF CONTENTS

LIST OF TABLES	viii
LIST OF FIGURES	ix
CHAPTER 1-- Introduction.....	1
1.1 Motivation for Organic Photovoltaic Research.....	1
1.2 What are Organic Electronics?	2
1.3 History of OPV device performance.....	3
1.4 How does a photovoltaic work?	6
1.5 Steps to converting photons to electrical energy	8
1.6 Small Molecule Films grown by Organic Molecular Beam Deposition	16
1.7 How can physics contribute to the OPV community?	18
1.8 Tying it all together	19
1.9 Outline of Thesis.....	21
1.9.1 Overview	21
1.9.2 Chapter 3: Thermally induced dewetting in ultrathin C60 films on Copper Phthalocyanine	22
1.9.3 Chapter 4: Toward Single-Crystal Hybrid-Carbon Electronics: Impact of Graphene Substrate Defect Density on Copper Phthalocyanine Film Growth.....	23
1.9.4 Chapter 5: Layer-by-Layer Growth of Crystalline C60 Films on Flat-lying Copper Phthalocyanine.....	23
1.9.5 Chapter 6: Morphological, optical, and electronic properties of three distinct crystal orientations present in a Beta CuPc thin film	24
CHAPTER 2-- Experimental Methods	26
2.1 Sample Fabrication Techniques.....	26
2.2 Organic Molecular Beam Deposition Chamber	27
2.3 Atomic Force Microscopy	32
2.4 Grazing Incidence Wide-Angle X-ray Scattering	35

2.5 Total Electron Yield Near-Edge X-ray Absorption Fine Structure	38
CHAPTER 3-- Thermally-Induced Dewetting in Ultra-Thin C₆₀ films on Copper Phthalocyanine	41
3.1 Preface	41
3.2 Abstract	41
3.3 Introduction	42
3.4 Experimental Methods.....	44
3.5 Results and Discussion	46
3.5A AFM Measurements of Film Morphology	46
3.5C Discussion of C ₆₀ Dewetting.....	51
3.6 Summary and Conclusions	55
3.7 Acknowledgements.....	56
3.8 Associated Content	56
CHAPTER 4-- Towards Single Crystal Hybrid-Carbon Electronics: Impact of Graphene Substrate Defect Density on Copper Phthalocyanine Film Growth	57
4.1 Preface	57
4.2 Abstract	57
4.3 Introduction	60
4.4 Results	63
4.4A CuPc Films on Graphene/SiC(0001).....	63
4.4B CuPc Films on HOPG	67
4.5 Discussion.....	71
4.5A Mechanism of Substrate Controlled CuPc Film Growth	71
4.5B Implications for Organic Photovoltaics.....	74
4.6 Conclusion.....	75
4.7 Experimental Methods.....	77
4.8 Funding	79
CHAPTER 5-- Layer-by-Layer Growth of Crystalline C₆₀ Films on Flat-Lying Copper Phthalocyanine	80
5.1 Preface	80

5.2 Abstract	80
5.3 Introduction	81
5.4 Experimental Methods.....	84
5.5 Results	85
5.6 Discussion	89
5.7 Summary and Conclusions	92
5.8 Acknowledgements.....	93
CHAPTER 6-- Morphological, Optical, and Electronic properties of three distinct crystal orientations present in a Beta CuPc thin film.....	94
6.1 Preface	94
6.2 Abstract	94
6.3 Introduction	95
6.4 Experimental Methods.....	97
6.5 Results	99
6.6 Discussion	104
6.7 Summary and Conclusions	107
6.8 Acknowledgements.....	108
CHAPTER 7-- Conclusions and Outlook	109
REFERENCES.....	111
APPENDICES	128
Appendix A	129
Simulating GIWAXS Peak Locations	129
Appendix B	133
Quantitative correlation of TEY NEXAFS signal composition with C₆₀ dewetting measured by AFM.....	133

LIST OF TABLES

Table B1. Comparison of calculated and measured CuPc component of TEY NEXAFS signal.....	130
---	------------

LIST OF FIGURES

- Figure 1.1 Solar Cell Performance.** Illustration of the relationship between the power conversion efficiency and the current, as a function of voltage, in a photovoltaic cell..... 8
- Figure 1.2 Photoconversion Steps.** Energy band diagram (left) and spatial schematic (right) illustrating the steps to convert photons into electrical energy in an OPV device. A bilayer architecture was chosen for simplicity. 10
- Figure 1.3 “Comb-like” morphology.** Example of a morphology theorized to achieve High OPV PCE. Red = Acceptor, Blue = donor material. Width of domain strips set to match the exciton diffusion length..... 16
- Figure 2.1 External view of chamber shown in (a). Internal view of chamber is shown in (b), as seen through the View Port labeled in (a). The hot-filament ionization gauge (Ion Gauge) measure the pressure in the OMBD chamber in the range of $\sim 10^{-4} - 10^{-10}$ torr range. Quartz Crystal Microbalance (QCM) monitors the deposition rate by measuring the mass adsorbed. A shutter is essential for OMBD because it allows experimenter to stabilize the deposition rate prior to film growth. 29**
- Figure 2.2 Deposition Uniformity.** Illustrates of the deposition uniformity of a crucible modeled as three point sources. 30
- Figure 2.3 Schematic of Atomic Force Microscopy primary components.** Motion in the plane of the sample is controlled by X and Y piezo motors on the sample stage. Motion perpendicular to the plane of the sample is achieved by the Z piezo motor attached to the cantilever. The cantilever height and oscillations are measure by reflecting a laser off the cantilever. Using the z-height and cantilever oscillation dampening as inputs, a feedback loop is used measure the height of the film as the cantilever raster across the sample. 35
- Figure 2.4 Grazing Incidence Wide-Angle X-ray Scattering.** Schematic of GIWAXS setup shown in (a). Figure (b) is an illustration of momentum transfer vector, q , and separated in its in-plane component, q_{xy} , and out-of-plane component, q_z 37
- Figure 2.5 Total Electron Yield Near Edge X-ray Absorption Fine Structure.** Schematic of TEY NEXAFS experimental setup is shown in figure (a), where the x-ray beam, sample, and sample plate are in a high vacuum enclosure. Figure (b) illustrates the energy band diagram for x-ray absorption and Auger decay processes occurring during TEY NEXAFS measurements. 39
- Figure 3.1 AFM Time Series of C_{60} Dewetting.** $2 \mu\text{m} \times 2 \mu\text{m}$ AFM images collected in non-contact mode of nominal $2 \text{ nm } C_{60} / 10 \text{ nm CuPc} / \text{Si}(100)$, a) As-Grown and annealed at $105 \text{ }^\circ\text{C}$ for times of:, b) 30 minutes, c) 5 hours, and d) 48 hours..... 47

- Figure 3.2 AFM Temperature Series of C₆₀ Dewetting.** 2 μm x 2 μm AFM images of a 2.2 nm C₆₀ film on CuPc a) As-grown; b) annealed at 100 C for 30 minutes; and c) annealed at 150 C for 30 minutes. 48
- Figure 3.3 Surface Composition.** TEY NEXAFS spectra of the Carbon K-edge in the region of highest absorption contrast between CuPc and C₆₀. The results of component fitting are shown in the legend in percentage of CuPc. 50
- Figure 3.4 C₆₀ Cluster Statistics.** (a) C₆₀ cluster Height vs FWHM for 5 Hour and 48 Hour annealing with least squares linear fit (b) Normalized histogram of cluster heights for time dependent annealing at 105 °C and 30 min annealing at 150 °C (c) Normalized histogram of cluster FWHM for same conditions as in part b). 52
- Figure 4.1 Brickstone CuPc Molecular Planes.** Illustration of CuPc molecular plane tilt angles in the Brickstone crystal with respect to the (012) and (112) crystal planes. As viewed parallel to the (012) and (112) planes (a), (012) and molecule plane (b), (112) and molecule plane (c). Perspective view of CuPc molecule packing along the (012) and (112) planes are shown in (d) without indicating the molecule plane. 59
- Figure 4.2 AFM of CuPc / Graphene / SiC.** 2 μm x 2 μm AFM scan on the same 20 nm CuPc / G / SiC sample at locations separated by less than a centimeter, showing regions with large, ~10-300 nm, crystals (a) and small, ~10-50 nm, crystals (b). 64
- Figure 4.3 Calculated diffraction peaks for CuPc Brickstone (012) and (112) (a).** GIWAXS data, with excluded wedge correction, for 80 nm CuPc/G/SiC with in plane rotation of the sample by (b) 10.0 deg, (c) 3.0 deg, (d) 0.0 deg showing relative peak intensity variation for both the (012) and (112) brickstone reflections. 65
- Figure 4.4 Plot of computed diffraction peak locations for CuPc Brickstone (012) (a) and (112) (b) orientations.** GIWAXS data, with excluded wedge correction, for (c) 5 nm, (d) 25 nm, (e) 80 nm, and (f) 250 nm CuPc on HOPG. 68
- Figure 5.1 Thickness Dependent AFM of C₆₀ / CuPc / HOPG.** 2 μm x 2 μm AFM on a) 5.5 nm C₆₀ / 25 nm CuPc / HOPG, b) 30 nm C₆₀ / 25 nm CuPc / HOPG, c) 30 nm C₆₀ / 150 nm CuPc / HOPG, d) 150 nm C₆₀ / 25 nm CuPc / HOPG 86
- Figure 5.2 GIWAXS acquired at 0.15 Deg incidence angle on a) 5.5 nm C₆₀ / 25 nm CuPc / HOPG, b) 30 nm C₆₀ / 25 nm CuPc / HOPG, c) 30 nm C₆₀ / 150 nm CuPc / HOPG, d) 150 nm C₆₀ / 25 nm CuPc / HOPG. 87**
- Figure 5.3 Calculated GIWAXS scattering peak locations for CuPc Brickstone (0 1 - 2) and (1 1 2) crystals [Left], and C₆₀ FCC (1 1 1) and (1 2 2) [Right] 88**
- Figure 5.4 Thermal Stability.** 2 μm x 2 μm AFM data on both a) As-Grown and b) post-annealing at 150° C for 24 hrs, and c) GIWAXS data (post-annealing at 150° C for 24 hrs), all acquired on the same 30 nm C₆₀ / 25 nm CuPc / HOPG sample. 89

Figure 6.1 GIWAXS on Beta CuPc Thin Film. GIWAXS data, with forbidden wedge correction, on 100 nm CuPc / Glass, annealed at 320° C for 3 hours. Simulated GIWAXS scattering peak locations for (1 0 1), (-1 0 5), and (-5 0 2) orientations of beta Herringbone CuPc is overplotted. 100

Figure 6.2 Beta CuPc Molecular Planes. Illustration of molecular arrangement of CuPc molecules in a beta herringbone crystal, as viewed along the b-axis. The parallelogram shows the unit cell, with a thin red and thin blue line showing the a-axis and c-axis of the crystal, respectively. The (1 0 1), (-1 0 5), and (-5 0 2) crystal planes, and relative angles between these planes, are overplotted. 101

Figure 6.3 KPFM of Beta CuPc Thin Film. AFM data, shown in part (a), collected simultaneous with KPFM, shown in part (b), on 100 nm CuPc / Glass, annealed at 320° C for 3 hours. In agreement with the GIWAXS data, three distinct topographies are identified from the AFM. The average surface potential for these domains is shown in part (c), indicating no measureable difference between the three crystal orientations. 102

Figure 6.4 Visual Light Spectroscopy. Visual Light Microscope on 100 nm CuPc / Glass, annealed at 320° C for 3 hours, with location where micro Uv-Vis spectra was collected for (a) Small Rough, (b) Big Rough, and (c) Small Flat domains. Uv-Visible spectroscopy spectra shown in (d) on locations indicated in (a),(b), and (c), as well as standard, bulk average, spectra on the As-Grown and 320° C annealed films. 104

Figure B1 Illustration of Bilayer Film. Illustration of assumed sample geometry in regions not occupied by large dewetted C₆₀ mounds 135

CHAPTER 1

Introduction

1.1 Motivation for Organic Photovoltaic Research

As the energy demands of the world grow, and we deplete our reserves of non-renewable resources, sources of renewable and sustainable energy are becoming increasingly important. Solar energy is one such renewable energy source, but the high manufacturing cost and scarcity of necessary elements of traditional condensed matter solar panels makes them unsuitable for our current and future needs.¹ Organic photovoltaics (OPVs), however, show promise for not only being cheap and primarily composed of earth abundant elements, but are already known to be light-weight, flexible, and easily transportable. Device power conversion efficiencies (PCE) of OPVs have increased by roughly an order of magnitude in the last 20 years, with the current record at 11.5%,² making them a promising candidate to supply our energy needs. Several manufacturing options show promise in achieving economy of scale, including slot-die printing,³ blade coating,⁴ and vapor deposition,⁵ which can be easily integrated into mass production techniques such as roll-to-roll processing.^{1, 5} The rapid increase of PCE, especially advances past the 10% benchmark, is largely due to individual and collaborative research efforts made by mechanical and electrical engineers, material scientists, chemists, and physicists. Specialization is required for advancement of

understanding of each aspect of an OPV. I have chosen to focus on morphology characterization and control.

1.2 What are Organic Electronics?

The fundamental difference between a traditional inorganic solar cell and an organic solar cell is the creation of free charges after photo absorption. Unlike traditional condensed matter solar cells where an absorbed photon directly results in separated charges, an absorbed photon in an OPV device results in a relatively tightly bound electron-hole pair, known as an exciton. The binding energy of an exciton in an OPV is $\sim 0.25 \text{ eV}^6$, making it too strongly bound to be dissociated by the internal electric fields. Thus, the exciton can only be separated into free charges at defect/trap sites (which is detrimental to solar cell performance), or preferably at an interface between two materials. If such an interface has electronic states with sufficient band offset energy to overcome the binding energy of the exciton, charges can be separated. During the dissociation process, the primary photon absorber typically ‘donates’ an electron to the second material, so this interface is typically called a donor/acceptor (D/A) interface.

The need for a D/A interface in an OPV to split the exciton into free charges makes efficient charge generation nontrivial. Typically, an active layer thickness of $\sim 100 \text{ nm}$ is required to absorb enough photons, but the exciton diffusion length is only $\sim 10 \text{ nm}$. This means that in a bilayer OPV, which is analogous to the inorganic p / n junction solar cell, only $\sim 20\%$ of excitons are able to reach the D/A interface to be split into free charges. To

increase the number of excitons that reach the D/A interface, either the exciton diffusion length must increase, or the path length of the exciton to the D/A interface must be decreased. Although the exciton diffusion length can be manipulated in the range of ~1-30 nm by choice of materials⁷, crystallinity⁸, molecular orientation⁹, etc., the path length of the exciton to the D/A interface can be drastically reduced by abandoning the bilayer device architecture in favor of a mixed or bulk heterojunction (BHJ) morphology¹⁰.

Due to the short exciton lifetime in OPV materials, a bulk heterojunction (BHJ) device morphology is used to create a bi-continuous network of (ideally) ~10-50 nm D/A domains, which allows the exciton to reach the D/A interface and dissociate into free charges before decaying. The morphology of the OPV device is thus a key parameter that strongly affects its overall performance.¹ Organic Molecular Beam Epitaxy (OMBD) can achieve a BHJ type morphology by co-deposition of the donor and acceptor materials followed by thermal annealing¹¹. To create a BHJ by solution processing, donor and acceptor materials are dissolved into a common solvent and cast onto the substrate. The resulting BHJ morphology is a result of the self-assembly of the donor and acceptor materials during the drying process, and is heavily influenced by the type of solvent and processing conditions.

1.3 History of OPV device performance

OPVs were demonstrated to be a possible energy source in 1986 when Tang achieved a 0.95 % PCE with an OMBD grown bilayer device using CuPc as the electron donor material and a perylene tetracarboxylic derivative (PV) as the electron acceptor material¹².

There was little improvement in OPV performance from 1986 until ~2000, at which point there have been new records every year. Although the performance was not record breaking, the discovery/invention of the Bulk Heterojunction in 1995 by Heeger, et. al¹³ allowed solution processing to become an alternative to OMBD for organic thin film device creation. A few important benchmarks in the evolution of OPV devices are worth mentioning. In 2001 Peumans and Forrest made a major leap past the ~1% PCE benchmark with a OMBD grown CuPc / C60 bilayer device with a 3.6 % PCE¹⁴. Aernouts, Mertens, et. al. achieved 3.1% in 2002 using solution processed MDMO-PPV:PCMB in a BHJ device architecture¹⁵. The fact that these two devices both achieved above 3%, yet are made of different materials, and completely different thin film creation techniques, showed a glimpse into the vast parameter space that could be investigated to further improve the PCE in OPVs. It was around this time that publications in the OPV field begin to pick up, with many researchers competing to be the new record holder.

A notable landmark in the importance of optimization was in 2003 when Sariciftci, et. al. published a PCE increase in P3HT:PCBM based BHJ from 2.5% to 3.5% by adding a thermal annealing step post device production.¹⁶ This result, in combination with related advances in OPV fabrication/optimization techniques in the early to mid 2000's, resulted in considerable research on P3HT:PCBM BHJs, allowing many researchers to consider it the "fruit fly" of the OPV community. Numerous research groups employed various optimization experiments using P3HT:PCBM OPVs in attempts to be the next PCE record

holder, leading to Heeger, et. al. reaching 5% PCE in 2005¹⁷. Only slight increases in PCE for P3HT:PCBM have been reported since then.

Just as many researchers flocked to optimization of solution processed P3HT:PCBM OPVs in the early 2000's, optimization of OMBD based OPVs also gained attention. Forrest, et. al. also achieved a 5.0% PCE device¹⁸ by modification of the CuPc / C₆₀ bilayer device into a planar-mixed heterojunction, where a mixed layer of CuPc and C₆₀ is added between the pure CuPc and C₆₀ layers of a bilayer device. Similar to the advantages of the BHJ, the mixed CuPc:C₆₀ layer dramatically increases the interfacial area between CuPc and C₆₀ domains, which increases the probability of an exciton reaching a D/A interface for dissociation before decaying.

By optimizing of CuPc:C₆₀ and P3HT:PCBM in the early 2000's, researchers were able to nearly double the PCE of these material systems. Since then, however, there have been very little improvements to the PCE in those material systems. This made it clear that although optimization is crucial for achieving high performance OPVs, alternative organic semiconducting materials were needed for OPVs to reach the ~10% PCE benchmark thought to be needed for them to be a practical alternative energy source.

Many chemist and chemical engineers began developing new donor and acceptor materials for OPVs. In 2012, Seth Darling, et. al., achieved 6.8% PCE by “judicious Molecular Design and Device Optimization”¹⁹ of a new donor material they synthesized called DPDCPB, which has a substructure of Donor-Acceptor-Acceptor groups within the molecule. Since 2012, many new solution processed small molecule materials, comprised of

combinations of donor and acceptor units, have been synthesized and characterized. One such material in 2013, called SMPV1, achieved a single junction OPV with a certified PCE of 8.02 %, and uncertified tandem OPV with 10.1 % PCE²⁰. A very recent publication reported a certified PCE of 10.10 % using a single junction, solution processed, small molecule OPV based on oligothiophene²¹.

The performance of OPVs has continuously increased over the last ~15 years through a combination of synthesizing new organic semiconducting materials, and by optimization of processing techniques of existing materials. This has been achieved largely due to the gain in collective understanding of the OPV community, namely, how the choice in materials and processing conditions impact the optoelectronic properties of the active layer. Overall, the gain in OPV performance is due to a deeper understanding of the processes occurring within the active layer of an OPV, allowing for the intelligent design of materials and processing techniques.

1.4 How does a photovoltaic work?

The key metric for evaluating the performance of an OPV is the Power Conversion Efficiency (PCE). The PCE is a measure of the power output of the solar cell as a percent of incident solar power. PCE can be expressed by the product of the short circuit current (J_{sc}), open circuit voltage (V_{oc}), and the fill factor (FF), divided by incident solar power per area, shown in equation 1.

$$(eq.1) \quad PCE = \frac{J_{sc} * V_{oc} * FF}{Incident\ solar\ power\ per\ area}$$

Numerical values for the J_{sc} , V_{oc} , FF, and PCE for a photovoltaic device can be determined by measuring the current output of the cell as a function of the voltage difference between the electrodes, as illustrated in figure 1. The device can be operated anywhere in Quadrant IV, while quadrants I and III must be measured with an applied bias. The J_{sc} is the measure of the current density out of the device when the cathode and anode are held at the same potential. The value of the J_{sc} in a solar cell is primarily dependent on the number of photons absorbed in the active layer, resulting in excitons which can be split into free charge carriers. The V_{oc} is the maximum possible voltage output of the device under operating conditions, and is the voltage difference between the cathode and anode when the device is under illumination and there is no current flowing. When the cell is in an open circuit condition, meaning there is no net charge flow through the device, free charge carriers self-arrange within the active layer to cancel the electric field, resulting in no internal electric field.

If we consider sweeping an applied bias in between the J_{sc} and V_{oc} conditions, we see that the current decreases as the bias increases. The reduction in the current is due to recombination losses. The reduced electric field slows down the rate charges transport to the electrodes, increasing the free charge carrier density and thus the probability of recombination. The FF is the ratio of the actual maximum power output of the cell per area divided by the product of the J_{sc} and V_{oc} . In the ideal case (FF=1), charge extraction is so efficient that lowering the electric field results in a negligible increase in recombination, allowing the current to remain near the J_{sc} value as the bias approaches the V_{oc} . In reality,

FF is often degraded by low intrinsic carrier mobility, charge traps, or morphological dead ends that prevent efficient charge extraction.

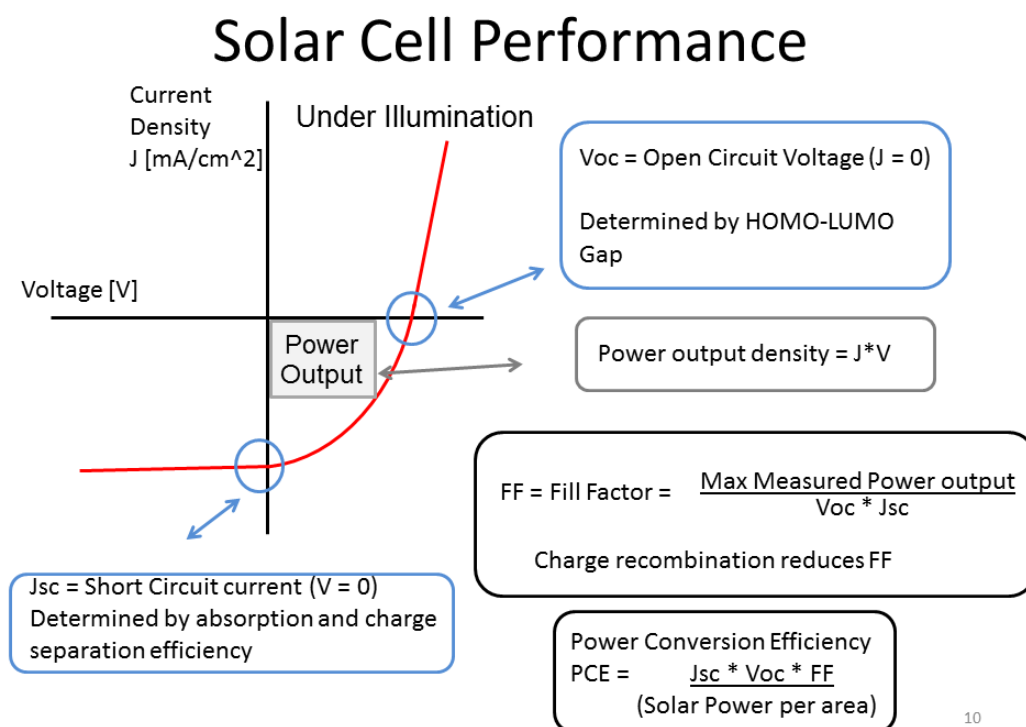


Figure 1.1 Solar Cell Performance. Illustration of the relationship between the power conversion efficiency and the current, as a function of voltage, in a photovoltaic cell.

1.5 Steps to converting photons to electrical energy

To understand the process of converting photons to electrical energy in a photovoltaic, it can be useful to consider each step in both energy space as well as real space. Figure 1.2 illustrates each step in the photo-conversion process in energy space diagram on the left hand side with the corresponding real space diagram on the right hand side. Figure

1.2 (a) and (b) show the system in equilibrium in dark conditions without photo excitations. Both the donor and acceptor materials have a two energy bands responsible for the conduction of charges. The higher energy band is referred to as the Lowest Unoccupied Molecular Orbital (LUMO), which is analogous to the conduction band in a conventional solar cell. The lower energy band is referred to as the Highest Occupied Molecular Orbital (HOMO), which is analogous to the valence band in a conventional solar cell. The energy difference between the HOMO and LUMO, or bandgap, is intrinsic to the material and is directly correlated to the onset of optical absorption. The relative position of the energy bands with respect to vacuum depends on the work function of the material.

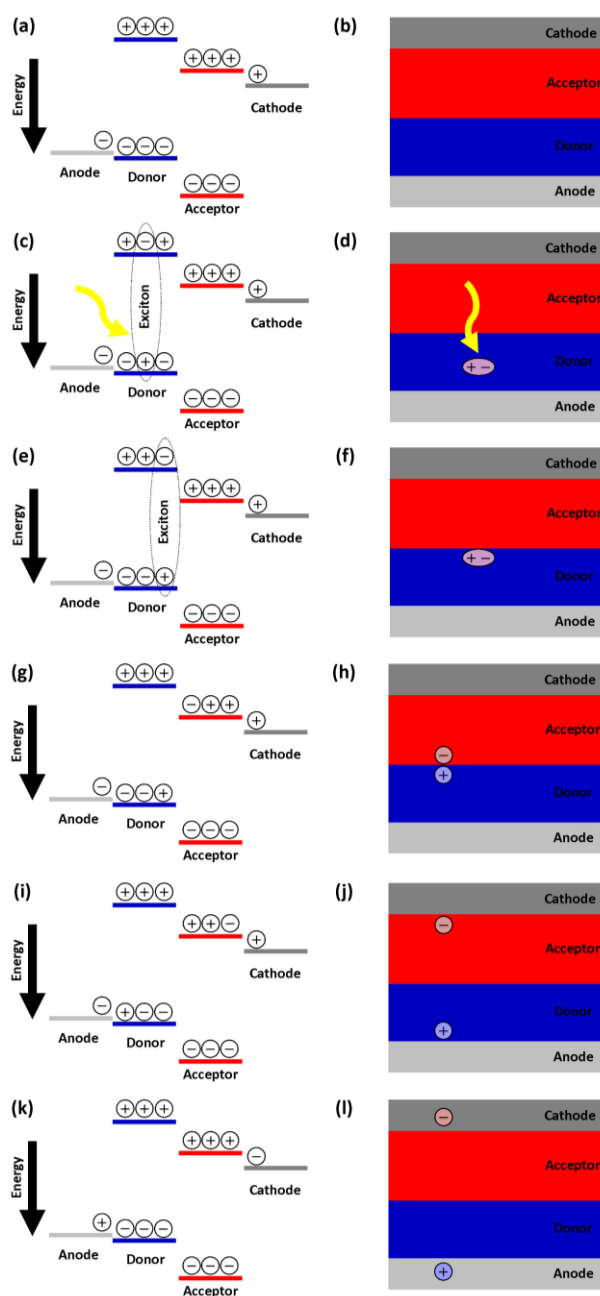


Figure 1.2 Photoconversion Steps. Energy band diagram (left) and spatial schematic (right) illustrating the steps to convert photons into electrical energy in an OPV device. A bilayer architecture was chosen for simplicity.

The first step in harvesting solar energy is to absorb photons in the active layer of the device, shown in figure 1.2 (c) and (d). The absorbed photon creates an exciton in the active layer which must then diffuse to a D / A interface, shown in figure 1.2 (e) and (f). The energy band offset between the donor and acceptor material provides the energy to separate the exciton into free charges, shown in figure 1.2 (g) and (h). Once the exciton is split into free charges, the electron(hole) must transport through the active layer to the anode(cathode), shown in figure 1.2 (i) and (j). The last step is for the free charge to transfer from the active layer to the electrode, shown in figure (k) and (l).

The illustration of the photo-conversion process shown in figure 1.2 is an overview, and skips the complexity of each step. Trap states, charge transfer states, band bending, and higher energy unoccupied states are not included. The complexity of exciton dissociation at the D/A interface is one aspect of OPVs that is still not well understood. Prior to the creation of free charges at the D/A interface, the exciton is thought to first transfer to intermediate states such as charge transfer states or by formation of polar-pairs. Recombination of charges is a major loss mechanism. Recombination prior to the creation of free charges is referred to as geminate recombination, while recombination of free charges is referred to as bimolecular recombination.

The efficiency of each of the individual steps in the photo-conversion process all contribute to the PCE of the OPV. Since the output of one step is the input for the next step in the photo conversion process, the PCE of an OPV can be dramatically reduced by inefficiency in any one of the steps. The maximum achievable J_{sc} and V_{oc} are intrinsic to the

bandgap of the donor and acceptor materials chosen. The size of the bandgap determines the minimum photo energy which can be absorbed by that material. By integrating the absorption profile of the material with the solar spectrum, the number of absorption events can be determined. The maximum achievable J_{sc} is thus fundamentally limited by the bandgap of the material since absorption of photons is the first step in producing a current. The maximum achievable V_{oc} is determined by the energy difference between the ionization potential of the donor (IP_D) and electron affinity of the acceptor material, (EA_A) less the binding energy of the bound electron-hole geminate pair following charge transfer, as shown in equation 2²². Where q is the charge of an electron, ϵ_0 is the vacuum permittivity, ϵ_r is the relative dielectric constant of the bulk organic material, and r is the separation distance of the electron and hole directly following exciton dissociation.

$$(eq. 2) V_{OC} = (IP_D - EA_A - \frac{q^2}{4\pi\epsilon_0\epsilon_r r})/q$$

Ideally, every photon that enters the active layer is absorbed and creates an exciton. The primary influence on what percentage of incident photons is absorbed is the thickness of the active layer. The specific thickness required depends of the choice of materials and the molecular orientation of the materials within the active layer, but is typically 100 nm or more for organic materials. The majority of organic semiconductors have anisotropic light absorption due to the orientation of orbitals within the molecule. Due to the alignment of the transition dipole moment in organic molecules, typically the absorption is highest when the polarization of the incident photons is perpendicular to the Pi-Pi stacking direction of the molecule.

The next limiting step is what percentage of the generated excitons result in free charges. Once created, the exciton can either decay by radiative or non-radiative processes or preferably be dissociated into free charge carriers. The binding energy barrier of the exciton can be overcome, allowing dissociation, by either an electric field or by transferring one of the charge carriers to a lower energy state. Lower energy states occur at an interface between two materials or at locations with defects or impurities within a homomaterial.

The internal electric field within an OPV is not strong enough to dissociate excitons due to their high binding energy. Dissociation at an impurity or defect within a homomaterial results in one of the charge carriers being spatially trapped since the energy band it is in is localized at the site of the defect or impurity. Therefore, in order to produce a free electron and hole which both have energy pathways to the electrodes, the exciton must be dissociated at the D / A interface. Since the exciton diffusion length is ~10 nm, the best way to get the exciton to the D / A interface before decaying is to have it generated within 10 nm of the D / A interface. Once the electron(hole) is a free charge in the acceptor(donor) material, it must transport through the acceptor(donor) material to the anode(cathode) without becoming trapped or recombining with a free hole(electron). The existence of a continuous pathway to the electrodes is trivial for a bilayer device, but is often problematic with BHJ devices. Once the charge reaches the electrode interface, it must transfer to the electrode. Nearly all high PCE OPVs not include electron and hole blocking layers between the active layer and the electrodes. The blocking layers only provide energy states for either the electron or the hole, allowing only the desired charge carriers to reach each electrode.

The probability of a free electron(hole) encountering a free hole(electron) and recombining is directly related to the density of free charge carriers in the active layer. Since you do not want to decrease the rate free charges are being created, the only beneficial way to reduce the density of free charge carriers is to extract the charges as quickly as possible. To extract charges more rapidly, either the path length to the electrodes must decrease or the transport velocity must increase. Reducing the path length to the electrodes is not practical since it would require reducing the active layer thickness resulting in less light absorption. The transport velocity is determined by the charge carrier mobility of the material and the strength of the electric field. The charge carrier mobility is determined primarily by the intrinsic properties of the organic semiconducting material chosen as well as the morphology within that material. Due to increased orbital overlap, charge transport between molecules is fastest in the Pi-Pi stacking direction. The presence of grain boundaries and/or molecular disorder within the material induces trap sites and/or band bending which can greatly inhibit charge transfer.

By manipulation of the active layer morphology, the efficiency of any one step can be nearly perfect, but results in unacceptable losses in the other steps. For example, the active layer thickness can be increased so that nearly every photon entering the active layer is absorbed, but this necessitates an increase in the path length the free charges must travel before charge extraction, leading to increased recombination and a lower current. Alternatively, having an active layer that is only a monolayer thick of each material would ensure that every exciton would reach the D / A interface since the entirety of the active layer

is the D / A interface. The obvious issue here is that very few excitons are created since very few photons can be absorbed in two monolayers of organic materials.

By consideration of the morphological needs of the various steps in the photo conversion process, we can make an educated guess as to what morphology, if achieved, would provide the maximum possible PCE for an OPV system. An interdigitated “comb-like” morphology, shown in Figure 1.3, is thus thought to be one possible morphology to achieve peak OPV PCE. The width of the domains would be the size of the exciton diffusion length. This morphology would potentially allow all excitons to reach the D / A domain as well as providing continuous pathways for free charge carriers to reach the electrodes. The thickness would then be optimized to balance efficient light absorption with recombination losses. To control film morphology approximating the structure shown in figure 1.3, we need to pay careful attention to the interface creation in donor-acceptor materials. This thesis will use organic molecular beam deposition to create model donor-acceptor interfaces that allow new insights into structure, morphology and photovoltaic function.

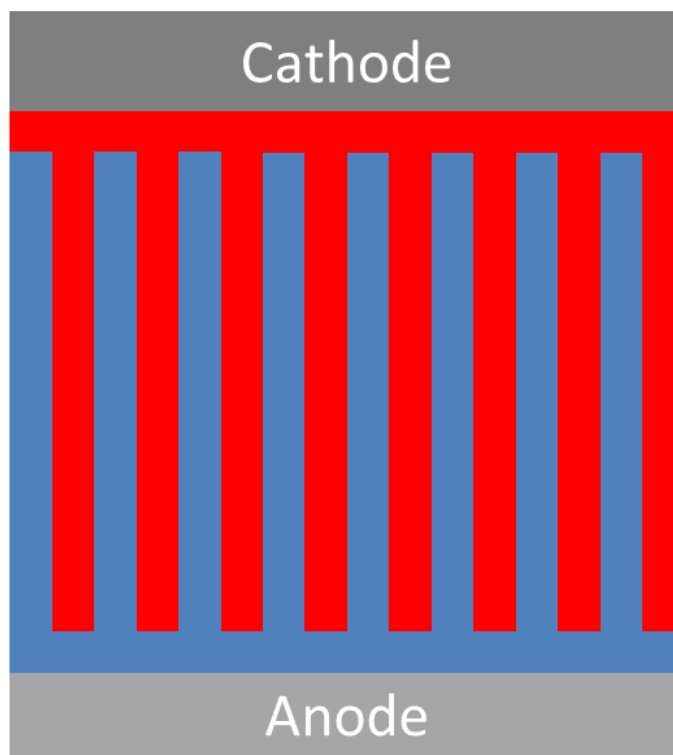


Figure 1.3 “Comb-like” morphology. Example of a morphology theorized to achieve High OPV PCE. Red = Acceptor, Blue = donor material. Width of domain strips set to match the exciton diffusion length.

1.6 Small Molecule Films grown by Organic Molecular Beam Deposition

Similar to liquid/surface contact angle measurements, the surface and interfacial energy relationships are the primary properties governing the film growth morphology. When the molecule-substrate interaction dominates the energetics in the system, the film will exhibit a layer-by-layer, or Frank-van-der-Merwe, growth mode. In contrast, if the molecule-molecule energetics far outweighs the molecule-substrate interactions, a Vollmer-Weber growth mode occurs, where 3D island growth starts with the first monolayer. A third growth

mode known as Stranski-Krastanov, exhibits a transition from uniform film growth in the first monolayer(s) to 3D island growth.

Unlike liquid/surface contact angle measurements, the energetics of a given organic material often cannot be described by a single numerical value. Asymmetry in individual molecules leads to non-negligible variation in interaction energies as a function of molecular orientation. This leads to orientation dependent energetics both at the film-substrate interface as well as the molecule-molecule interactions within the film. For example, molecules may preferentially adopt either a face-on or edge-on orientation in the first monolayer to minimize the film-substrate interfacial energy, but switch orientation in subsequent layers to minimize the molecule-molecule interactions. The molecule-molecule interactions within the film are further complicated by crystallization. Depending on the material(s), substrate, and growth parameters used, multiple crystal structures and/or crystal orientations may be induced in the film, each with different energies of formation.

Since film growth is an inherently non-equilibrium process, knowing the preferred morphology in static equilibrium is not enough to determine the actual morphology of a film growth by OMBD. In particular, the deposition rate and substrate temperature can have a dramatic impact on resultant film morphology. The deposition rate essentially determines how much time a molecule, or layer of molecules, arriving at the film surface have to self-arrange before additional molecules arrive. Higher deposition rates thus increases disorder within the film, typically resulting in poorer crystalline order and increased surface roughness. The substrate temperature determines how much energy the molecules have to

rearrange themselves on the surface. At low temperatures, molecules do not have very much energy available to rearrange, causing them to become trapped in a local, quasi-stable, low energy configuration. Higher substrate temperatures allow molecules to have more energy to diffuse across the surface and overcome local energy barriers, significantly increasing the chances of a molecule to reach its lowest energy configuration.

The parameters described above are intended to highlight the principle mechanisms involved in film formation, and is in no way a complete summary. Stress/strain relationships, vibrational and rotational degrees of freedom within a molecule, and epitaxial growth conditions, for example, may also have a significant impact on film formation.

1.7 How can physics contribute to the OPV community?

Although intimately related, the continual PCE increases in OPV devices over the last ~15 years can be attributed to two primary research tracks: 1) optimization of known OPV D/A material systems *via* film processing procedures, and 2) the development of new organic semiconducting materials. Unfortunately, there is no practical limit to the number of possibilities for researchers to consider for new materials as well as for the optimization of the materials.

Given that semi-infinite parameter space that can be pursued to achieve high PCE OPVs, it is imperative to narrow down the possibilities researchers must investigate. By gaining a deeper understanding of the opto-electronic processes that occur in an OPV, researchers can make educated decisions about what materials and processing conditions

have the potential to achieve higher PCEs. As described above, there are 5 basic steps which must occur for a photovoltaic device to convert a photon into electrical energy. The sequential nature of the photo conversion process means that inefficiency at any one step necessarily results in inefficiency of the entire cell. It is thus of great benefit to determine which process is limiting the performance of the device, and how the efficiency of that process can be improved.

High performance OPVs often exhibit similar morphological characteristics such as crystallinity, domain size, domain purity, and molecular orientation, regardless of the means used to produce the optimal morphology. This points out that the various methods of optimization *via* processing conditions are non-additive. For example, similar performance can be obtained by either using a solvent additive such as DIO or by thermal annealing, but using both the DIO additive and thermal annealing results in a poorly performing device.²³

Although theoretical predictions²⁴ combined with heuristic trial and error methods have provided many advances to the performance of OPVs, the use of techniques, such as TEM,²⁵ AFM,²⁶ SANS,²⁷ GIWAXS,²⁸ and R-SoXS²⁹ to characterize the morphology OPV devices provides critical insight into what properties allow specific combinations of material selection and processing conditions to make a better device

1.8 Tying it all together

The majority of OPV research is driven by the end goal of finding a cheap alternative energy source. The practical benefits of achieving high performance OPVs puts the

emphasis of research on the improvement of the PCE. Researchers from not only academia have flocked to OPV research, but from national laboratories and industry as well. Due to the variety of challenges which need in-depth research understanding, scientists with different specialties are needed, particularly mechanical and electrical engineers, material scientists, chemists, and physicists.

The interdependence of the morphology on each step of the photo conversion process makes it nearly impossible for the efficiency of any one step to approach unity without causing the efficiency of the other steps to decrease. By optimization of the morphology, a balance between the efficiency of each step can be found to maximize the resulting PCE of the OPV. To accomplish this, we must thoroughly understand how the morphology impacts each step in the photo conversion process.

The growing need, as well as the monetary benefits, of finding a cheap alternative energy source have led to a breadth of OPV funding and research worldwide. The goal of research on OPV is primarily focused on achieving the end goal, a cheap OPV with high PCE, regardless of the methods used. If a researcher produces a new OPV with record PCE, the device fabrication method alone merits publication, even without insight as to why it performs better. In this context, it doesn't matter if the end goal is achieved by intelligent design through a deep understanding or by brute force with trial and error. In practice, OPV device researchers use the existing knowledge and understanding of the community to guide which parameters are worth experimental investigating.

It can be beneficial for the OPV researcher to decide whether the primary impact of their work contributes to understanding how to make high PCE devices or to actually produce a new PCE record device. As a physicist working in the organic electronics community, I am best suited to contribute to the collective fundamental understanding of the mechanisms that impact the PCE.

1.9 Outline of Thesis

1.9.1 Overview

When struggling to solve a complexed problem, it is often useful to solve a simplified version of the problem. By understanding the simplified problem in depth, the insight gained can often assist with solving the more complexed problem. For example, a common classical mechanics problem is to solve for the kinematics of a 2-stage rocket. If a student can't figure out the 2-stage rocket, then it might be suggested that they solve for the kinematics of a 1-stage rocket first. Similarly, insight into the performance of a BHJ device can be gained from a deeper understanding of a bilayer device. For example, the well-defined D/A interface in a bilayer device would likely be better suited for understanding the impact of molecular orientation on exciton dissociation rather than in a BHJ.

In an effort to focus my research on advancing the understanding of the fundamental processes that occur within a OPV device, I have chosen to study pure and bilayer films of CuPc and C60 grown by OMBD. Of the many choices of organic donor and acceptor materials available, CuPc and C60 are not only two of the oldest and most well studied donor

and acceptor materials to date, but are also highly symmetric. Considering mathematicians and physicists often model a complexed shape as a superposition of spheres, rods/discs, and or a plane to allow for analytical solutions, the “disc-like” like structure of CuPc and the “sphere-like” structure of C60 make them ideal materials for fundamental OPV research. Investigation of pure and bilayer films rather than a mixed or BHJ film morphology, allows for the isolation of the individual steps in the photo conversion process, such as having a well-defined morphology at the D / A interface. Although OMBD does not provide the ease of scalability provided by solution processing techniques, the sub-monolayer thickness accuracy of OMBD provides for very precise control of film growth, making it ideal for fundamental OPV research.

1.9.2 Chapter 3: Thermally induced dewetting in ultrathin C60 films on Copper Phthalocyanine

By investigation of the evolution of thermally annealed ultrathin fullerene-C60 layers on copper phthalocyanine, evidence for the incompatibility of C60 for long-term device stability is demonstrated as well as providing a practical method to achieve a morphology resembling the “ideal” OPV shown in figure 1. Thermal annealing of the bilayer film at a relatively low temperature of 105° C induced spherical island ripening of the top C60 layer from ~5-10 nm as-grown into ~20-40 nm radius domains over a 48 hour period. Although the operation temperature for OPVs in practical situations would not likely reach 105° C,

operation at 50° - 75° C is likely to occur. Thus, over 10 – 20 years of operation, the film morphology of a C60 containing OPVs may exhibit detrimental morphology changes.

1.9.3 Chapter 4: Toward Single-Crystal Hybrid-Carbon Electronics: Impact of Graphene Substrate Defect Density on Copper Phthalocyanine Film Growth

By investigation of CuPc films grown on Graphene and Graphite, we demonstrate how the presence of defects impacts CuPc film growth and the suitability of Graphene as an electrode for OPVs. Low defect density graphite substrates allow CuPc crystals larger than a micrometer to be formed. Additionally, the CuPc molecules adopt a flat-lying morphology, which enhances light absorption. The morphology of CuPc in defect free regions meets all of the key requirements for a donor layer in an efficient bilayer device. Namely, the substantial reduction in traps, defects, and grain boundaries, and preferred molecular orientation. These properties improve each of the steps necessary for photo conversion, with no conceivable detrimental effects.

1.9.4 Chapter 5: Layer-by-Layer Growth of Crystalline C60 Films on Flat-lying Copper Phthalocyanine

By investigation of C60 film growth morphology on CuPc / Graphite, the validity of a bilayer device being ideal for efficient photo conversion, as suggested by my findings in the

previous chapter, is further investigated. Remarkably, the co-facial D / A interface induces a C60 film morphology that is not only composed of large, highly ordered crystals, but is also stable under thermal annealing up to 150° C. In addition to the reduced traps, defects, and grain boundaries provided by having large, ordered C60 crystals, the co-facial interface enhances Pi orbital overlap between the CuPc and C60 molecules which should facilitate more efficient exciton dissociation.

These findings give merit to an alternative method of achieving High PCE OPV devices using tandem bilayer devices. Tandem cells stack two or more OPVs on top of one another. This means each cell is only responsible for absorbing a portion of the incident photons, allowing for a thinner active layer, which reduces recombination due to improved charge extraction. Since however many cells are needed can be added to absorb all of the incident photons, the thickness and morphology of each cell can be optimized for efficient exciton dissociation and charge transport.

1.9.5 Chapter 6: Morphological, optical, and electronic properties of three distinct crystal orientations present in a Beta CuPc thin film

In this chapter the morphological, optical, and electronic properties of a beta CuPc film is examined. In addition to the alpha herringbone and brickstone crystal structures adopted in CuPc thin films, as described/characterized in previous chapters, the beta herringbone crystal structure is of particular interest due to not only being the most stable CuPc crystal structure known, but also exhibits the highest charge carrier mobility.

GIWAXS on beta CuPc reveals three orientations of beta herringbone crystals coexist in the film. Micro Uv-Vis, AFM, and KPFM on individuals crystal domains is employed to further characterize the properties of each of the three observed crystal orientations.

CHAPTER 2

Experimental Methods

2.1 Sample Fabrication Techniques

The first step in performing an experiment on an organic semiconducting material is sample fabrication. The method used to create a sample may have a significant impact on its optoelectronic properties due to differences in the morphology. The three primary routes for fabricating a sample from an organic semiconducting material are using a tube furnace, solution processing, and thermal evaporation in high vacuum.

Tube furnaces provide purification of the material as well as being useful for creating 3-D crystals of controllable sizes, which is particularly beneficial for creating device from a single crystal. Solution processing includes a variety of techniques including drop casting, spin coating, blade-coating, and slot-dye printing. The scalability of solution processing makes it highly suitable for mass production of organic electronics, but the complexities of the BHJ can make it challenging to manipulate the film morphology as desired, making it less suitable for experimental studies of fundamental optoelectronic properties. Thermal evaporation/sublimation in high vacuum or ultra-high vacuum of materials onto a substrate is commonly used to deposit metals, such as electrodes, as well as being compatible with some organic materials. The sample creation technique chosen by the researcher is largely dependent on what properties of the material they wish to investigate.

In the literature, thermal evaporation/sublimation of materials in vacuum has several names, but is commonly referred to in general as Physical Vapor Deposition (PVD), or OMBD if the material is organic. OMBD is not compatible with all organic materials due to decomposition of the material prior to evaporation. Specifically, high molecular weight materials, such as polymers like P3HT³⁰, suffer from decomposition due to heating prior to thermal evaporation, resulting in a film composed of broken fragments of the original material. Unlike alternative organic sample fabrication techniques, OMBD provides sub-monolayer deposition precision of materials as well as simultaneous deposition from multiple sources.

The precise control offered by OMBD makes it suitable for experimental studies of fundamental optoelectronic properties, but the higher thermal budget and need of loading/unloading samples into vacuum makes it less suitable for mass production of devices. As a physicist interested in investigating the impact of morphology on the fundamental properties of organic semiconducting materials, I choose to use OMBD as my primary method of sample fabrication.

2.2 Organic Molecular Beam Deposition Chamber

For precision film growth with minimal impurities, OMBD is most likely the best choice. By monitoring the deposition rate with sub-nanometer accuracy, pure or blended films of a desired composition can be grown with sub-monolayer thickness precision. Since no solvents are used, arbitrarily high film purity can be achieved by growth in higher vacuum

and by further purification of the starting materials prior to deposition. The expressed advantages of OMBD are not intrinsic, and are achieved by careful design of the deposition system.

After using the Dougherty group's existing OMBD "box chamber" for sample growth for a few months, it became apparent that it was not suitable for achieving the film precision/accuracy necessary for my experiments. Using spare high vacuum equipment in Dougherty Lab, along with ~ \$2500 in additional equipment purchased using my GAANN NEEM grant, I constructed a new OMBD chamber, shown in figure 2.1, with the precision/accuracy I needed. The OMBD chamber I constructed features: two deposition sources, with optional third source, co-deposition capable; sub-monolayer thickness precision, with less than 5% thickness variation over the ~ 2 in by 2 in sample plate; and by minimizing the chamber volume, a fast pump down time of only ~ 45 minutes is needed to reach an acceptable deposition pressure of 2×10^{-6} torr. These features of the OMBD chamber I constructed were achieved primarily by careful design of the chamber.

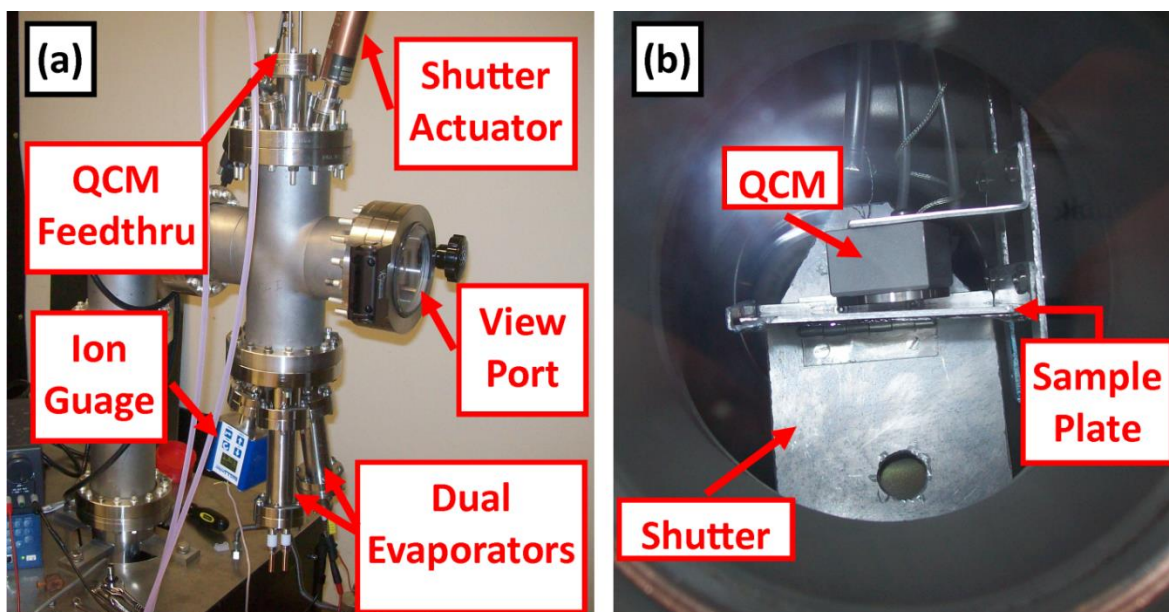


Figure 2.1 External view of chamber shown in (a). Internal view of chamber is shown in (b), as seen through the View Port labeled in (a). The hot-filament ionization gauge (Ion Gauge) measure the pressure in the OMBD chamber in the range of $\sim 10^{-4} - 10^{-10}$ torr range. Quartz Crystal Microbalance (QCM) monitors the deposition rate by measuring the mass adsorbed. A shutter is essential for OMBD because it allows experimenter to stabilize the deposition rate prior to film growth.

The first thing to determine when designing an OMBD chamber is the maximum number of source materials one needs to use for a film growth. When making devices, in addition to your donor and acceptor materials, a hole blocking material such as BCP, and a metal for the anode, such as aluminum, may be needed. The next decision is what film thickness accuracy/precision/variation is acceptable, and over what area. Once the answers to these questions, you can design the OMBD chamber using basic geometry. The film thickness accuracy/precision/variation is determined by the distance between the substrate and the source, as well as the source type and physical orientation.

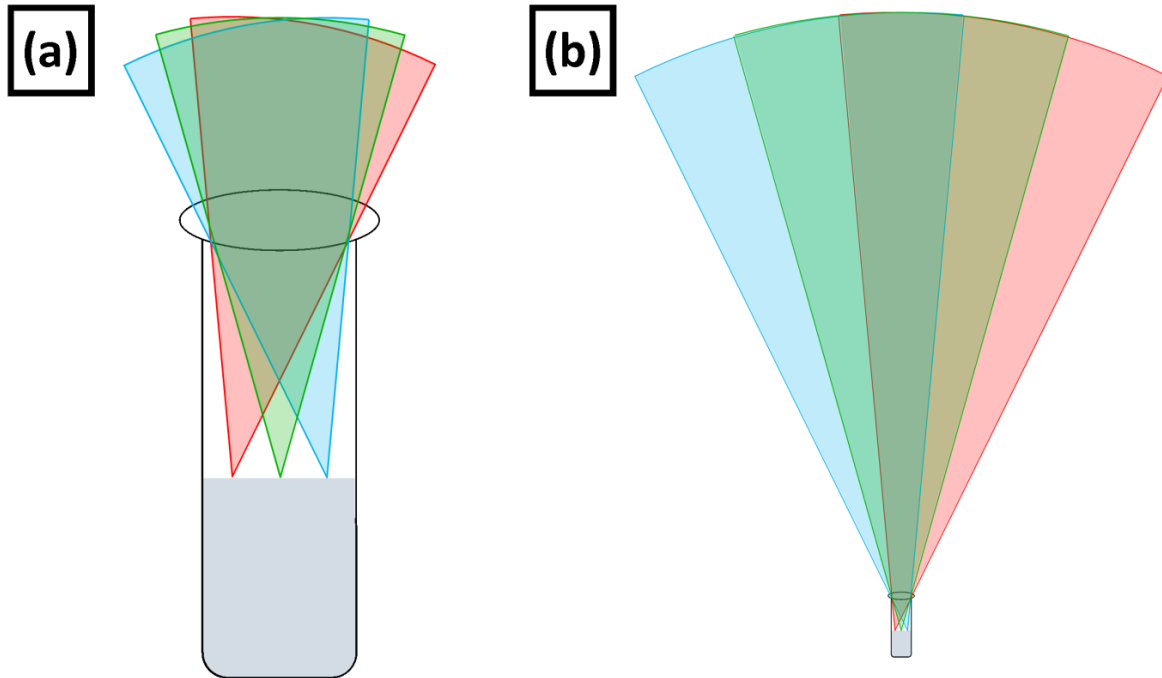


Figure 2.2 Deposition Uniformity. Illustrates of the deposition uniformity of a crucible modeled as three point sources.

A crude method of estimating the deposition profile of a source is to model it as a point source. A much more accurate method would be to model the source as a continuous distribution of point sources. For this example, I have modeled my deposition source as three point sources, as seen in figure 2.2 (a). Looking at figure 2.2 (a), it can be seen that a substrate placed near the crucible would have a narrow area where it would receive flux from all three point sources. It is also clear from the arcs of equal flux that the source- sample distance varies significantly, even in the region directly above the crucible. Figure 2.2 (b) shows two distinct advantages for increasing the source to substrate distance. First off, a much larger area can “see” all three point sources. Secondly, the arcs of equal flux begin to

overlap. Thus, the primary factor that determines the deposition uniformity over a given area is the distance between the source and substrate. Arbitrarily high precision can be achieved by this method. Secondly, the orientation of the crucible is important. For maximum uniformity, the crucible should be oriented such that if one were to draw an imaginary line through the center of the crucible and extend it to the substrate position, it would intersect the center of the sample plate. As seen in figure 2.2, tilting the crucible by only ~10 degrees can drastically change the deposition profile. It is thus imperative that the crucible is not only aligned coaxially with the substrate plate, but that it is physically stable, especially if the flux monitor is outside of the area of uniform deposition..

Considering these factors, the position of the QCM is important for the thickness accuracy. Often, the QCM is positioned off to the side of the sample plate to allow the substrates to be placed within the region of low thickness variation. The reduced flux from the QCM being off axis from the crucible can be easily calibrated to represent the actual deposition rate at the substrate. While a slight change in the crucible orientation angle would not result in a substantial variation in deposition uniformity at the substrate, if the QCM is already outside of the uniform deposition area, it would experience a much more substantial change in flux, making the film thickness calibration inaccurate. Considering this, I chose to sacrifice some of my sample plate area by cutting a hole in the center of the sample plate to allow the QCM to be positioned in the center of the uniform deposition area, as seen in figure 2.1 (b).

2.3 Atomic Force Microscopy

AFM is a powerful tool for surface investigation of a film. In addition of providing a 3-D mapping of the topography of a film, it can also measure electrical and magnetic properties as well. Topography measurements can be performed by two primary methods. The first, and original technique, often referred to as “contact mode”, is where the tip is kept in contact with the film by a constant force, and dragged across the sample while measuring the height of the tip as it rasters across the sample. Contact mode works well with hard materials, such as silicon, but can lead to substantial damage to the surface of soft materials, such as organic materials used for organic electronics. The alternative method to contact mode AFM is “tapping mode”, which can substantially reduce the tip-film interaction, making it more suitable for studying the topography of soft materials.

In tapping mode, the cantilever is oscillated near its resonant frequency above the film surface. As the tip approaches the film, van der Waals forces create a potential well that dampens the oscillations of the cantilever. Thus, the cantilever can be modeled as a damped driven simple harmonic oscillator. The surface topography is measure by lowering the cantilever until either the amplitude changes by a specified amount for amplitude modulated AFM, or the frequency changes by a specified amount for frequency modulated AFM. The cantilever is then moved to the next location, and its height is adjusted to maintain the same dampening, or “set point”. I used amplitude modulated, tapping mode, AFM to measure the topography of my films. The amount of dampening specified by the experimenter determines how strongly the tip interacts with the film. In some cases, the tip can be

prevented from making contact with the film by specifying a set point high enough to be sensitive to the attractive, long range, van der Waals forces.

There are two primary considerations when choosing how strongly to dampen the tips oscillations in tapping mode. The longer range, attractive component of the van der Waals force exhibits a slow change in the applied force with decreasing tip-substrate distance, which the shorter range, repulsive component exhibits a rapid change in the applied force with decreasing tip-substrate distance. Choosing a low tip dampening, such as in the attractive regime of the van der Waals potential, necessitates a slower scan rate to allow the tip to equilibrate at each location. Choosing a high tip dampening allows for faster scanning, but may introduce sample and/or tip deformations.

Organic small molecules, especially C_{60} , can be particularly susceptible to deformations in the sample and tip morphology. Choosing a high tip dampening in this case causes molecules to detach from the sample and attach to the tip, leading to not only a morphology change in the sample, but the deformed tip also induces tip imaging.

In addition to the topography, AFM can also be used to measure the electrical and magnetic properties of a film. While van der Waals forces have a distance dependence of $\sim 1/r^6$ for the attractive component and $1/r^{12}$ for the repulsive component³¹, electric and magnetic forces have a distance dependence of $1/r$, $1/r^2$, or $1/r^3$. Thus electric and magnetic forces are much longer range than van der Waals forces. By taking advantage of the distance dependence of the forces, once the topography is known, the AFM cantilever can be

withdrawn from the surface enough to make the van der Waals forces negligible, allowing the electrical and/or magnetic properties to be measured.

Kelvin Probe Force Microscopy (KPFM), is once such measurement which allows the electric surface potential of the film to be measure. After each topography line scanned, the same line is scanned again but at a specified distance above the now known topography. By varying an applied voltage between the sample and the AFM cantilever, the electric force on the cantilever can be made zero. If there is no electric force between two materials, there is also no net electric field, necessitating they are at the same potential, thus the surface potential for that location is determined. I used KPFM for my work in chapter 6 to compare the variation in surface potential of Beta CuPc crystals of different orientation.

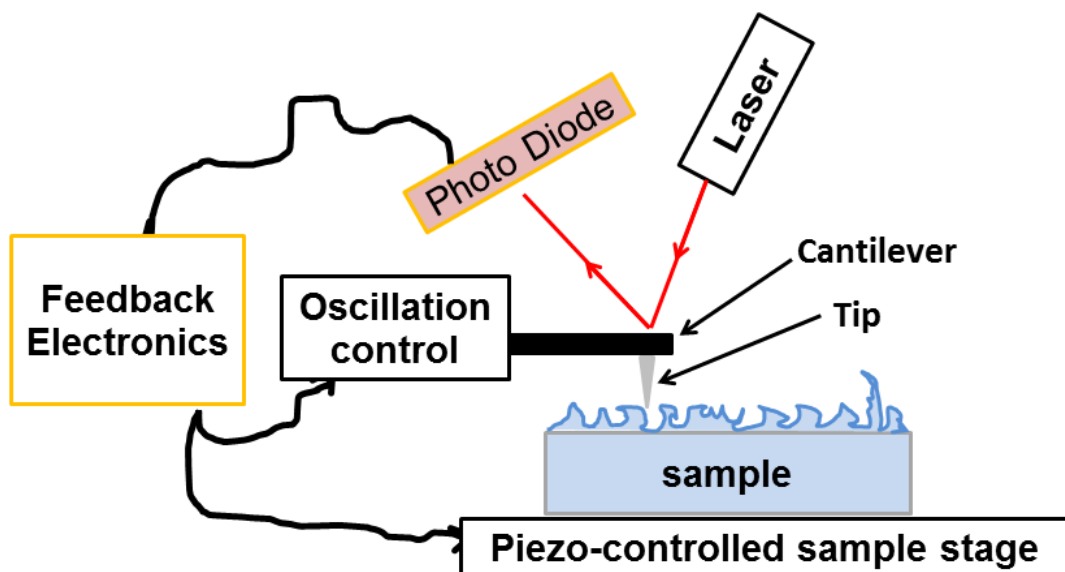


Figure 2.3 Schematic of Atomic Force Microscopy primary components. Motion in the plane of the sample is controlled by X and Y piezo motors on the sample stage. Motion perpendicular to the plane of the sample is achieved by the Z piezo motor attached to the cantilever. The cantilever height and oscillations are measure by reflecting a laser off the cantilever. Using the z-height and cantilever oscillation dampening as inputs, a feedback loop is used measure the height of the film as the cantilever raster across the sample.

2.4 Grazing Incidence Wide-Angle X-ray Scattering

Grazing Incidence Wide-Angle X-ray Scattering (GIWAXS), also commonly referred to as Grazing Incidence X-ray Diffraction (GIXD), measures the in-plane and out-of-plane crystal structure of a film. GIWAXS is an elastic hard X-ray scattering technique similar to X-ray Diffraction (XRD), but with a fixed incidence angle for the X-ray beam and utilizing a 2-D detector. Using a 2-D detector allows GIWAXS to probe the crystal structure perpendicular to the sample plane, which may also be measured by XRD, as well as the crystal structure in the plane of the sample, which is not measureable by XRD. The drawback of GIWAXS is the need to be a fixed incidence angle, which limits probe-able q -

space in the out of plane direction to a single point. GIWAXS is quite useful for identifying the crystal structure and orientation of organic thin films.

GIWAXS measurements were performed at beam line 7.3.3³² of the Advanced Light Source using 10 keV photons and Pilatus 2M and 2M detectors. Hard x-rays scatter primarily from electrons. To reduce scattering from molecules in the air such as N₂, which has 14 electrons per molecule, samples are loaded into an enclosure filled with Helium, which has only 2 electrons per atom. This reduces the air scattering by a factor of seven.

There are three primary paths the photon can take. First, the photon may be reflected off of the surface of the film. If the photon is reflected off of the surface of the film, there is an evanescent wave localized at the surface, allowing scattering from only the very top of the film. The second path the photon can take is through the film as well as the substrate. Scattering from this process is referred to as direct beam scattering since the x-ray beam maintains the same momentum vector while in the film. The third path the photon can take is through the film, but reflected from the film/substrate interface. Once reflected, the x-rays have a different momentum vector than the incident beam as they travel back through the film, allowing scattering during this process to be referred to as scattering from the reflected beam. The difference in momentum between the direct and reflected beams depends on the incidence angle. As the incidence angle approaches zero, there is no momentum difference between the direct and reflected beams. Inelastic scattering, multiple scattering events, as well as multiple reflections from interfaces may also occur, but is generally considered negligible.

Often with GIWAXS, the incidence angle is chosen by the experimenter to maximize scattering from the film. To do this, an incidence angle higher than the critical angle of the film, but lower than the critical angle of the substrate. This allows for the longest path length of the x-rays in the film, and thus the most scattering. The downside to this approach is that the scattering signal is coming from both the direct and reflected beam. If an accurate and precise \mathbf{q} value of the scattering peak is desired, an incidence angle higher than the critical angle of both the film and the substrate is preferred. By using an incidence angle higher than the critical angle of the substrate, the reflected beam is minimized.

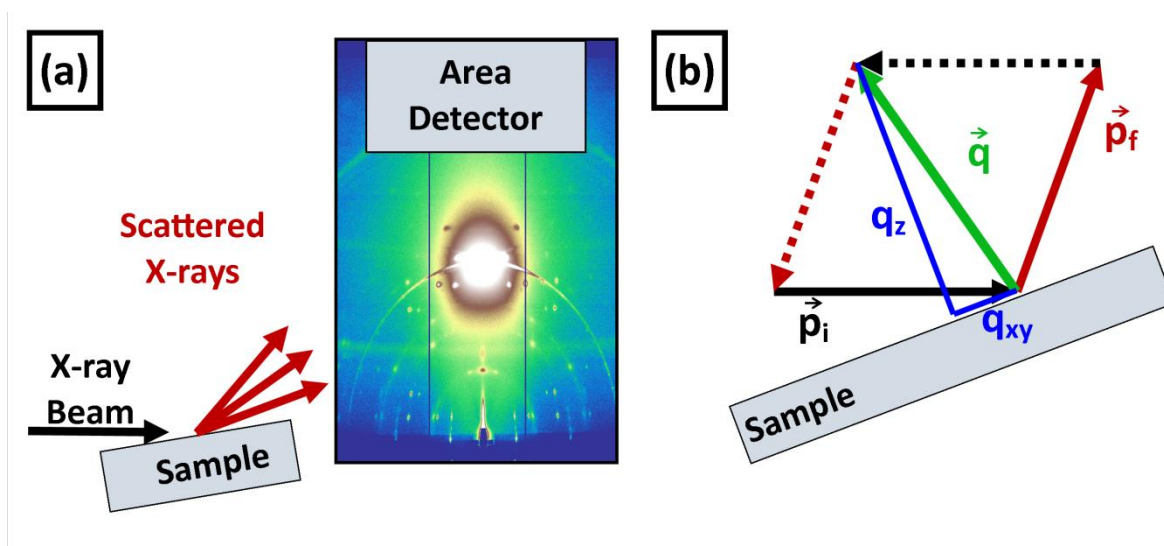


Figure 2.4 Grazing Incidence Wide-Angle X-ray Scattering. Schematic of GIWAXS setup shown in (a). Figure (b) is an illustration of momentum transfer vector, \mathbf{q} , and separated in its in-plane component, q_{xy} , and out-of-plane component, q_z .

Figure 2.3 b illustrates the momentum transfer during the scattering process. The black arrow, \mathbf{p}_i , represents the incident photon. The red arrow, \mathbf{p}_f , represents the scattered

photon. The green arrow, \mathbf{q} , is the difference between \mathbf{p}_i and \mathbf{p}_f , known as the momentum transfer vector. The momentum transfer vector can be decomposed into components either parallel to the substrate, q_{xy} , or perpendicular to the substrate, q_z . As mentioned above, one drawback of GIWAXS is that the q_{xy} component is zero only when \mathbf{p}_i and \mathbf{p}_f are in the same plane and have the same incidence angle. For scattering at higher q values, the momentum transfer vector has more and more of a q_{xy} component, resulting in a “forbidden wedge” of data missing along the q_z axis.

2.5 Total Electron Yield Near-Edge X-ray Absorption Fine Structure

NEXAFS, also referred to as X-ray Absorption near edge structure (XANES), measures the absorption spectra of a material due to the excitation of a core electron into an unoccupied molecular orbital. NEXAFS is particularly sensitive to the types of bonds within the molecule since each bond contributes to the molecular orbitals. Since changing a bond within a molecule alters the molecular orbitals, it also alters the energy difference needed to excite a core electron into an unoccupied state. This allows each molecule to have a unique “fingerprint”. Unlike hard x-ray and neutron techniques which “see” contrast based on density variations, the bond specific contrast of NEXAFS is highly suitable for distinguishing differences in organic materials, which generally have very similar densities.

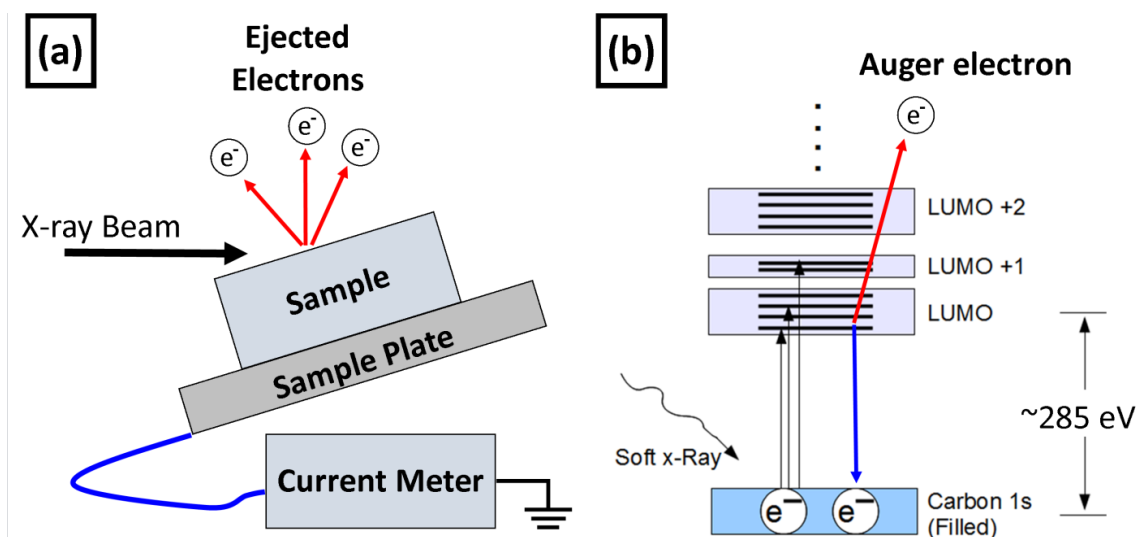


Figure 2.5 Total Electron Yield Near Edge X-ray Absorption Fine Structure. Schematic of TEY NEXAFS experimental setup is shown in figure (a), where the x-ray beam, sample, and sample plate are in a high vacuum enclosure. Figure (b) illustrates the energy band diagram for x-ray absorption and Auger decay processes occurring during TEY NEXAFS measurements.

NEXAFS can be performed by transmission, x-ray fluorescence, or electron yield. Transmission NEXAFS is experimentally analogous to Uv-Vis absorption spectroscopy, and provides accurate absorption spectra as long as the film thickness is in a range to absorb enough photons, but not all. X-ray fluorescence and electron yield methods measure the absorption spectra indirectly by observing either photons or electrons ejected from the sample when an electron transitions from a valence band back to a core hole created when an x-ray is absorbed.

The absorption cross section for electrons is much higher than that of x-rays in organic materials, making electron yield methods surface sensitive, where transmission and x-ray fluorescence methods sensitive to the bulk of the film. Electron yield methods can be

less accurate for measuring the absorption spectra of a material due to the non-linearity of electrons ejected from the sample per photon as a function of energy. Total electron yield measurements are easy to obtain by simply measuring the drain current from the sample plate. If a more accurate absorption profile is needed, partial electron yield measurements can be implemented, where a detector with energy filtering can be used to detect electrons in a specific energy range. For my experiments in chapter 3, I needed to measure the surface composition, making TEY NEXAFS the best choice. A schematic of a TEY NEXAFS experimental setup is shown in figure 2.5.

CHAPTER 3

Thermally-Induced Dewetting in Ultra-Thin C₆₀ films on Copper Phthalocyanine

3.1 Preface

This chapter will be comprised of a reproduction of work that was previously published in 2013 in The Journal of Physical Chemistry C, Vol 117, pages 26007-26012

Coauthors: T. McAfee, E.H. Gann, H. Ade, and D.B. Dougherty*

Department of Physics, North Carolina State University, Raleigh, NC 27695

*Corresponding Author: dbdoughe@ncsu.edu

3.2 Abstract

The evolution of thermally-annealed ultra-thin fullerene-C₆₀ layers on copper phthalocyanine is examined by Atomic Force Microscopy and Near Edge X-Ray Absorption Fine Structure spectroscopy. Annealing causes C₆₀ films to dewet the copper phthalocyanine substrate surface via lateral surface mass transport. Coarsening of C₆₀ clusters is observed that creates mounds that exceed the nominal C₆₀ thickness by more than an order of magnitude and is consistent with surface diffusion-mediated mass transport. Implications for thermal morphology control in organic solar cells, such as the destabilization of multilayered C₆₀:CuPc with individual layers only ~5-10 nm thick, are discussed.

3.3 Introduction

Bilayer photovoltaic cells employing interfaces between Copper Phthalocyanine (CuPc) and fullerene-C₆₀ were among the first to demonstrate that organic materials can provide a cost effective alternative to the traditional inorganic solar cells.^{14, 33} These materials are of interest due to their synthetic reproducibility in structure and the precise film thickness control offered by organic molecular beam epitaxy (OMBE) compared to solution-processed devices. While solution-processed polymer devices have recently defined the state-of-the-art in organic photovoltaic device performance with power conversion efficiencies reaching >8%,³⁴ small-molecule devices, such as the CuPc:C₆₀ bilayer, offer advantages in terms of precise composition control during vacuum evaporation and relative ease of integration into tandem architectures.³⁵ CuPc:C₆₀ bilayer films have also become important experimental and theoretical model systems in order to investigate the impact of molecular orientation at the heterojunction interface.³⁶

Recently, evaporated small -molecule organic photovoltaic (OPV) devices achieved a power conversion efficiency (PCE) of 6.6 ± 0.2 % using a novel “donor-acceptor-acceptor” molecular architecture which increases both the short-circuit current (J_{sc}) and open-circuit voltage (V_{oc}) by manipulating the optical bandgap of the active material.¹⁹ However, such advances in control over the bandgaps of OPV materials may not be sufficient to reach the PCE needed to be cost effective. A deeper understanding and control of the domain size, domain purity, and molecular orientation are crucial for achieving efficient exciton dissociation, charge transport, long-term device stability, and ultimately the PCE. Control of

the film morphology in these devices is thus vital and methodologies such as post deposition thermal annealing need to be assessed for their efficacy as a control parameter.

The need for morphology control and manipulation has been recognized in efforts to grow mixed films of small-molecules by vacuum co-deposition in order to create intermixed morphologies analogous to those achieved in solution-processed bulk heterojunction (BHJ) solar cells.^{11a,37} The BHJ morphology comprises a bicontinuous network of nanoscale donor and acceptor domains that is thought to be ideal for simultaneous optimization of exciton dissociation and free-carrier transport. Unfortunately, it is not always straightforward to achieve BHJ-like device performance using small-molecule co-deposition. Morphologies and donor-acceptor connectivity can be degraded^{11a} and exciton dissociation efficiencies can be reduced.³⁸ However, there have been notable successes³⁹ including a tandem cell with a high PCE of more than 6 %.

Small-molecule intermixing strategies have been elaborated using the uniquely-precise capabilities of OMBE growth to create compositionally-graded solar cells by co-deposition of C₆₀ with CuPc and with boron sub-phthalocyanine.³⁷ Holmes and co-workers showed that by creating films with controlled gradients in donor-acceptor composition, they could achieve improvements in PCE compared to simply co-depositing the two materials to create a film with fixed composition. This clearly shows that it is possible to adjust OMBE growth conditions to improve the donor-acceptor networks in the OPV. More generally, controllable nanostructuring of donor-acceptor mixtures shows promise for solving the morphology problem for many donor-acceptor OPV's.⁴⁰

In this work, we investigate the morphological stability of the C₆₀:CuPc interface. We find that ultra-thin C₆₀ films on top of CuPc are unstable under even relatively low temperature annealing conditions resulting in large-scale lateral dewetting. This interpretation is unambiguously revealed by a combination of AFM imaging and NEXAFS spectroscopy on the same samples, which distinguishes lateral dewetting from previously-asserted vertical phase segregation of CuPc.⁴¹ Direct AFM observation of the dewetting process suggests a surface diffusion-mediated ripening of C₆₀ clusters at the interface that implies significant surface diffusivity and a strong tendency for phase segregation that needs to be considered as part of small-molecule OPV processing strategies. Moreover, the dewetting process could be implemented as a means to controllably nanostructure donor-acceptor interfaces in order to achieve a comb-like morphology that would simultaneously optimize carrier transport and exciton dissociation allowing for thicker OPV devices with increased light absorption and J_{sc}.

3.4 Experimental Methods

Four bilayer samples of 1.9 ± 0.3 nm C₆₀ / 10 ± 1 nm CuPc / Silicon(100) were prepared in parallel by sequential deposition in a UHV chamber with a base pressure of $<1 \times 10^{-8}$ Torr. The C₆₀ (98%) and CuPc (95%) were obtained from Sigma-Aldrich and loaded, as received, into quartz and boron nitride crucibles, respectively, followed by several hours of outgassing in high vacuum prior to film growth. A Silicon(100) wafer with native oxide was cleaved, then sonicated in Acetone followed by Isopropyl Alcohol for 15 minutes each then

immediately loaded into the UHV chamber for deposition. The CuPc and C₆₀ thin film layers were then grown at $< 6 \times 10^{-7}$ torr by thermal evaporation from the heated crucibles. A quartz crystal monitor (QCM) was used to monitor the growth rate and thickness of each layer. Samples were thermally annealed at 105 °C for 30 minutes, five hours, and 48 hours in a dry nitrogen glove box with ~2 ppm of Oxygen and 1-5 ppm H₂O. This annealing temperature was chosen for direct comparison with a recent study reporting vertical phase separation in the same system.⁴¹ Moreover, it is within the range of temperatures relevant to small-molecule OPV processing for enhancing charge transport.^{33, 42} A separate sample prepared in the same way was annealed at a higher temperature of 150 °C for comparison. Films of pure C₆₀ and CuPc were prepared using identical procedures and it was confirmed that no changes in these films were observable after annealing. As-Grown and 30 minute annealed at 200 °C samples of thicker bilayers films of 60±6 nm C₆₀ / 80±8 nm CuPc / Silicon(100) were grown at pressures $< 2 \times 10^{-6}$ torr by the same experimental methods described above. Total Electron Yield Near Edge X-ray Absorption Fine Structure (TEY NEXAFS) and Atomic Force Microscopy (AFM) were performed on the 1.9±0.3 nm C₆₀ / 10 ±1 nm CuPc / Silicon(100) samples. Resonant Soft X-ray Reflectivity (RSoXR) data was taken on the 60 nm C₆₀ / 80 nm CuPc / Silicon(100) samples.

Total Electron Yield Near Edge X-ray Absorption Fine Structure (TEY NEXAFS) spectra and RSoXR data were collected at Beamline 6.3.2 at the Advanced Light Source. TEY NEXAFS carbon K-edge spectra were obtained for the photon energy range from 270 – 400 eV. The data was normalized to the incident photon beam intensity measured by a

photodiode. Atomic Force Microscopy was carried out in non-contact mode under ambient conditions using a commercial instrument (Asylum Research MFP-3D). AFM tips (Budget Sensors, Tap300AL-G) had a nominal radius of ~ 10 nm and a nominal resonant frequency of ~ 300 kHz. The TEY NEXAFS technique is surface sensitive and so our use of very thin films of C_{60} allows direct access to interfacial composition changes that would not be possible for thicker films typically used in bilayer OPV's.

3.5 Results and Discussion

3.5A AFM Measurements of Film Morphology

The AFM measurements shown in Figure 3.1 illustrate significant changes in morphology near the bilayer surface due to annealing. Films of C_{60} grown on top of CuPc exhibit a granular morphology as shown in Figure 3.1a suggestive of small C_{60} aggregates decorating the somewhat larger grains of the CuPc film. This is very similar to the granular growth of C_{60} on top of pentacene films.⁴³ While no change in film morphology is obvious after 30 minutes of annealing, after 5 hours it is clear that average cluster size has increased in both height and width on the surface (see quantification in Sec III.C). This growth in cluster size persists for further annealing up to 48 hours. In between the large clusters, film morphology is consistent with that of a *pure* CuPc film grown on SiO_2 annealed at low temperature (less than 150 C), well-known from our own work and several other studies.⁴⁴

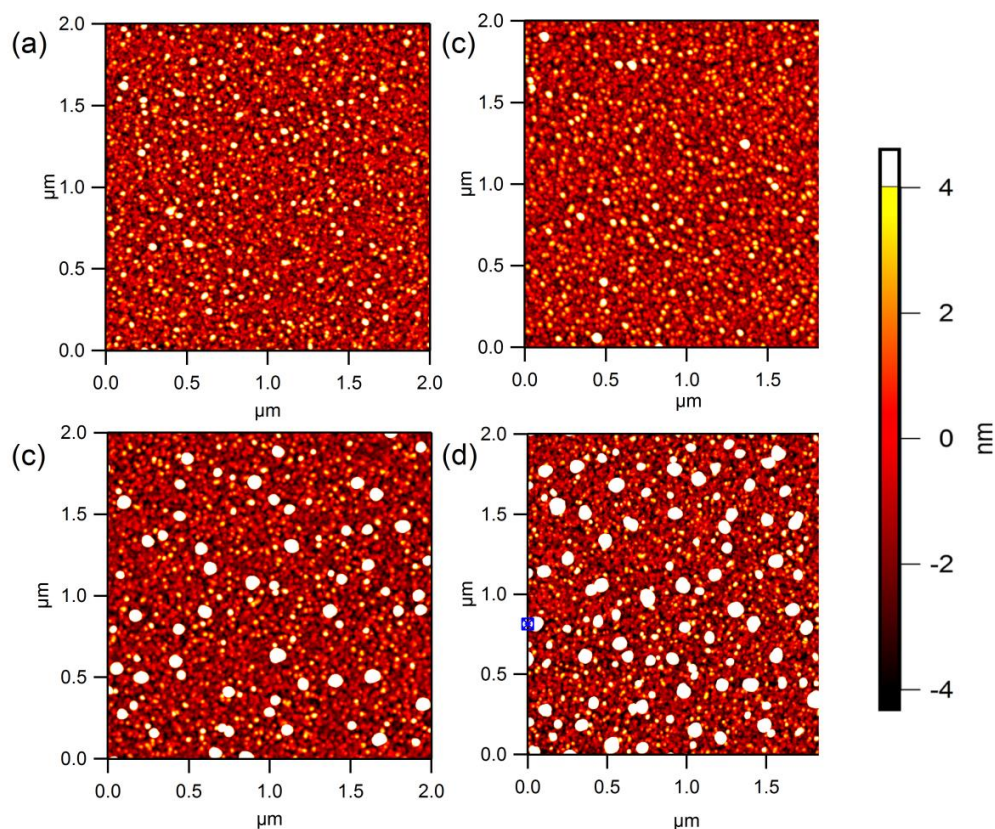


Figure 3.1 AFM Time Series of C_{60} Dewetting. $2 \mu\text{m} \times 2 \mu\text{m}$ AFM images collected in non-contact mode of nominal 2 nm C_{60} / 10 nm CuPc / Si(100), a) As-Grown and annealed at 105 °C for times of: b) 30 minutes, c) 5 hours, and d) 48 hours

The morphological changes increase in rate when annealing at higher temperatures as shown in the sequence in Figure 3.2. Here, a somewhat thicker film is imaged so that an increase in surface mound size is more apparent than in Figure 1 after only 30 minutes of annealing at 100 °C as shown in Figure 3.2b. Significant mound coarsening is observed after 30 minutes of annealing a separate film of the same thickness at a higher temperature of 150 °C as shown in Figure 3.2c. This indicates the expected acceleration of activated surface mass transport as temperature increases.

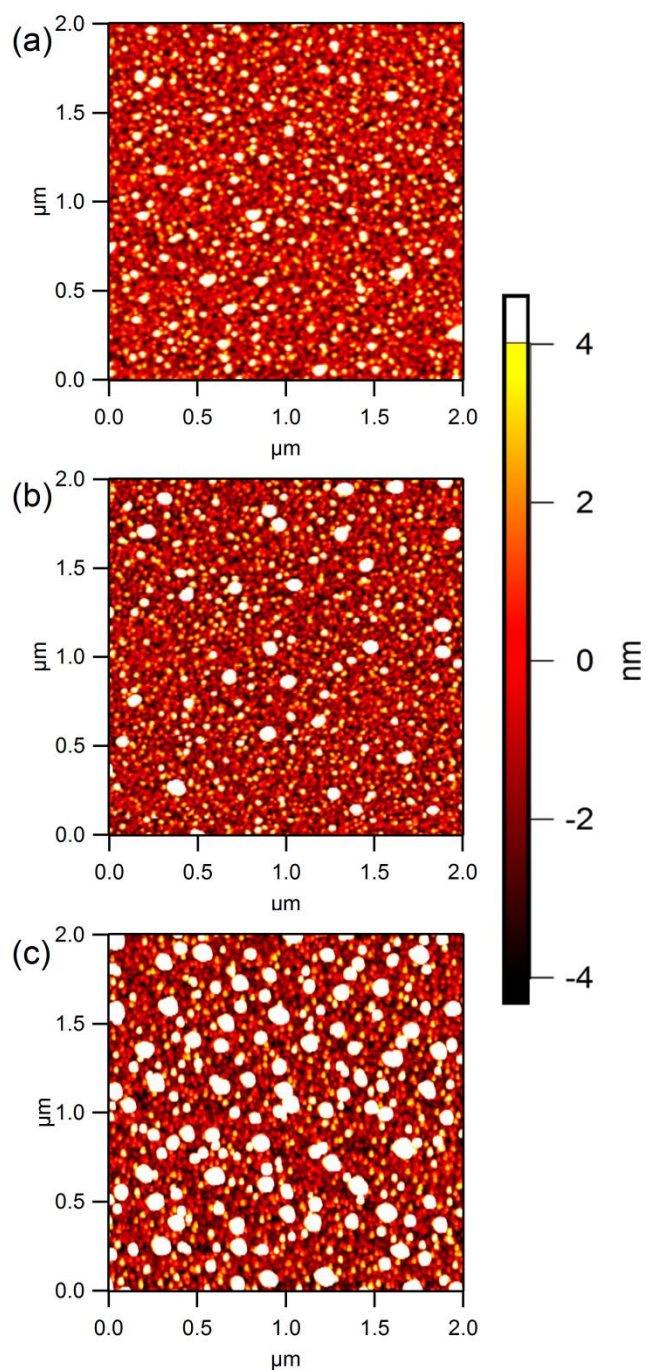


Figure 3.2 AFM Temperature Series of C_{60} Dewetting. $2 \mu\text{m} \times 2 \mu\text{m}$ AFM images of a 2.2 nm C_{60} film on CuPc a) As-grown; b) annealed at 100 C for 30 minutes; and c) annealed at 150 C for 30 minutes.

3.5B NEXAFS Measurements of Film Surface Composition

In order to clarify the composition of the observed 3D mounds on this surface, we carried out TEY NEXAFS on the same films shown in Figure 3.1. Figure 3.3 shows the NEXAFS spectra for the four bilayer films after different annealing protocols along with reference spectra for the pure C₆₀ and CuPc. The NEXAFS spectra for the pure materials show a very convenient anti-correlation just above 285 eV where C₆₀ has a local minimum and CuPc has a strong peak due to multiple transitions into its lowest unoccupied molecular orbital.⁴⁵ As a function of annealing time, an enhancement of the CuPc peak is seen in this local region starting with the 5 hour annealing time. The relative changes in these spectra can be quantified by fitting the bilayer spectra to linear combinations of the pure material spectra (including also linear and constant background terms). The results of this fitting show that the relative contribution of the pure CuPc to the spectra increase from 34% for the as-grown and 30 minute annealed bilayers, to 38% after 5 hours annealing and 52% after 48 hours annealing.

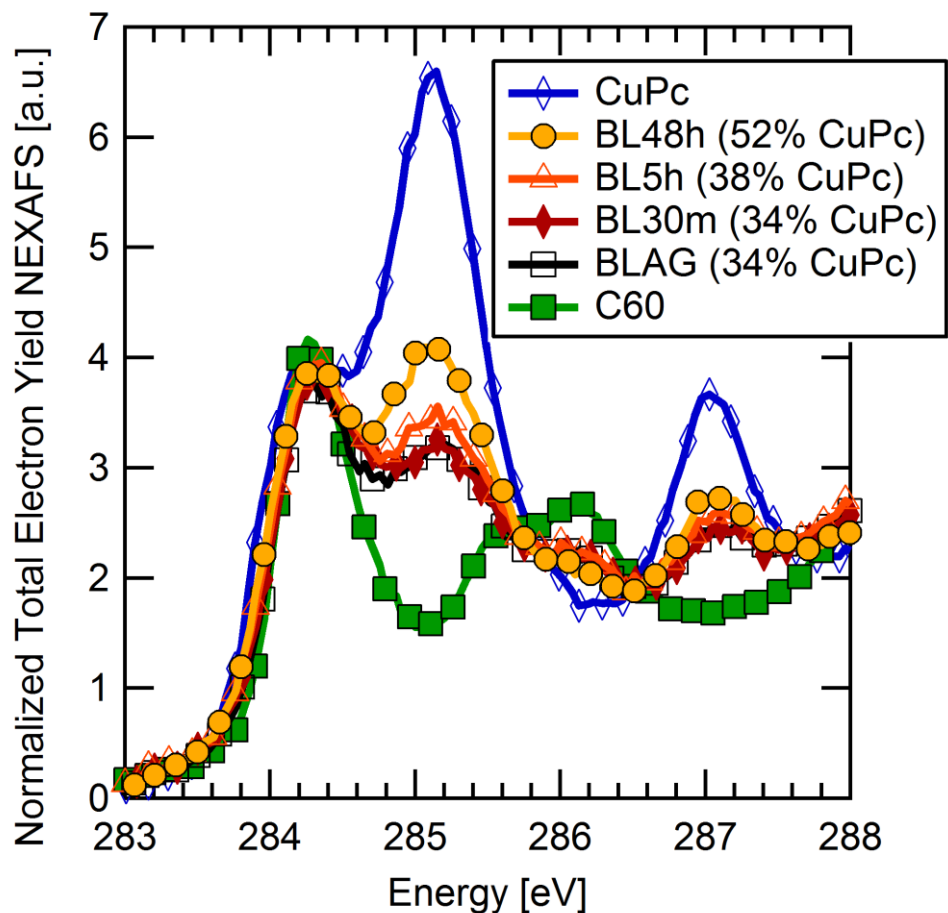


Figure 3.3 Surface Composition. TEY NEXAFS spectra of the Carbon K-edge in the region of highest absorption contrast between CuPc and C₆₀. The results of component fitting are shown in the legend in percentage of CuPc.

The combination of AFM and NEXAFS leads to the clear conclusion that C₆₀ laterally dewets CuPc with annealing. The increase in the exposed surface area of CuPc explains the increase in its relative contribution to the surface-sensitive NEXAFS spectra. The AFM results provide direct morphological evidence that this interpretation is correct via the appearance and thermal coarsening of large C₆₀ mounds. This conclusion favors an

alternate interpretation of recent photoemission studies of similar bilayers of 2 nm C_{60} on CuPc that was interpreted in terms of vertical phase segregation of CuPc toward the surface.⁴¹ Instead of vertical surface segregation, the same results (see Fig. 3 of Ref. 14) could be interpreted as the result of the purely lateral dewetting process visualized in Figure 3.1 and Figure 3.2.

3.5C Discussion of C_{60} Dewetting

In order to quantify the dewetting process, we measured the full-width-at-half-maximum and height of a large population of C_{60} mounds observed by AFM under each annealing condition. The results are shown as a plot of mound height as function of mound width in Figure 3.4a. The strong correlation between the two shows that the mounds grow in three dimensions (as opposed to only laterally). Most importantly, the approximate slope of the linear trend for the 5 hour and 48 hour annealing times is nearly identical. This leads to the conclusion that the shape of the mounds is largely determined by near-equilibrium interfacial energetics. The size of the mounds may then be inferred to grow primarily as a result of kinetic processes as opposed to a thermally-induced mound re-shaping.

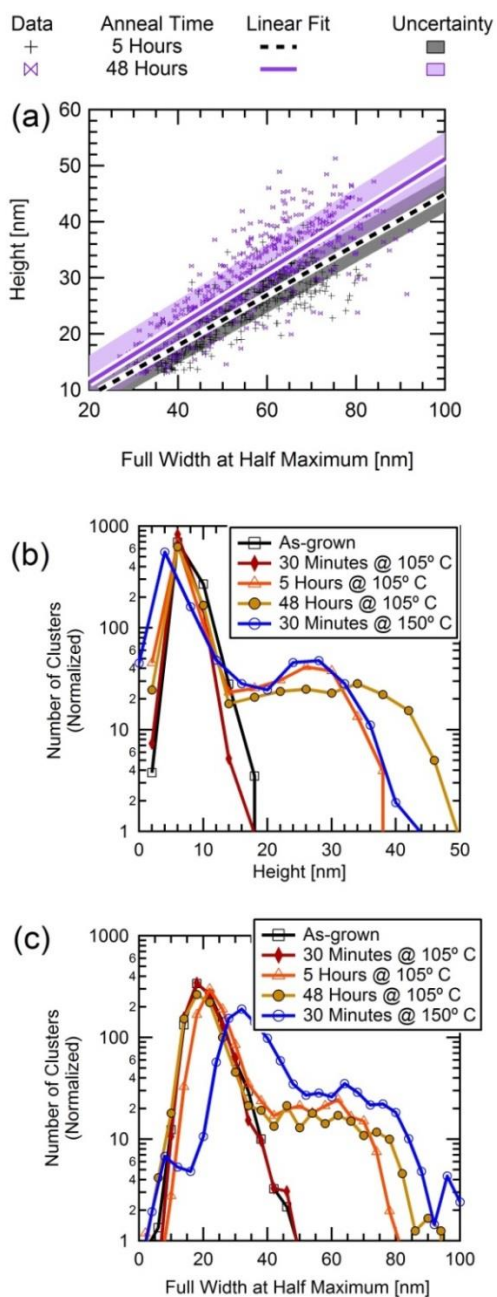


Figure 3.4 C_{60} Cluster Statistics. (a) C_{60} cluster Height vs FWHM for 5 Hour and 48 Hour annealing with least squares linear fit (b) Normalized histogram of cluster heights for time dependent annealing at 105 °C and 30 min annealing at 150 °C (c) Normalized histogram of cluster FWHM for same conditions as in part b).

To clarify the nature of the kinetic processes that give rise to the observed mound ripening, we plot a normalized histogram of mound heights and widths in Figure 3.4b and 3.4c respectively. The as-grown and thirty minute annealed samples are once again almost identical, and have a roughly Gaussian distribution of heights just below 10 nm. Further annealing results in the emergence of a second broad distribution of mound heights that is much taller than the initial species. The total number of smaller mounds and the average height of these mounds both decrease with annealing time, while the larger mounds continue to grow. This is consistent with surface diffusion-limited mound ripening as described for alloys and thin films.⁴⁶ We also note that the C_{60} surface diffusion implied by the dewetting rate is comparable to the reported dewetting of a planar organic on SiO_2 .⁴⁷ In general, the surface diffusion coefficients at organic-organic interfaces have been predicted⁴⁸ to be sizeable, allowing large-scale surface rearrangements with only modest annealing. Finally, at 150° C after only about 30 minutes, the degree of C_{60} island coarsening is intermediate between the images shown in Figure 3.1c-d, consistent with a thermally activated surface diffusion process. The mound height and width distributions for this annealing protocol are shown in Figure 3.4b and 3.4c.

The observation of C_{60} dewetting at a CuPc interface illustrates two important facts about the C_{60} :CuPc interface: 1) surface diffusion of C_{60} on CuPc is significant even at mild annealing temperatures; and 2) Interfacial energies between these two materials are generally unfavorable. The later point suggests a strong tendency for phase segregation that is known for polymer-fullerene heterojunctions and has also been indicated by AFM

observations of mixed, co-deposited C_{60} :CuPc films after annealing deposited on a heated substrate.³⁸ Recent work has also shown that solvent-vapor annealing results in a roughening of the fullerene surface in a combined solution-vacuum-deposited solar cell.⁴⁹ This roughening is explained by the annealing induced lateral dewetting process we describe here. While such uncontrolled processes may be a disadvantage to device performance, they could also be exploited as a mechanism for nanoscale interfacial morphology control. By tuning annealing time (or temperature) during sequential thin layer deposition, it is possible that nanoscale morphologies could be created that would simultaneously optimize exciton dissociation and carrier mobility.⁵⁰

Enhancements in device performance have been made by adding a mixed⁵¹ and graded⁵² layer in between the CuPc and C_{60} layers. The increased donor-acceptor interface increases the J_{sc} , but reduces the fill factor due to recombination at these interfaces as well as decreased carrier mobility. A fully-intermixed assembly of CuPc: C_{60} , for example, would lead to strong recombination effects that degrade device performance.⁵³ Incorporation of dewetting and/or phase-separation-controlled structures into the production and processing of OPV devices may lead to improved device performance and stability in this system. This is analogous to extensive considerations of annealing⁵⁴ and solvent-vapor annealing⁵⁵ that have been used for morphology-driven efficiency improvement in solution-phase BHJ growth. One possible strategy would be to use dewetting of C_{60} as a mechanism to create columnar fullerene structures that have recently been reported to allow improvements in BHJ solar cell performance.^{40a} Further characterization of these kinds of film processing strategies for

small molecule films will ideally lead to control of domain sizes in the active layer that is crucial for efficient exciton dissociation and also for control of crystallinity, which is connected to carrier mobility. In particular, a fully-intermixed assembly of CuPc:C₆₀ would lead to strong recombination effects that degrade device performance.⁵³

3.6 Summary and Conclusions

In conclusion, we have combined AFM and NEXAFS to demonstrate dewetting at the technologically-relevant C₆₀:CuPc interface. By considering very thin 2 nm C₆₀ films grown on CuPc, we could combine surface sensitive spectroscopy and real-space imaging to reveal lateral de-wetting due to annealing at 105 °C. This process is to be distinguished from the vertical CuPc segregation proposed to occur for similar CuPc: C₆₀ bilayers.⁴¹ Our combined microscopy and spectroscopy results show that CuPc does not transport vertically to the surface for bilayers with C₆₀. They contribute compelling evidence for the strong tendency toward phase segregation in the C₆₀:CuPc system, even in bulk co-deposited films,³⁸ that needs to be incorporated into new strategies for small molecule solar cell morphology optimization. In particular, the implications of these observations extend beyond vacuum-deposited bilayer photovoltaics to situations where C₆₀ interfaces with solution-grown layers are subjected to solvent-vapor annealing that roughens the C₆₀ surface.⁴⁹ Alternately, a strategy to engineer morphology could use multilayered C₆₀:CuPc with individual layers only ~5-10 nm thick, for which controlled annealing could yield a complex heterostructure with domains the size of the exciton diffusion length. This would improve the fill factor of these

devices and allow for a thicker active layer with a higher J_{sc} , leading to much higher PCE. It is plausible that the lateral dewetting behavior of C_{60} on CuPc is not unique, and may occur for C_{60} bilayers with other donor materials. Finally, it is reasonable also to extrapolate this observation even to the case of mixed fullerene films, whose morphology is likely to be strongly influenced by phase segregation.

3.7 Acknowledgements

This work was equally supported by the U. S. Department of Energy (DE-FG02-98ER45737) and NSF CAREER award DMR-1056861. TM and EHG were at times also supported by GAANN Fellowships.

3.8 Associated Content

Details of quantitative analysis of NEXAFS spectra included in Appendix B.

CHAPTER 4

Towards Single Crystal Hybrid-Carbon Electronics: Impact of Graphene Substrate Defect Density on Copper Phthalocyanine Film Growth

4.1 Preface

This chapter will be comprised of a reproduction of work that was previously published in 2014 in *Crystal Growth & Design*, Vol 14, pages 4394-4401

Coauthors: Terry McAfee, Eliot Gann, Tianshuai Guan, Sean C. Stuart, Jack Rowe, Daniel B. Dougherty, Harald Ade

Department of Physics and Organic and Carbon Electronics Laboratory, North Carolina State University, Raleigh, NC 27695

4.2 Abstract

Graphene has long been recognized as a potential replacement for indium tin oxide as a transparent conducting substrate that may not only be cheaper to manufacture, but also provide mechanical flexibility and templating for preferential organic film growth. Here, we report the discovery that the thin film growth mode and crystal structure of copper phthalocyanine (CuPc), a prototype organic semiconductor, is extremely sensitive to even atomic-scale defects (e.g. steps) on the graphene surface and that high quality films can be grown with a well-defined crystal orientation that should be favorable for optimized solar cell applications. The initial growth involves flat-lying copper phthalocyanine molecules in a

triclinic brickstone crystal with $(01\bar{2})$ orientation. Thicker films on pristine graphite, as well as thin films on lower quality graphene, show an orientational transition to the flat-lying $(11\bar{2})$ -oriented brickstone, which nucleates near film defects and grows in more compact 3D islands. The thickness dependent transition between these two flat-lying crystal orientations is sensitive to substrate defect density since this determines the extent to which initial island elongation along the substrate can alleviate strain in the film. The sensitivity of copper phthalocyanine film morphology demonstrates the extreme importance of graphene substrate quality to controlling organic film growth. The high crystallinity and optimal molecular orientation achieved here implies a new driving force for high performance organic optoelectronics based on substrate-controlled crystal engineering.

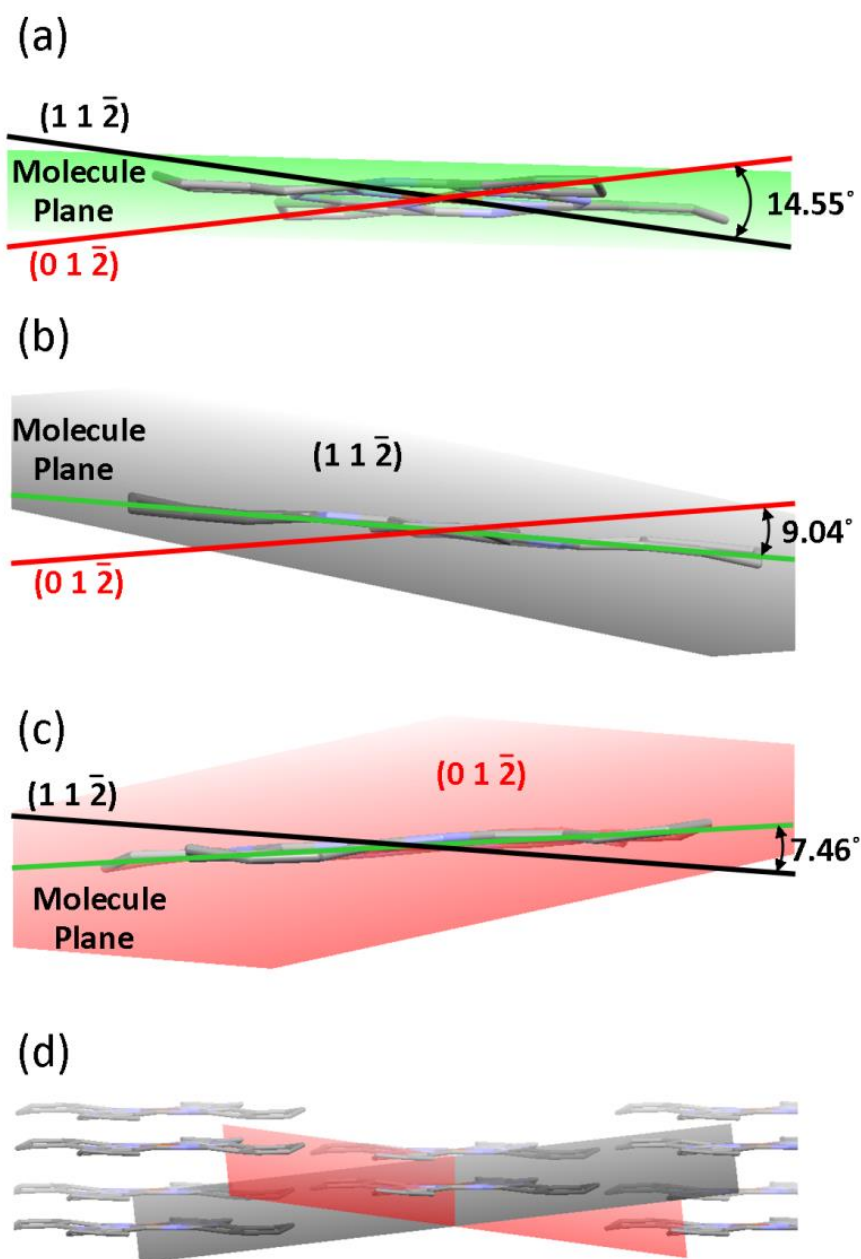


Figure 4.1 Brickstone CuPc Molecular Planes. Illustration of CuPc molecular plane tilt angles in the Brickstone crystal with respect to the $(01\bar{2})$ and $(11\bar{2})$ crystal planes. As viewed parallel to the $(01\bar{2})$ and $(11\bar{2})$ planes (a), $(01\bar{2})$ and molecule plane (b), $(11\bar{2})$ and molecule plane (c). Perspective view of CuPc molecule packing along the $(01\bar{2})$ and $(11\bar{2})$ planes are shown in (d) without indicating the molecule plane.

4.3 Introduction

The growing global need for a cost effective renewable energy source has led to a substantial increase in Organic Photo-Voltaic (OPV) research and solar power conversion efficiency over the past decade.⁵⁶ OPV devices are promising because of their low cost, mechanical flexibility, and light weight properties as well as their often earth-abundant elemental composition. Identifying new transparent conducting electrodes is an important technical challenge in the ongoing development of OPVs especially those that can provide more optimal small molecule film growth than the current standard, Indium Tin Oxide (ITO). ITO, as well as similar traditional transparent conductors, is costly to manufacture, non-flexible, involves scarce elements, and tends to exhibit a rough surface morphology that can be detrimental to film growth. Replacements for ITO considered to date include other metal oxides,⁵⁷ various conducting polymers,⁵⁸ carbon nanotubes, and graphene⁵⁹. Bilayer OPV devices of Ag/Bathocuprine/C₆₀/CuPc/Graphene⁵⁹ show that graphene has the potential as an electrode, but the reduced fill factor and short circuit current strongly suggests that the active layer is far from optimized. Two recent publications report that 50 nm of CuPc deposited on graphene partially adopts a preferred flat lying (01 $\bar{2}$)⁶⁰ and (11 $\bar{2}$)⁶¹ oriented growth of the triclinic brickstone crystal structure⁶² with extensive coexistence of the undesirable standing (100) oriented CuPc alpha phase. Here, we report that the undesirable (100) orientation can be eliminated on low-defect density graphene and that highly crystalline CuPc films can be grown with a uniform flat-lying molecular orientation optimized for solar cell performance gains.

On graphitic carbon, interactions between the substrate and the growing molecular film are strong enough for some molecules to stabilize a "flat-lying" or "face-on" molecular orientation where the aromatic plane of the molecule is parallel to the surface plane. Molecular orientation and crystallite size have a significant impact on the optical absorption cross section, charge transport, and electronic band alignment properties of thin films⁶³, and must be optimized for organic device fabrication.

Molecular orientation is often described as "flat lying" or "face-on" when the aromatic plane is parallel to the substrate and described as "standing" or "edge-on" when the aromatic plane is perpendicular to the substrate. The flat-lying molecular orientation preferentially aligns intermolecular π -overlap interactions with the anode-to-cathode transport direction needed for charge transport in OPV's and enhances light absorption. Finally, the Highest Occupied Molecular Orbital (HOMO) and Lowest Unoccupied Molecular Orbital (LUMO) energy levels are lowered,⁶⁴ which increases the energy gap between charge-separated holes (in the donor) and electrons (in the acceptor), thus increasing the open circuit voltage (V_{oc}) achievable in the device.

In addition to this preferred face-on orientation, it is necessary to optimize film crystallinity for peak device performance.⁶⁵ Charge mobility and recombination are often hindered by grain boundaries and can be improved with larger crystal domains. Larger crystallites are particularly advantageous for OPV devices for this reason, provided that the exciton lifetime allows diffusion to the donor-acceptor interface where charge separation can occur.

The less optimal orientation of “standing” CuPc is commonly observed in films thicker than a monolayer on many substrates, such as silicon⁶⁶, copper,⁶⁷ and ZnO (1 $\bar{1}$ 00)^{62b}. Two crystal structures for standing CuPc, as-grown at room temperature, have been reported as the monoclinic herringbone⁶⁸ (200) and the more recently identified triclinic brickstone^{62a} (100). CuPc has also been reported to partially form the triclinic brickstone in the (01 $\bar{2}$)⁶⁰ and (11 $\bar{2}$)⁶⁰ orientations on graphene, both of which have advantageous flat lying CuPc molecules. The CuPc crystal plane parallel to the substrate is uniquely defined by the Miller Indices of the crystal and is illustrated in Figure 4.1. The (01 $\bar{2}$) and (11 $\bar{2}$) planes of the the brickstone crystal are rotated by 14.6° from one another, and have a tilt angle of the CuPc molecule of ~10° and ~7° from flat-lying with respect to the substrate for the (0 $\bar{1}$ 2) and (11 $\bar{2}$) orientation, respectively. Consequently, both orientations will enhance charge transport and optical absorption in OPV cells.⁶⁹ Fortuitously, face-on molecular stacking of CuPc, as well as many other commonly used organic semiconductors, improves *all* of the performance characteristics in OPV devices.

In this paper, we report the crucial impact of substrate defect density on controlling crystallinity and orientation in CuPc films. We use Atomic Force Microscopy (AFM) and Grazing Incidence Wide-Angle X-ray Scattering (GIWAXS) to characterize the film growth of CuPc on Highly Oriented Pyrolytic Graphite (HOPG) and epitaxial graphene on SiC(0001). By comparison of CuPc film growth on epitaxial graphene on stepped SiC(0001) to that grown on pristine, cleaved HOPG, we observe the impact of substrate defect density on growth of CuPc. On defect-free graphite, CuPc films grow epitaxially in (01 $\bar{2}$) oriented

flat-lying crystals, which form elongated strips due to asymmetric tensile strain. The larger domains of flat graphene on the HOPG surface allows strain relief via elongation in the $(01\bar{2})$ domains, making it the sole crystal growth orientation up to a film thickness of 25 nm. Thicker films, up to 250 nm, exhibit a transition to a flat-lying $(11\bar{2})$ brickstone orientation, and show no evidence of the less desired "standing" (100) CuPc. By contrast, growth of CuPc on graphene on SiC(0001) with numerous atomic step and etch pit defects due to high temperature vacuum processing, shows coexisting flat-lying and standing crystal orientations at all film thicknesses. This comparison has the important implication that the details of active-layer film growth on graphene substrates will be strongly impacted by the substrate quality. A path towards high quality, "single crystal" organic thin film devices can thus be envisioned that depends solely on the achievable quality of the graphene substrates.

4.4 Results

4.4A CuPc Films on Graphene/SiC(0001)

Growth of CuPc/Graphene/SiC(0001) (CuPc/G/SiC) was investigated by GIWAXS and AFM, revealing some similarities and differences to the recent reports of CuPc growth on CVD Graphene⁶⁰⁻⁶¹. The single layer graphene grown from Silicon Carbide on our substrates has flat, defect free, graphene domains ranging from ~10-500 nm in diameter, which arises from the unavoidable miscut from the perfect (0001) plane. This surface exhibits a regular array of triple-bilayer SiC steps (height 0.75 nm) as well as random "etch pits" due to rapid thermal desorption of Si during graphene growth.⁷⁰ The single layer

graphene grown on single crystal SiC(0001) wafers has an added advantage of forming a continuous 2-D single crystal of graphene across the sample with essentially no rotational disorder in the plane of the surface. However, the intrinsic SiC surface steps and etch pits formed during graphene growth by thermal desorption of Si in ultrahigh vacuum give our graphene on SiC(0001) substrates substantially higher defect density than cleaved graphite.

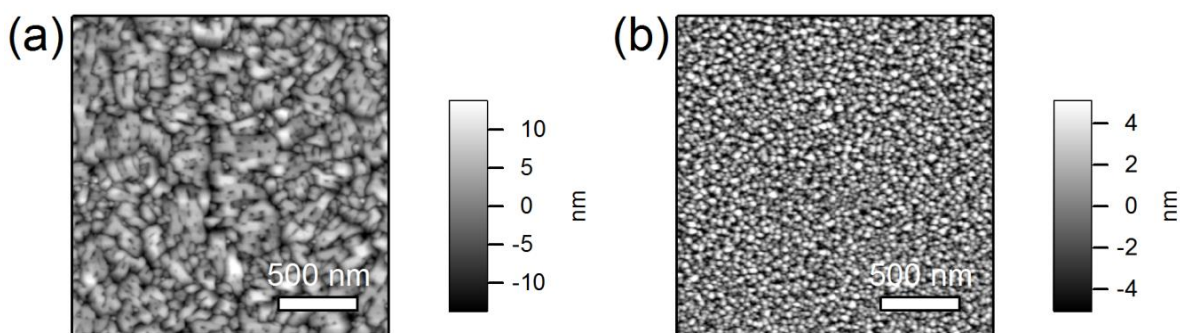


Figure 4.2 AFM of CuPc / Graphene / SiC. 2 μm x 2 μm AFM scan on the same 20 nm CuPc / G / SiC sample at locations separated by less than a centimeter, showing regions with large, $\sim 10\text{-}300$ nm, crystals (a) and small, $\sim 10\text{-}50$ nm, crystals (b).

AFM images of CuPc/G/SiC show a macroscopic inhomogeneity of CuPc domain sizes ranging from $\sim 10 - 300$ nm. Figure 4.2a shows a region of the sample exhibiting relatively large domains, primarily larger than 100 nm in size. The domain morphology resembles that previously reported for annealed films of CuPc on CVD graphene⁶⁰ and HOPG⁷¹. These larger domains were observed several times on multiple samples, but do not represent the typical topography observed for thick films on graphene on SiC. Instead, Figure 4.2b shows the typical topography observed by AFM for CuPc/G/SiC, which has $\sim 10\text{-}50$ nm CuPc domains which corresponds to the size of flat graphene regions available on flat

terraces of the G/SiC substrate used. The inhomogeneity of CuPc domain sizes is attributed to the large variation in the graphene defect density, as epitaxial graphene on SiC prepared in UHV is known to be extremely spatially inhomogeneous.⁷⁰ This is reflected in our AFM measurements shown in Figure 4.2a and 2b that show highly variable film morphology in different macroscopic surface regions.

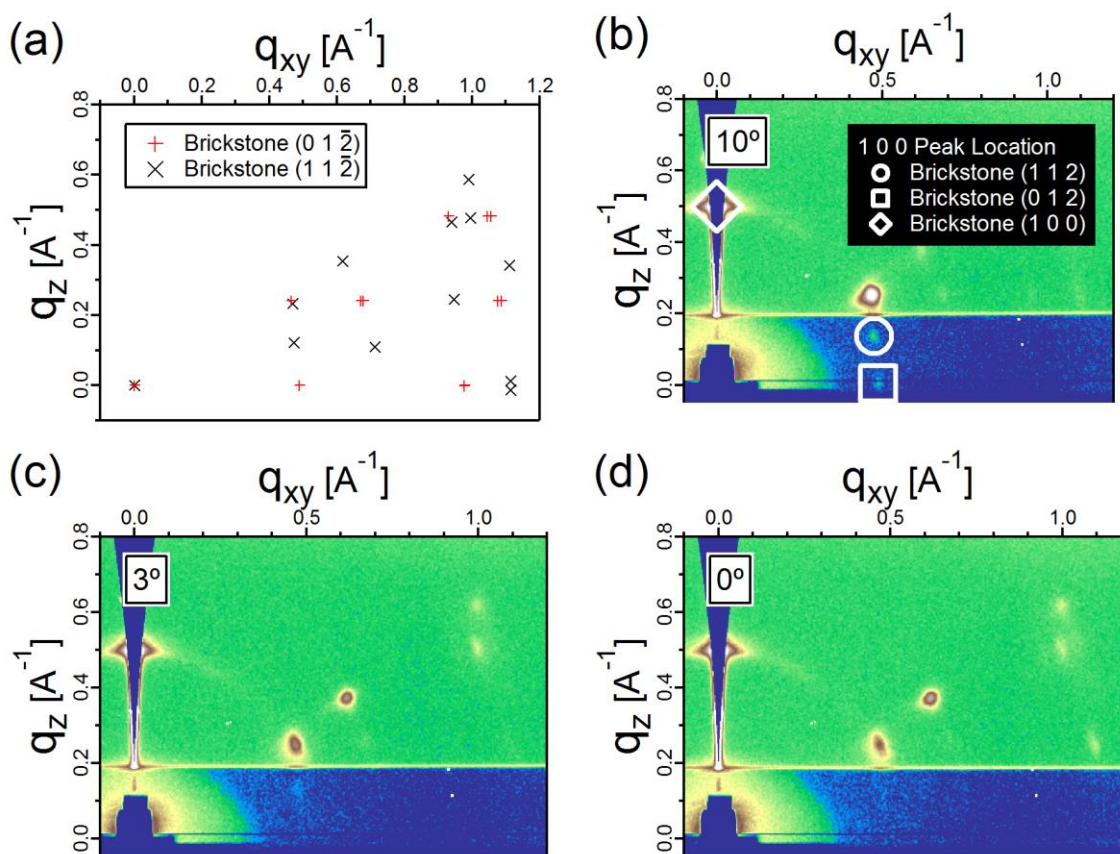


Figure 4.3 Calculated diffraction peaks for CuPc Brickstone $(01\bar{2})$ and $(11\bar{2})$ (a). GIWAXS data, with excluded wedge correction, for 80 nm CuPc/G/SiC with in plane rotation of the sample by (b) 10.0 deg, (c) 3.0 deg, (d) 0.0 deg showing relative peak intensity variation for both the $(01\bar{2})$ and $(11\bar{2})$ brickstone reflections.

To probe the crystalline structure of CuPc/G/SiC, GIWAXS was employed. GIWAXS data was obtained for films of 5 nm, 25 nm, and 80 nm of CuPc deposited on G/SiC, all of which had reflections from *both* the $(11\bar{2})$ and $(01\bar{2})$ orientations of the brickstone crystal structure, as well as the less favorable (100) orientation of the monoclinic crystalline structure. However, only a subset of the reflections from each crystal orientation were observed, suggesting that the CuPc crystallites exhibit ordering in the plane of the substrate, for a large range of film thicknesses. To investigate the in-plane ordering of the CuPc crystal domains, we monitored the GIWAXS peak intensities from the 80 nm CuPc on G/Si sample as a function of azimuthal rotation of 120° in 2° steps. The standing (100) orientation was present for all azimuthal angles, as is evident by the high intensity peak at $Q_z = \sim 0.5 \text{ \AA}^{-1}$, $Q_{xy} = 0.0 \text{ \AA}^{-1}$. The angular dependence of the emergence and disappearance of reflections from the $(11\bar{2})$ and $(01\bar{2})$ brickstone orientations, shown in figure 4.3, necessitates that all crystallites of each species have a fixed in-plane growth direction with respect to the graphene single crystal. The azimuthal dependence of each scattering peak was cyclical in 60° increments (see supplemental data), which means both crystal structures exhibited a six-fold symmetry in the in-plane structure. This observation thus indicates epitaxial CuPc film growth on graphene, which is consistent with low energy electron diffraction observations of ordering in the first monolayer of PdPc on graphite⁷² and graphene.⁷³

4.4B CuPc Films on HOPG

To further investigate the presence of both $(11\bar{2})$ and $(01\bar{2})$ orientations of the brickstone crystal structure observed for all samples of CuPc/G/SiC, and the observed topographic variations shown in figure 4.2, we performed a thickness dependent study of CuPc growth on mechanically-cleaved HOPG. This substrate has roughly an order of magnitude lower defect density and thus larger pristine graphene areas to promote crystalline film growth with optimized flat-lying orientations.

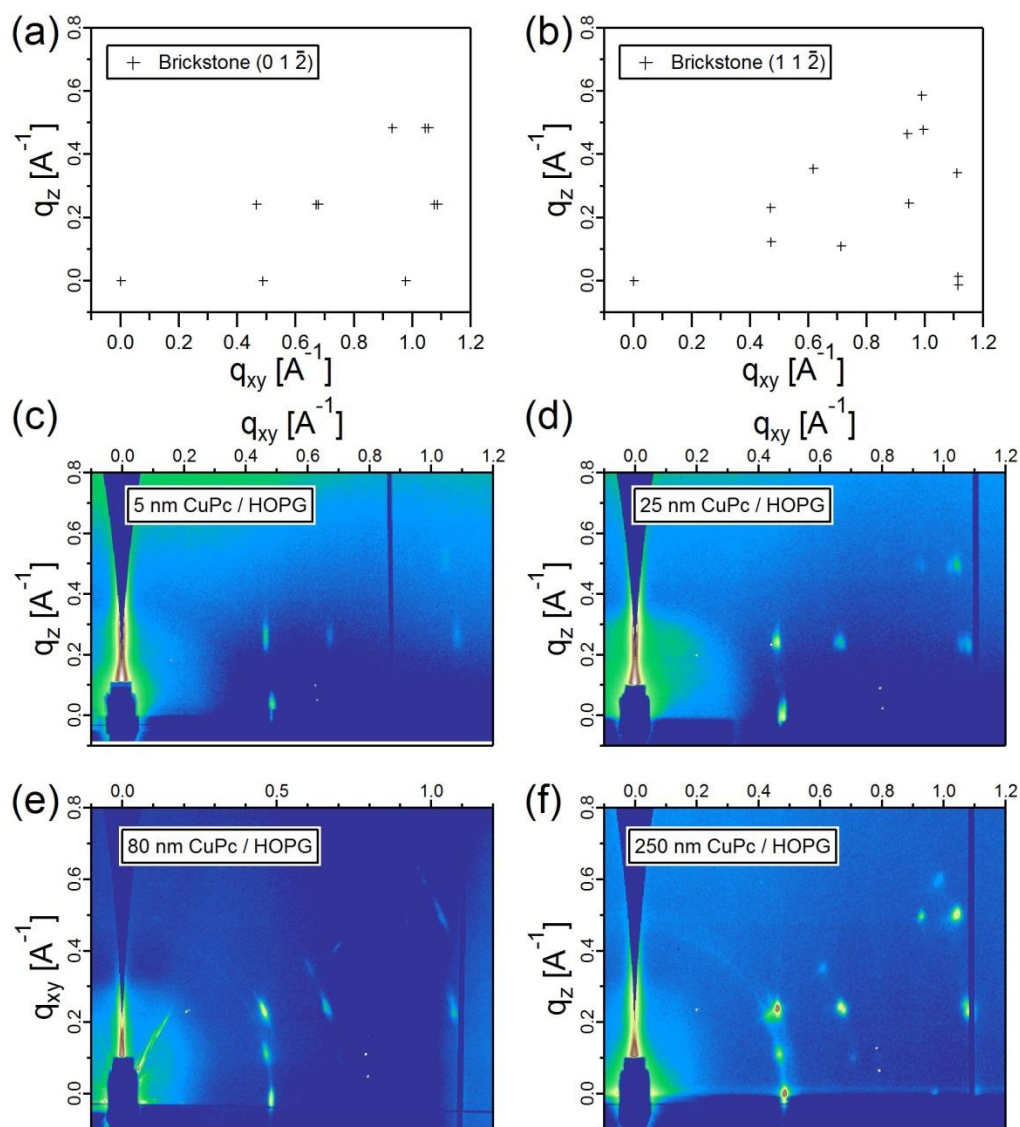


Figure 4.4 Plot of computed diffraction peak locations for CuPc Brickstone (01 $\bar{2}$) (a) and (11 $\bar{2}$) (b) orientations. GIWAXS data, with excluded wedge correction, for (c) 5 nm, (d) 25 nm, (e) 80 nm, and (f) 250 nm CuPc on HOPG.

GIWAXS and AFM were used to determine the structure, orientation, and topography of CuPc crystals formed on HOPG at deposition thicknesses of 5 nm, 25 nm, 80 nm, and 250 nm. Figure 4.4 shows the thickness dependence of the crystal structure for CuPc on HOPG.

A clear evolution of the Brickstone ($01\bar{2}$) orientation transitioning to the Brickstone ($11\bar{2}$) orientation at larger film thickness is observed. The lowest order scattering peak locations for each of these two observed brickstone orientations were calculated and plotted in figure 4.4 (a,b). The samples with 5 nm and 25 nm of CuPc on HOPG show *only* the ($01\bar{2}$) orientation, while the 80 nm and 250 nm films show both orientations of the brickstone crystal structure. Significantly, we point out that films of up to 250 nm of CuPc on the low defect density HOPG show *no evidence* of the disadvantageous edge-on (100) CuPc crystals. This is the first observation of an entirely flat-lying crystalline film of this material at device-relevant thicknesses.

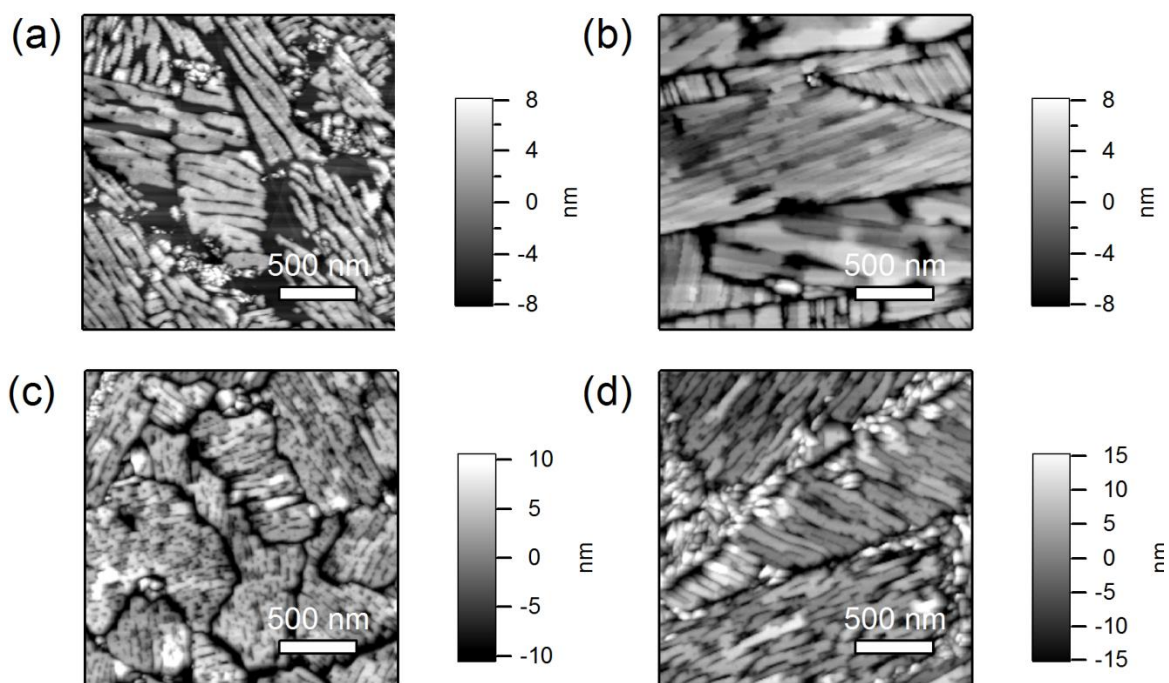


Figure 4.5 AFM of CuPc / HOPG. 2 um x 2 um AFM on films of (a) 5 nm, (b) 20 nm, (c) 80 nm, and (d) 250 nm CuPc on HOPG.

AFM imaging of 5 nm of CuPc grown on HOPG (figure 4.5a) shows that, at these small thicknesses, the substrate is only partially-covered by CuPc domains. This suggests that the CuPc is mobile on the HOPG surface during growth, and is able to aggregate into crystalline domains. Many surface regions without CuPc crystals are associated with defects in the graphene surface, primarily from step edges and step bunches between the basal planes of the HOPG. The initial growth of CuPc on HOPG forms flat, elongated crystal grains that are remarkably semi-parallel to one another, adding to the evidence for epitaxial film growth. At 25 nm of CuPc grown on HOPG (Figure 4.5b) the elongated strips have grown together filling the HOPG domains. Within a crystalline domain the surface is quite flat with small gaps where the individual strips have grown together.

AFM imaging of thicker films of 80 nm and 250 nm CuPc/HOPG (Figure 4.5c,d) shows elongated crystals in regions with large graphene terraces, but the strips are noticeably rougher on the 250 nm sample. Since the $(11\bar{2})$ orientation only begins to form after the $(01\bar{2})$ orientation fills the graphene domains, the $(11\bar{2})$ orientation must be nucleating on top of the $(01\bar{2})$ orientation. We conclude the rougher regions in figure 4.5 c,d are $(11\bar{2})$ oriented crystals, which are primarily present in the smaller domains. This means that as the $(01\bar{2})$ oriented crystal domains continue to grow, they become constrained by the size of the graphene domain in which they have nucleated, and the film instead begins to grow in the $(11\bar{2})$ orientation.

4.5 Discussion

4.5A Mechanism of Substrate Controlled CuPc Film Growth

Despite nearly identical sample fabrication, both $(01\bar{2})$ and $(11\bar{2})$ brickstone orientations have been reported for room temperature growth of CuPc/CVD Graphene⁶⁰⁻⁶¹. This discrepancy, added to our own observations of both crystal orientations over a range of film thicknesses of CuPc/G/SiC forces us to consider the impact of the quality of the graphene substrate at mesoscopic length scales as a crucial factor in controlling film growth. We point out that the CuPc molecular tilt angle with respect to the substrate for both the $(01\bar{2})$ and $(11\bar{2})$ orientations are both nearly perfectly flat lying, meaning that both orientations will enhance charge transport and optical absorption in OPV cells compared to the (100) orientation.

Although HOPG is not transparent, making it unsuitable for device applications, the presence of large pristine graphite domains, an order of magnitude larger in diameter than produced in our G/SiC substrates, permits observations of the characteristics of CuPc film growth on defect-free graphene. For the 5 nm and 25 nm CuPc/HOPG samples, only the $(01\bar{2})$ orientation of the brickstone is present. We also observed a narrow distribution of long, thin, crystalline domains which are semi-parallel to each other within each graphene domain. The elongated shape of initial CuPc islands is very important to consider in understanding the growth and evolution of these films. Numerous inorganic heteroepitaxial systems involving strained island growth show elongated islands arising either from minimization of strain energy in the growing island as described by Tersoff and Tromp⁷⁴ or

from kinetic effects.⁷⁵ The prevalence of elongated islands in strained layer growth under a variety of circumstances permits the qualitative conclusion that strain is important in the initial film morphology in this system. In addition, the more compact nature of the $(11\bar{2})$ domains that appear after the orientation transition suggests that they are not as strained. This implies that strain relief is likely an important factor in the thickness dependent orientation transition that we observe.

To evaluate the competition of strain relief mechanisms of elongated crystal growth and a crystal orientation transition, we consider the strain relationships at the epitaxial interfaces. First layer growth of CuPc on Graphene, imaged directly with single molecule resolution using Scanning Tunneling Microscopy, has been reported to form a wetting layer of perfectly face-on CuPc molecules arranged in a nearly square 2-D lattice with dimensions of 1.369 nm x 1.496 nm.⁷⁶ Combining our observations from CuPc/HOPG with the observation of epitaxial growth of CuPc/G/SiC, we can form a more complete picture of the orientation of CuPc molecules as successive film is grown upon the wetting layer. For epitaxial growth of the $(01\bar{2})$ brickstone, we calculate the strain from lattice mismatch with the CuPc wetting layer. A relaxed $(01\bar{2})$ plane has CuPc molecule spacings of 1.289 nm x 1.351 nm at an included angle of 89.3 degrees, leading to a tensile strain of 5.9% and 9.7%. The strain is high compared to inorganic epitaxial growth conditions, but the CuPc molecules are also able to change their tilt angle to relieve stress and achieve lattice matching. We assert that the elongated islands (Figure 4.5) arise from the asymmetry in strain, resulting in preferred growth in the low strain direction. As films grow thicker, subsequent layers of a

given elongated $(01\bar{2})$ crystal relax toward the unstrained crystal unit cell and islands elongate in the plane of the substrate. When island elongation is impeded by substrate defects, it becomes favorable to relieve strain by nucleating the $(11\bar{2})$ orientation which has an intermolecular spacing of 1.351 nm in common with a spacing in the bulk $(01\bar{2})$ plane.

This picture explains the presence of the $(11\bar{2})$ brickstone orientation for all thicknesses of CuPc grown on G/SiC. On the G/SiC substrate, small graphene domains immediately inhibit the mechanism of strain relief by the elongated $(01\bar{2})$ growth. The GIWAXS experimental observation of both flat-lying $(01\bar{2})$ and $(11\bar{2})$ CuPc orientations for even the 5 nm CuPc/SLG/SiC sample is the strongest evidence for our claim that the transition from the $(01\bar{2})$ to the $(11\bar{2})$ brickstone orientations is intimately tied to the extended or mesoscale defect (e.g. step and/or etch pit) density of the graphene substrate. From this observation, we conclude that the achievable CuPc film thickness of single crystal brickstone $(01\bar{2})$ oriented domains is limited by the lateral size of defect-free graphene available on the substrate. In addition to controlling the thickness dependence of the $(01\bar{2})$ to $(11\bar{2})$ orientation transition, extended defects also evidently promote the nucleation of unfavorable (100) crystal orientations in our experiments on G/SiC. The standing (100) growth mode of CuPc is dominant when the molecule-molecule interactions exceed the molecule-substrate interactions. We thus infer the (100) growth mode would occur for film thickness $\gg 250$ nm on pristine graphene, and for all thicknesses grown on graphene with extremely high defect density. This general picture agrees well with recent investigations of

CuPc growth on other graphene substrates for which mesoscale defect density may be significant and allow different growth modes.⁶⁰⁻⁶¹

4.5B Implications for Organic Photovoltaics

Regarding the use of graphene as a transparent electrode, substrate quality is crucial just as it is when considering ITO for the same purpose. In the case of graphene, however, *both* the CuPc (01 $\bar{2}$) orientation of the Brickstone crystal associated with pristine substrate domains and the (11 $\bar{2}$) orientation induced by the need for strain relief in the presence of substrate defects are expected to show significant advantages over the typical standing orientations found for growth on ITO and conducting polymer substrates. Graphene defect density is a major controlling factor in CuPc film growth, but graphene is *always* advantageous as a substrate from the perspective of molecular orientation-based optimization of light absorption and charge extraction. Furthermore, low defect density graphene allows CuPc crystalline domains of more than a micrometer in lateral size and at least 25 nm in height, which would result in a significant reduction in crystallite domain boundaries in films for device applications.

For high performance bilayer OPV devices employing CuPc / graphene interfaces, domains of graphene must be uniformly distributed over the entire device area. The remaining challenge is that the (0 $\bar{1}2$) orientation often has large gaps between domains (Figure 4.5) that might be filled by the subsequent growth of an acceptor layer. This could potentially lead to continuous pathways between electrodes in the same material that reduce

the fill factor of the device. The $(11\bar{2})$ orientation, however, does not have gaps on these scales and has an advantageous surface roughness on the size scale of the exciton diffusion length. The epitaxial growth of the $(11\bar{2})$ oriented crystals on top of the $(01\bar{2})$ oriented crystals indicates that significant orbital interaction between CuPc molecules still occurs at the interface and would not necessarily significantly reduce charge mobility. The dependence of the transition to the $(11\bar{2})$ orientation on the graphene defect density can be exploited to create a CuPc bilayer OPV device with an optimized CuPc layer. If achieved, the nearly flat lying CuPc film would have higher light absorption increasing the short circuit current, lowered HOMO energy levels increasing the open circuit voltage, and the continuous crystal networks will have improved charge mobility and reduction in trap states, improving the fill factor. Doping of the graphene to modify its work function may also improve the fill factor by increasing the charge carrier tunneling asymmetry between holes and electrons at the CuPc/Graphene interface, which is often achieved on ITO by using a PEDOT:PSS layer.

4.6 Conclusion

The critical observation of this work is that CuPc film crystal texture and morphology on graphitic substrates are very sensitive to the density of mesoscale substrate defects. By using cleaved, low defect density graphite substrates, we have achieved flat-lying, crystalline orientations in films as thick as 250 nm, with *no* measured contamination from unfavorable standing orientations. We observe flat-lying CuPc films grown on graphene and graphite to have a transition with increasing film thickness between an initial triclinic “brickstone”

structure with $(01\bar{2})$ -oriented crystals to a secondary $(11\bar{2})$ -oriented brickstone. The critical thickness for this orientation transition is determined by the defect density of the graphene substrate surface, and reflects a competition between strain relief by island elongation and strain relief by nucleation of the second film orientation. The presence of surface steps, step bunches, etch pits, or crystalline domain boundaries favor nucleation of the $(11\bar{2})$ orientation of the triclinic brickstone crystal structure as a mechanism of strain relief when island elongation is impeded. This implies a major role for even relatively minor surface defects beyond the roughness effects previously reported for organic films on sputtered graphene⁷⁷.

The effect of the quality of the graphene substrate on the CuPc thin film morphology and crystal structure could plausibly be extrapolated to other organic films on graphene, especially those with planar aromatic groups⁷⁸. With the many methods of transparent graphene electrode production currently being explored for organic device applications, such as CVD graphene⁷⁹, functionalized graphene⁸⁰, and solution-cast graphene⁸¹, we show that it is crucial to consider how the distribution of extended defects like steps, wrinkles and etch pits on graphene will impact the properties of subsequent thin film formation. Notable among the graphene variants under heavy investigation in recent years is epitaxial graphene on SiC⁸² which is a platform that is intrinsically highly crystalline and also transparent to visible light. With this variety of high performance graphene as a substrate, we envision the use of highly crystalline organic semiconductor films with optimal charge carrier mobilities for improved solar cell efficiency. More generally, this work makes clear that graphene is a strong candidate for broader use as a transparent electrode in OPV's and other optoelectronic

devices. In particular, the dependence of organic film growth on fine details of substrate quality present new opportunities for control of morphology and crystallinity that can be used to optimize OPV performance. The high quality growth achievable changes the perspective on organic optoelectronics from "dirty" devices dominated by disorder and complexity, to devices in which crystallinity leads to high performance, analogous to the more traditional inorganic semiconductors.

4.7 Experimental Methods

CuPc (95%) was obtained from Sigma-Aldrich and loaded, as received, into a boron nitride crucible, followed by several hours of outgassing in high vacuum prior to film growth. Graphene was grown from Silicon Carbide using the standard van Bommel UHV-growth method described in detail in a separate paper.⁷⁰ Substrates were exposed to air for ~ 5 minutes while transferring to the CuPc film deposition chamber. HOPG was exfoliated using scotch tape immediately before loading into the CuPc deposition chamber. CuPc thin films were grown using thermal evaporation at pressure $< 2.0 \times 10^{-6}$ torr in a high vacuum chamber with a base pressure of 10^{-9} torr. Deposition rates, monitored using a quartz crystal microbalance, between 0.01 Å/s and 6.0 Å/s, typically 0.25 Å/s, were used during film growth. AFM was carried out in non-contact mode in air using a commercial instrument (Asylum Research MFP-3D). Commercial AFM tips (Budget Sensors, Tap300AL-G) had a nominal radius of ~ 10 nm and a nominal resonant frequency of ~ 300 kHz. To investigate the possibility of film morphology changes due to air exposure, AFM was

typically performed directly following film growth. AFM data was also acquired on the same samples several weeks later following GIWAXS measurements, and no topography changes were observed.

GIWAXS data was acquired at beamline 7.3.3 at the Advanced Light Source³² at grazing angles between 0.10° and 0.20° above the plane of the substrate. Azimuthal rotation of the 80 nm CuPc/G/SiC was collected over 120° in 2° steps. For data acquired on HOPG substrates, the x-rays were incident on a region of the substrate that was visibly flat, uniform, and did not contain flakes. GIWAXS samples were inside a Helium enclosure during data acquisition to minimize air scattering and x-ray induced oxidation. A comparison of an initial short x-ray exposure of ~ 1 s with consecutive exposures of ~ 20 seconds was performed for several film thicknesses on both HOPG and G/SiC substrates, and did not show any evidence of x-ray induced morphology changes. Reciprocal space peak locations, shown in figure 4.2 a,b and figure 4.4a, were calculated using equations from reference⁸³ with lattice parameters from Cruickshank et al.^{62b} for the CuPc brickstone crystal structure of $a = 12.886 \text{ \AA}$, $b = 3.769 \text{ \AA}$, $c = 12.061 \text{ \AA}$, $\alpha = 96.22^\circ$, $\beta = 90.62^\circ$, $\gamma = 90.32^\circ$. The geometrically excluded wedge arises from the experimental necessity of having a fixed beam incidence near the critical angle of the film with respect to the sample, which only allows data on the Qz axis as would be collected with standard x-ray diffraction Θ - 2Θ scans, where the incident and scattered light are at the same angle.

4.8 Funding

This work was equally supported by the U. S. Department of Energy (DE-FG02-98ER45737) and NSF CAREER award DMR-1056861. TM and EHG were partially supported by GAANN Fellowships.

CHAPTER 5

Layer-by-Layer Growth of Crystalline C₆₀ Films on Flat-Lying Copper Phthalocyanine

5.1 Preface

This chapter will be comprised of a reproduction of work that has been submitted for publication in *The Journal of Materials Chemistry A*

Coauthors: Terry McAfee, Aubrey Apperson, Harald Ade, Daniel B. Dougherty

Department of Physics and Organic and Carbon Electronics Laboratory, North Carolina State University, Raleigh, NC 27695

5.2 Abstract

We observe layer-by-layer growth of fcc(111) films of fullerene-C₆₀ on top of crystalline flat-lying CuPc film structures on graphite using combined grazing incidence wide-angle x-ray scattering and atomic force microscopy. Such a morphology is nearly ideal for bilayer films of C₆₀ / CuPc in solar cells. Very similar crystallinity and morphology is observed when varying the film thickness of either material from 5 nm up to more than 100 nm, suggesting that this advantageous solar cell morphology is not only robust, but may actually be preferred compared to the typical mounded fullerene morphology often seen on standing, edge-on aromatic film substrates. The large, ordered domains observed in both materials and the co-facial interface should greatly increase charge carrier mobility leading to increased Fill factor. We envision that bilayer films, such as described here, grown on very

high quality graphene as a transparent conducting electrode would simultaneously optimize crystallinity and molecular orientation for peak solar cell performance.

5.3 Introduction

Small molecule organic semiconductors initiated the field of organic photovoltaics¹² (OPVs) and, in the donor-acceptor bilayer device architecture, provided some of the first glimpses of the upward efficiency trends that persist to this day.^{14, 84} With the advent of new molecules with tunable ionization potentials and good optical absorption properties⁸⁵ as well as novel tandem,⁸⁶ p-i-n,⁸⁷ and graded device architectures,³⁷ progress toward competitive efficiencies is promising.

Most of the advances in small molecule OPVs use molecular beam deposition to, in principle, allow very precise film thickness control down to the single molecular layer. There are advantages to be gained by creating very flat donor-acceptor (D-A) interfaces between highly crystalline materials that reduce carrier recombination losses compared to intermixed D-A films.⁸⁸ The value of this possibility is contingent upon a layer-by-layer film growth mode. Otherwise, molecular-scale thickness control is not spatially-uniform over the large areas needed for device applications.

Surprisingly, there are relatively few examples of very flat layer-by-layer growth modes in organic donor-acceptor bilayers. Often interfacial energies between donor and acceptor layers lead to a strong tendency for dewetting⁸⁹ or phase separation.^{38, 41, 90} Since intermolecular interactions are generally weak in organic molecular materials, it is rare that

donor-acceptor interactions are strong enough to stabilize a layer-by-layer growth mode without tipping the balance toward intermixing⁹¹ that would create a non-abrupt (graded) interface. Moreover, kinetic roughening of organic films during growth can lead to a rough donor film which subsequently templates a similarly rough acceptor film.⁸⁹

Interfacial energetics are particularly unfavorable for fullerene acceptor films which have a reasonably strong cohesive energy and relatively weak interaction with substrate molecules. Moreover, nearly isotropic fullerenes tend to have a steric incompatibility with planar aromatic donor molecules and a strong tendency for phase separation even in bulk mixtures.⁹¹ Fullerene films grown on top of pentacene consist of crystallites of only tens of nanometers in diameter.⁴³ A similar morphology is seen for C₆₀ films on top of copper phthalocyanine (CuPc) films grown on SiO₂ and the tendency for dewetting can be greatly accelerated by only modest thermal annealing.⁹² We have argued in the past that controlled dewetting might be of interest for nanometer scale film morphology engineering.⁹² However, it is not yet known what particular morphology will be optimal for organic electronic devices and we also need the versatility to create ultra-flat, abrupt donor-acceptor interfaces.

Within a bilayer device geometry (as in bulk heterojunction devices), it is crucial to understand and control relative molecular orientation at donor-acceptor interfaces. This is necessary to allow the most efficient charge transfer across the interface since excited state coupling is strongly orientation dependent. The general intuition is that a co-facial orientation in which π electron clouds are well-coupled promotes charge separation.^{69, 93} However, one also needs to balance efficient coupling with the possibility of detrimental

geminate recombination across the interface.^{49, 94} This makes the evaluation of orientation controlled bilayers one of the most important problems in organic electronic materials, particularly when the added question of D-A intermixing at the buried interface is considered.⁹⁵

In this paper, we present observations of a layer-by layer growth mode of crystalline C₆₀ films on top of flat-lying CuPc films on graphite that establish a robust co-facial orientation at the donor-acceptor interface. We take advantage of CuPc films reported previously on graphite,⁹⁶ with large crystalline domains the size of which is limited primarily by the substrate defect density. On top of these films, we grow C₆₀ that exhibits comparable long-range crystalline ordering and flat surface morphology that is stable to extensive annealing at 150 °C. Crystal structure is inferred from GIWAXS and reveals an expected fcc (111) oriented film alongside a coexisting (122) orientation induced by substrate defects. Atomic force microscopy images show that the C₆₀ films exhibit very flat terraces on top of CuPc domains with steps heights only on the order of a single molecule. This donor-acceptor film structure and morphology enables a stable and abrupt co-facial interface between CuPc and C₆₀ and could be used in operational solar cells employing graphene as a transparent electrode. More immediately, this is an important model experimental system for the ongoing assessment of the nature of co-facial interaction between fullerene acceptors and aromatic donors.^{69, 93}

5.4 Experimental Methods

C₆₀ (98%) and CuPc (95%) was obtained from Sigma-Aldrich and loaded, as received, into quartz and boron nitride crucibles, respectively. The crucibles were then outgassed for ~24 hours in high vacuum prior to film growth. HOPG was exfoliated using scotch tape immediately before loading into the deposition chamber. C₆₀ and CuPc thin films were grown using thermal evaporation at pressure $< 2.0 \times 10^{-6}$ torr in a high vacuum chamber with a base pressure of 10^{-9} torr. Deposition rates, monitored using a quartz crystal microbalance, between 0.01Å/s and 0.2Å/s, typically .05Å/s, were used during film growth. AFM was carried out in AC mode in air using a commercial instrument (Asylum Research MFP-3D). Commercial AFM tips (Budget Sensors, Tap300AL-G) had a nominal radius of ~ 10 nm and a nominal resonant frequency of ~ 300 kHz. Annealing was performed in a dry nitrogen glove box with less than 0.1 ppm O₂ and H₂O.

GIWAXS data was acquired at beamline 7.3.3 at the Advanced Light Source³² at grazing angles between 0.10° and 0.20° above the plane of the substrate. For data acquired on HOPG substrates, the x-rays were incident on a region of the substrate that was visibly flat, uniform, and did not contain flakes. To make the C₆₀ scattering peak at $Q_{xy} = 0 \text{ \AA}^{-1}$ and $Q_z = 0.767 \text{ \AA}^{-1}$ visible to the reader, missing wedge corrections of the GIWAXS data has been omitted.

5.5 Results

Figure 5.1 shows a series of AFM images of C60 films of different thicknesses grown on CuPc/HOPG. Overall, the C60 film morphology tracks the CuPc film well along the striped subdomains. The lateral size of a given C60 domain is primarily limited by the size of the flat CuPc subdomain it forms on. CuPc film morphology and roughness is determined by the quality of the graphene or graphite substrate, which is described previously,⁹⁶ Although further study of the morphology dependence of neat CuPc films on defects in graphitic substrates is needed to avoid electrical shorts due to the cracks between CuPc domains, subsequently adding C60 should not introduce any additional obstacles for OPV devices.

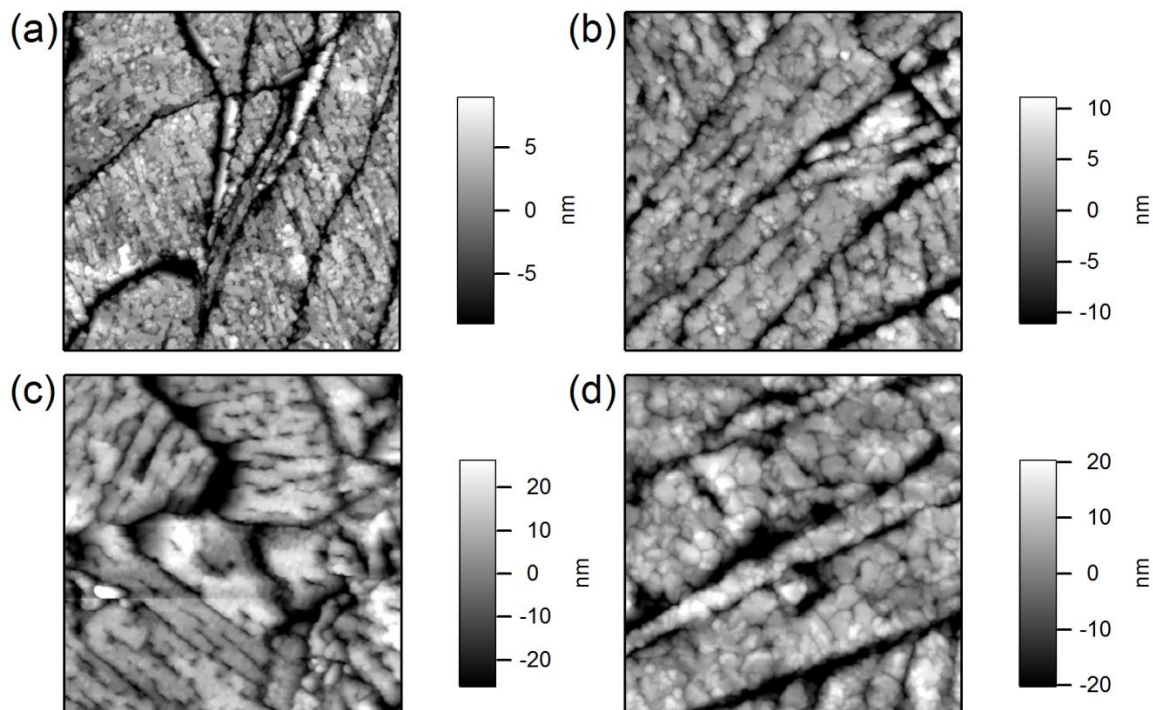


Figure 5.1 Thickness Dependent AFM of C_{60} / CuPc / HOPG. $2 \mu\text{m} \times 2 \mu\text{m}$ AFM on a) 5.5 nm C_{60} / 25 nm CuPc / HOPG, b) 30 nm C_{60} / 25 nm CuPc / HOPG, c) 30 nm C_{60} / 150 nm CuPc / HOPG, d) 150 nm C_{60} / 25 nm CuPc / HOPG

In Figure 5.2, we report GIWAXS data for the films shown in Figure 5.1. Distinct spots in the scattering pattern indicate good crystallinity in the fullerene films. Moreover, the pattern is independent of thickness and does not show any trace of the ring-like features characteristic of typical poorly-crystalline fullerene films with a large distribution of orientations with respect to the substrate plane.

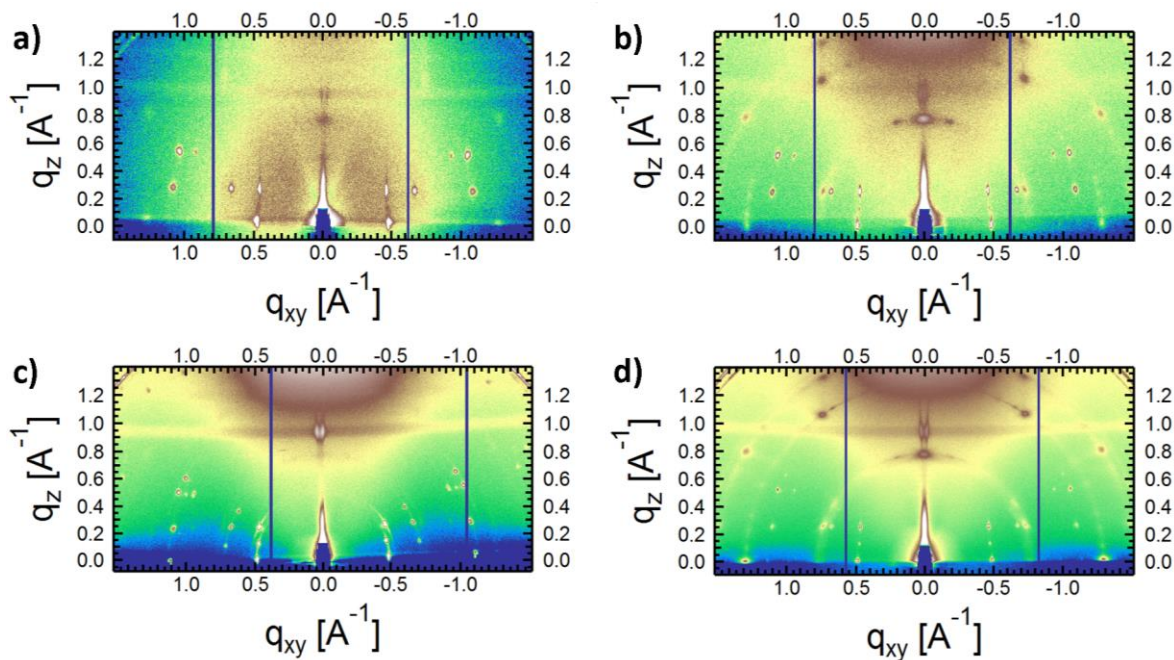


Figure 5.2 GIWAXS acquired at 0.15 Deg incidence angle on a) 5.5 nm C₆₀ / 25 nm CuPc / HOPG, b) 30 nm C₆₀ / 25 nm CuPc / HOPG, c) 30 nm C₆₀ / 150 nm CuPc / HOPG, d) 150 nm C₆₀ / 25 nm CuPc / HOPG.

Simulation of the diffraction pattern can be achieved by assigning the film as an fcc fullerene film with coexisting (111) and (122) orientations parallel to the substrate plane. Simulated diffraction patterns, excluding forbidden reflections, for the observed crystal orientations for C₆₀ and CuPc are shown in Figure 5.3. The sharp double peak and horizontal stripe centered at $Q_{xy} \sim 0 \text{ \AA}^{-1}$ and $Q_z \sim 0.95 \text{ \AA}^{-1}$ as well as the diffuse corona directly above it, centered at $Q_{xy} = 0 \text{ \AA}^{-1}$ and $Q_z \sim 0.95 \text{ \AA}^{-1}$, are scattering from the HOPG substrate. The [111] reflection of the (111) orientation is seen at $Q_{xy} = 0 \text{ \AA}^{-1}$ and $Q_z = 0.767 \text{ \AA}^{-1}$. The [111] reflection of the (122) orientation is seen at $Q_{xy} = 0.209 \text{ \AA}^{-1}$ and $Q_z = 0.738 \text{ \AA}^{-1}$. We find that the relative intensity ratio of these two reflections is the same for all

samples to within our experimental sensitivity, showing that there is no strong thickness dependence to the creation of the coexisting orientations.

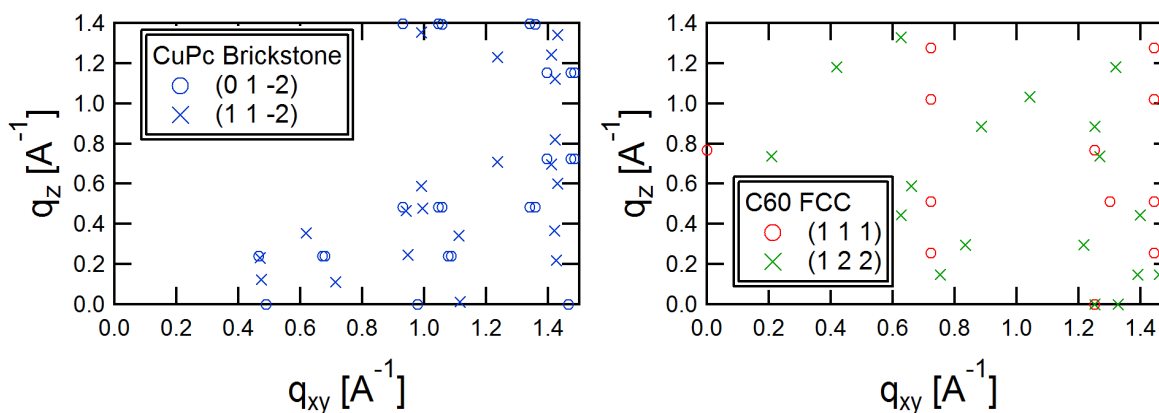


Figure 5.3 Calculated GIWAXS scattering peak locations for CuPc Brickstone (0 1 - 2) and (1 1 2) crystals [Left], and C₆₀ FCC (1 1 1) and (1 2 2) [Right]

The (111) orientation has been previously reported for similar C₆₀ films of a fixed thickness on CuPc / HOPG.^{93b} Our data indicates an unusual (122) orientation also exists which we presume is nucleated at defects. The AFM data in Figure 5.1 clearly shows two distinct morphological features in the form of large flat domains as well as smaller granular features. Correlation to the GIWAXS data strongly suggests that the flat domains are the (111) orientation and the more granular features are the (122), which are evidently less prevalent in terms of area coverage.

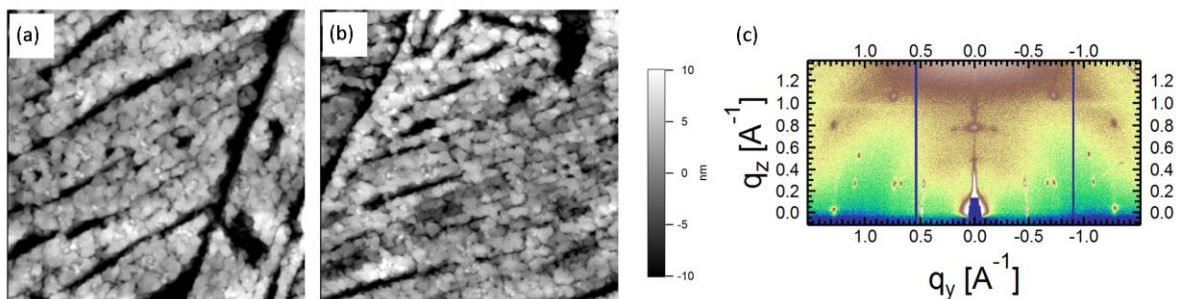


Figure 5.4 Thermal Stability. 2 $\mu\text{m} \times 2 \mu\text{m}$ AFM data on both a) As-Grown and b) post-annealing at 150°C for 24 hrs, and c) GIWAXS data (post-annealing at 150°C for 24 hrs), all acquired on the same 30 nm C_{60} / 25 nm CuPc / HOPG sample.

Figure 5.4 demonstrates the crucial new observation of the thermal stability of C_{60} films when grown on flat-lying CuPc. A 30 nm C_{60} / 150 nm CuPc / HOPG film was characterized by AFM both as-grown, shown in figure 5.4 a), and after annealing at 105°C for 48 hrs, with no apparent changes to the topography. The same sample was further annealed at 150°C for 24 hrs, and characterized by AFM, shown in figure 5.4 b), as well as by GIWAXS, shown in figure 5.4 c), showing no evidence of a surface nor bulk morphology change due to annealing. This is in dramatic contrast to our previous observations of thermal dewetting that results in C_{60} mound coarsening on CuPc/Si substrates.⁹²

5.6 Discussion

Both AFM and GIWAXS show that the C_{60} film morphology and crystallinity and mosaicity is essentially the same for 5.5, 30, and 150 nm C_{60} / 30 nm CuPc / HOPG, as well as for 30 nm C_{60} / 150 nm CuPc / HOPG. This thickness independence typifies a layer-by-layer growth mode of fullerene $-\text{C}_{60}$ on flat CuPc that is not commonly observed in donor-

acceptor bilayers. Most importantly, the film morphology is very stable to thermal annealing, indicating a relatively strong cofacial interaction at the flat donor-acceptor interface compared to other edge-on films.⁹² In particular, the fact that the film morphology is very insensitive to annealing means that there is no significant driving force for intermixing at the interface in this system. Given the observation of this unusual organic film growth mode, it is worthwhile to recount the arguments in favor of a single D-A interface geometry for organic solar cells.

At present, world record power conversion efficiencies for organic solar cells are achieved using the blended polymer-fullerene bulk heterojunction approach.³⁴ The rationale for this film morphology is to control mesoscale donor-acceptor domain sizes to promote efficient exciton dissociation at D-A interfaces. Domains are engineered to match exciton diffusion lengths so that almost all photo excitations can find their way to an interface before recombining.

However, achieving efficient dissociation of excitons is useless if the charges are not able to transport to the electrode. Typically, once a free hole (electron) is in a donor (acceptor) domain it is not energetically favorable to transfer to the other material. Thus, a continuous pathway to the electrodes is needed for both the donor and acceptor materials. It is challenging to ensure such continuous pathways in BHJ devices. Without numerous percolation paths to the electrodes, charges can become trapped, leading to bimolecular recombination. This makes it challenging to simultaneously optimize both exciton dissociation and bimolecular recombination in a BHJ device.

The layered and crystalline features of the C_{60} / CuPc bilayer films we have created represent a possible alternate approach to meeting this challenge. The large, flat, 3D, single crystal island growth in both the CuPc and C_{60} is advantageous for minimizing recombination. The charges from dissociated excitons not only have a continuous path to the electrode in the donor/acceptor material, the shortest path to the electrode is located within a *single-crystal* domain. This means that charge traps and bimolecular recombination will be limited by charge extraction at the electrodes, which can be easily improved with choice of electron/hole blocking layers and choice of metal for the cathode.

For this reason, we consider it still an open question to what extent bilayer devices can be further improved for organic solar cell technology. Charge transport can be efficient and bimolecular recombination suppressed in a bilayer. However, exciton dissociation will be much less efficient than in a BHJ. Our results here and in our previous CuPc/graphene study⁹⁶ also indicate the importance of using very high quality substrates for optimizing crystalline order in small molecule OPV materials. Both for fullerene films and the CuPc substrates on which they are grown, preexisting defects on growth substrates can nucleate secondary crystal orientations. The resulting disorder is unfavorable for charge transport and needs to be avoided. Similar recent observations for pentacene film growth on graphene suggest that these ideas are broadly applicable to small molecule films grown on graphitic substrates.⁹⁷

Thus, an organic solar cell technology based on D-A bilayer will look much more like traditional photovoltaic technologies where crystalline materials are important and single “p-

n” junctions are used to establish a built-in electric field. In highly crystalline bilayer device, we will still need to use the chemical potential difference at the D-A interface to dissociate excitons. In the current state of the art, we still need to improve carrier mobilities and exciton diffusion lengths in both donor and acceptor materials. However, this device morphology has advantages in terms of recombination losses as already mentioned and also lends itself to efficiency improvements through the use tandem cell construction.⁸⁶

The stability of this system under thermal annealing indicates a distinct advantage to OPV device longevity compared to typical fullerene based BHJ films. First, it demonstrates that the co-facial C₆₀:CuPc interface interaction not only induces layer-by-layer growth of the C₆₀ film, but is also in a preferred, thermally stable, equilibrium. It has been shown⁹⁸ that a major source of degradation in C₆₀ films is due to UV-induced polymerization of the C₆₀, which has been demonstrated to be reversible when annealed at 110 °C.^{90b} Our films are compatible with this annealing treatment, unlike typical, quasi-stable,-fullerene BHJ films which undergo morphological changes under annealing at 110 °C.⁹⁹

5.7 Summary and Conclusions

In summary we report layer-by-layer growth of fcc fullerene-C₆₀ films on flat-lying CuPc films on graphite. This contrasts sharply with the typical granular, polycrystalline C₆₀ film morphology found on edge-on organic film substrates.^{43, 92} We observe that the C₆₀ film morphology remains the same for 5.5, 30, and 150 nm C₆₀ / 30 nm CuPc / HOPG, as well as for 30 nm C₆₀ / 150 nm CuPc / HOPG. There is only minor crystalline disorder in the form

of an alternate fcc (122) orientation with respect to the substrate plane, which we believe is related to nucleation at substrate defects. Most importantly, we observe no tendency for fullerene dewetting, even after annealing. This very stable layer-by-layer growth mode indicates a strong interaction at the D/A interface. This is consistent with the general intuition in the organic photovoltaic community about the value of co-facial interactions between planar aromatic species and fullerenes to enhance coupling for OPVs.^{69, 93}

These observations are important for confirming that co-facial interactions between C₆₀ and CuPc can be relatively strong and possibly promote efficient charge transfer in OPVs. In addition, the high crystalline quality of both donor and acceptor films points to very efficient charge transport after separation that is likely to minimize bimolecular recombination. If the recent trend of improving small molecule film quality continues, it will be worthwhile to consider whether the simplest bilayer OPV architecture should be re-visited and explored in functioning devices.

5.8 Acknowledgements

This work was equally supported by the U. S. Department of Energy (DE-FG02-98ER45737) and NSF CAREER award DMR-1056861 for characterization and growth, respectively. TM was partially supported by GAANN Fellowships.

CHAPTER 6

Morphological, Optical, and Electronic properties of three distinct crystal orientations present in a Beta CuPc thin film

6.1 Preface

This chapter will be comprised of work which is to be submitted to a peer reviewed journal for publication.

Coauthors: *Terry McAfee*^{*}, *Benjamin Hoffman*^{*}, *Xiao You*^{**}, *Joanna Atkin*^{***}, *Harald Ade*^{*}, *Daniel B. Dougherty*^{*}

^{*}Department of Physics and Organic and Carbon Electronics Laboratory, North Carolina State University, Raleigh, NC 27695

^{**} Department of Applied Physical Science, University of North Carolina at Chapel Hill, Chapel Hill, NC 27599-3216

^{***} Joanna Atkin, Department of Chemistry, University of North Carolina at Chapel Hill, Chapel Hill, NC 27599-3216

6.2 Abstract

Organic semiconducting small molecule Copper Phthalocyanine is used in many organic electronic devices, including photovoltaics, thin film transistors, and light emitting diodes. In this report we investigate the structural, optical, and electronic properties of a 100 nm Beta CuPc film on a glass substrate. Using Grazing Incidence Wide-Angle X-ray Scattering, we observe the three dominant crystal orientations for Beta CuPc to be (1 0 1), (-1 0 5), and (-5 0 2), which have been previously misidentified as (001) and (2 0 -1) orientations by X-ray Diffraction in the literature. Each of the three crystal orientations have distinct

topography, as measured by atomic force microscopy, and optical absorption, as measured by micro UV-Vis spectroscopy, yet are electronically similar by Kelvin Probe Force microscopy. The crystal structure of Beta phase CuPc is a monoclinic herringbone, which is commonly created in thin films by either thermal annealing of Alpha CuPc at $\sim 300^\circ\text{C}$ or deposition on heated substrates. Of the several known CuPc crystal polymorphs, the Beta phase is of particular interest due to its thermodynamic stability. In the global strive to improve the performance and longevity of organic electronics, the need to understand and control the morphology in the active layer it is becoming evident.

6.3 Introduction

The promise of flexible, low cost, electronic devices composed of renewable, earth abundant, elements has led to increasing research on organic semiconductors over the last ~ 20 years. Out of the numerous organic semiconducting materials available, the planar small molecule copper phthalocyanine (CuPc) is not only one of the oldest and well-studied materials, but to date is still a common choice for organic electronic research due to its chemical stability, high molecular symmetry, facile yet precise film creation capability, and commercial availability. CuPc has been used in the fabrication of nearly all types of organic electronic devices, including diodes,¹⁰⁰ and transistors,¹⁰¹ photovoltaics,¹⁰² light emitting diodes,¹⁰³ photodetectors¹⁰⁴, rectifiers,¹⁰⁵ temperature sensors,¹⁰⁶ radiation dosimeters,¹⁰⁷ and chemical biosensors,¹⁰⁸ The growing global demand for cheap energy sources and consumer

electronics has brought organic photovoltaics (OPV's) and organic thin film transistors (OTFT's) to the forefront of organic semiconductor research.

The crystal structure and orientation of CuPc thin films has been studied by many research groups over the last few decades. The identification and control of crystal formation in organic thin films is quite valuable since the molecular orientation and order is known to have a substantial impact on the performance characteristic in organic electronic devices¹⁰⁹. The choice of substrate, substrate temperature, and film thickness are the primary factors influencing CuPc crystal structure and orientation. The most common crystal polymorphs of CuPc are the alpha herringbone,¹¹⁰ beta herringbone,¹¹¹ and the more recently identified brickstone.^{62a} In addition to there being several known crystal phases for CuPc thin films, multiple orientations of these crystals have been reported as well. Films grown on substrates below $\sim 200^\circ\text{C}$ form either the alpha herringbone or brickstone crystals. Films grown on substrates above $\sim 200^\circ\text{C}$, or annealed above $\sim 300^\circ\text{C}$ after film growth, form beta herringbone crystals. Thickness dependent morphology transition from alpha herringbone (2 0 0) to a brickstone (1 0 0) crystal structure on a ZnO(1100)^{62b} substrate and transition from brickstone (0 1 -2) to brickstone (1 1 -2) on a graphite substrate⁹⁶ have been reported. Beta CuPc has been reported to adopt several crystal orientations dependent upon the substrate and fabrication method used, including (0 1 0)¹¹², (1 0 0)¹¹³, (0 1 1)^{113b}, (-1 0 1)¹¹⁴, (3 0 2)^{113b}, (2 0 -1)¹¹⁵, (0 0 1)^{115b,c}, and (2 0 -2)^{115b} orientations. While the (0 0 1) and (2 0 -1) orientations are reported more commonly in the literature, more often than not, the

orientation of beta CuPc crystals in thin film devices are not reported, even though it known to impact their morphological, optical, and electronic properties

The active layer morphology has a significant impact on the performance of organic thin film devices.¹¹⁶ For example, CuPc TFT mobility has been reported to increase from $10^{-5} - 10^{-3} \text{ cm}^2/\text{V s}$, for deposition at room temperature or below, to $1-2 \times 10^{-2} \text{ cm}^2/\text{V s}$ by heating the substrate during deposition.¹¹⁷ Optimization of the morphology, either by altering the film fabrication procedure or by annealing the fabricated film, is a crucial step in achieving peak performance devices from a given material system. Through a deeper understanding of how to control the thin film morphology, the performance of CuPc based devices could be significantly improved.

In this paper we report the coexistence of three unique beta herringbone domain types present in a 100 nm CuPc film / glass annealed at 320°C for three hours. We characterize the morphological, optical, and electronic properties of the three observed domains using GIWAXS, AFM, KPFM, and Uv-Vis. The morphology and optical absorption properties were found to vary substantially for each of the three domain types, yet were found to be indistinguishable electronically by KPFM.

6.4 Experimental Methods

Directly prior to being loading into the OMBD deposition chamber, glass substrates were cleaned by sonication in Acetone then isopropanol, followed by Uv-Ozone cleaning, each for 15 minutes. CuPc (95%) was obtained from Sigma-Aldrich and loaded, as received,

into a boron nitride crucible. The crucible was outgassed for ~ 24 hours in high vacuum prior to film growth. CuPc thin films were grown using thermal evaporation at pressure $< 2.0 \times 10^{-6}$ torr in a high vacuum chamber with a base pressure of 10^{-8} torr. Deposition rates, monitored using a quartz crystal microbalance, between 0.3 \AA/s and 0.5 \AA/s were used during film growth. Following film growth, samples were annealed at 320° C for three hours in a dry nitrogen glove box with less than 0.1 ppm O_2 and H_2O .

AFM was carried out in AC mode in air using a commercial instrument (Asylum Research MFP-3D). Following each topography line scanned, the same line is scanned again in KPFM mode to measure the surface potential. Commercial AFM tips (Budget Sensors, Tap300E-G) had a nominal radius of ~ 10 nm, a nominal resonant frequency of ~ 300 kHz, and are composed of Silicon with a Cr/Pt conductive coating.

GIWAXS data was acquired at beamline 7.3.3 at the Advanced Light Source³² at grazing angles between 0.10° and 0.20° above the plane of the substrate. Beta phase CuPc lattice parameters used for simulation of RSM, $a = 19.407$, $b = 4.79$, $c = 14.628$, $\alpha = \gamma = 90^\circ$, $\beta = 120.933^\circ$, was identified by Brown in 1968.

Standard, bulk averaged, Ultraviolet-Visible (Uv-Vis) absorption spectroscopy was performed on films before and after annealing using a commercial instrument Cary 50 UV-Vis spectrometer. Microscopic Uv-Vis absorption measurements, with ~ 1.2 micrometer spatial resolution, was performed on individual crystal domains using a commercially available microspectrophotometer from CRAIC Technologies Inc. A visual light microscope was used to identify domains for the microscopic Uv-Vis absorption measurements.

6.5 Results

The crystal structure and orientation is determined using Grazing Incidence Wide-Angle X-ray Scattering (GIWAXS) data coupled with simulated reciprocal space maps (RSM), shown in figure 6.1. All of the scattering peaks are smeared circularly about the origin due to the rough surface of the glass substrate. None of the observed scattering peaks were centered along the q_z axis. To identify the structure and orientation of CuPc crystals responsible of the observed GIWAXS scattering peaks, RSMs of alpha herringbone, brickstone, and beta herringbone crystal structures with (H K L) orientations for all combinations of H,K,L between +/- 8 were considered. All observed scattering peaks were identified to belong to orientations of a beta herringbone crystal structure. Three different beta herringbone crystal orientations were needed to account for the observed scattering peaks. Out of all of the orientations considered, the (1 0 1), (-1 0 5), and (-5 0 2) orientations were found to be in best agreement with the observed scattering peak locations. Due to the close proximity of scattering peaks from these orientations, combined with the circular smearing of the observed scattering peaks, identification of the crystal orientations in the film cannot be determined with absolute certainty. However, the absence of a scattering peak centered along the q_z axis clearly indicates the absence of the more commonly reported (0 0 1) and (2 0 -1) orientations. Figure 6.2 illustrates the relative angle between the (1 0 1), (-1 0 5), and (-5 0 2) crystal planes, as viewed along the b-axis of the beta herringbone crystal.

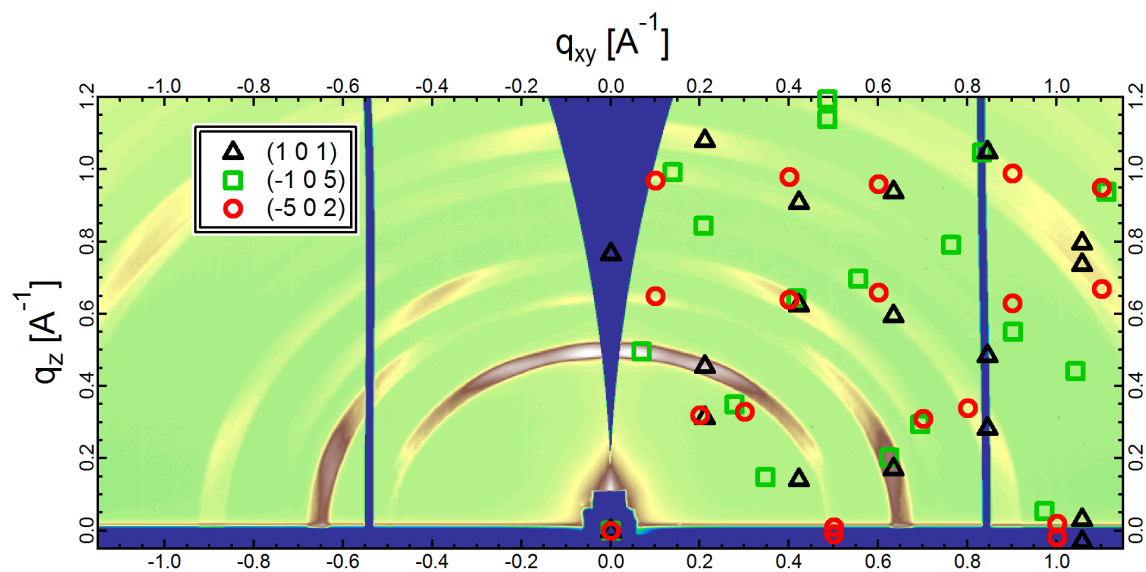


Figure 6.1 GIWAXS on Beta CuPc Thin Film. GIWAXS data, with forbidden wedge correction, on 100 nm CuPc / Glass, annealed at 320° C for 3 hours. Simulated GIWAXS scattering peak locations for (1 0 1), (-1 0 5), and (-5 0 2) orientations of beta Herringbone CuPc is overplotted.

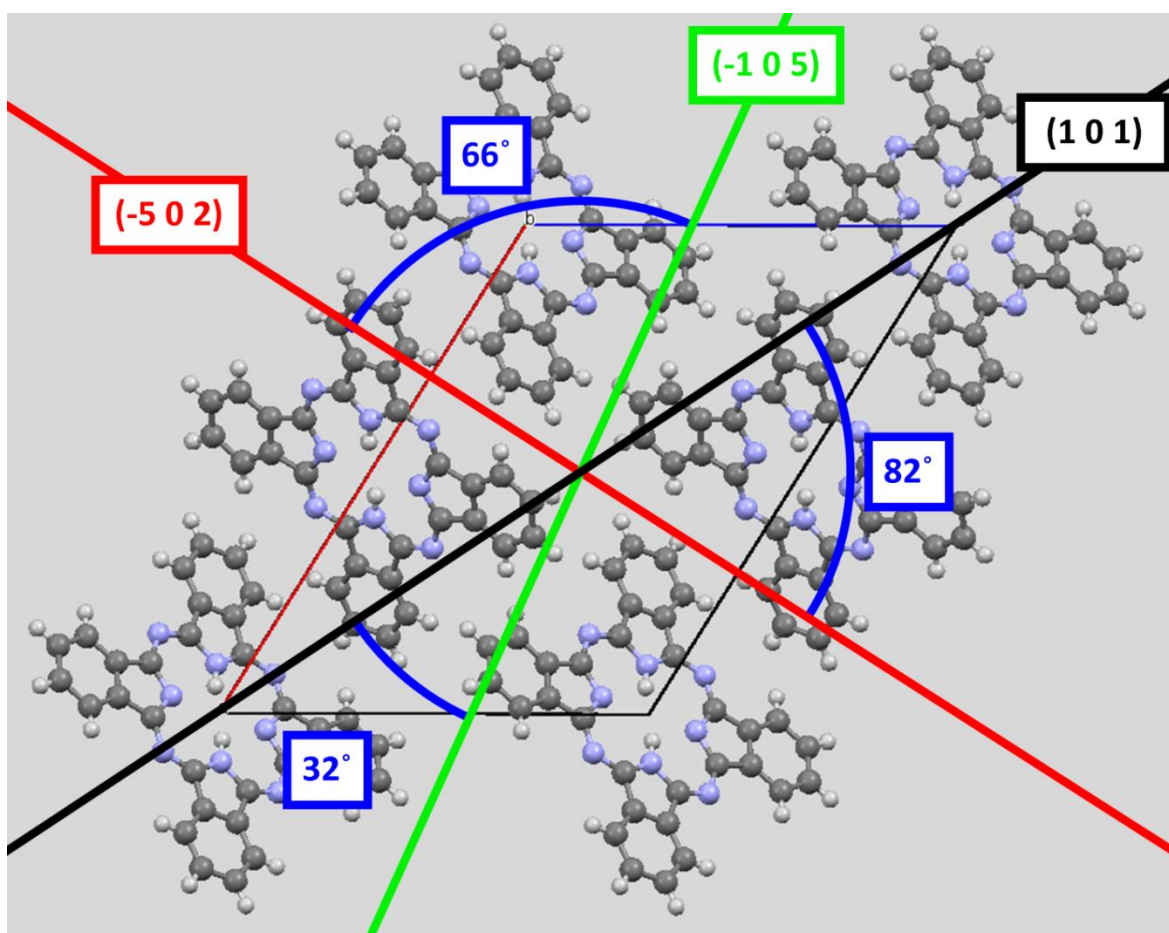


Figure 6.2 Beta CuPc Molecular Planes. Illustration of molecular arrangement of CuPc molecules in a beta herringbone crystal, as viewed along the b-axis. The parallelogram shows the unit cell, with a thin red and thin blue line showing the a-axis and c-axis of the crystal, respectively. The $(1\ 0\ 1)$, $(-1\ 0\ 5)$, and $(-5\ 0\ 2)$ crystal planes, and relative angles between these planes, are overlotted.

AFM and KPFM was performed to characterize the film morphology and surface potential. Three distinct crystal domain morphologies were observed from the topography, which, based on their observed characteristics, will be referred to as “big rough”, “small rough”, and “small flat”. The big rough crystals are larger in both surface area and height than the two smaller domains, and were observed to form ~10 micrometer wide domains

exhibiting an average RMS surface roughness of 33 ± 4 nm. The two smaller crystal domains were observed to be ~ 2 -5 micrometer wide, exhibiting average RMS surface roughness of 16.7 ± 1.4 nm for the rough domains and 8.3 ± 1.4 nm for the flat domains. The area between the two smaller crystal domain types appears to be a mixture both the small rough and small flat crystals.

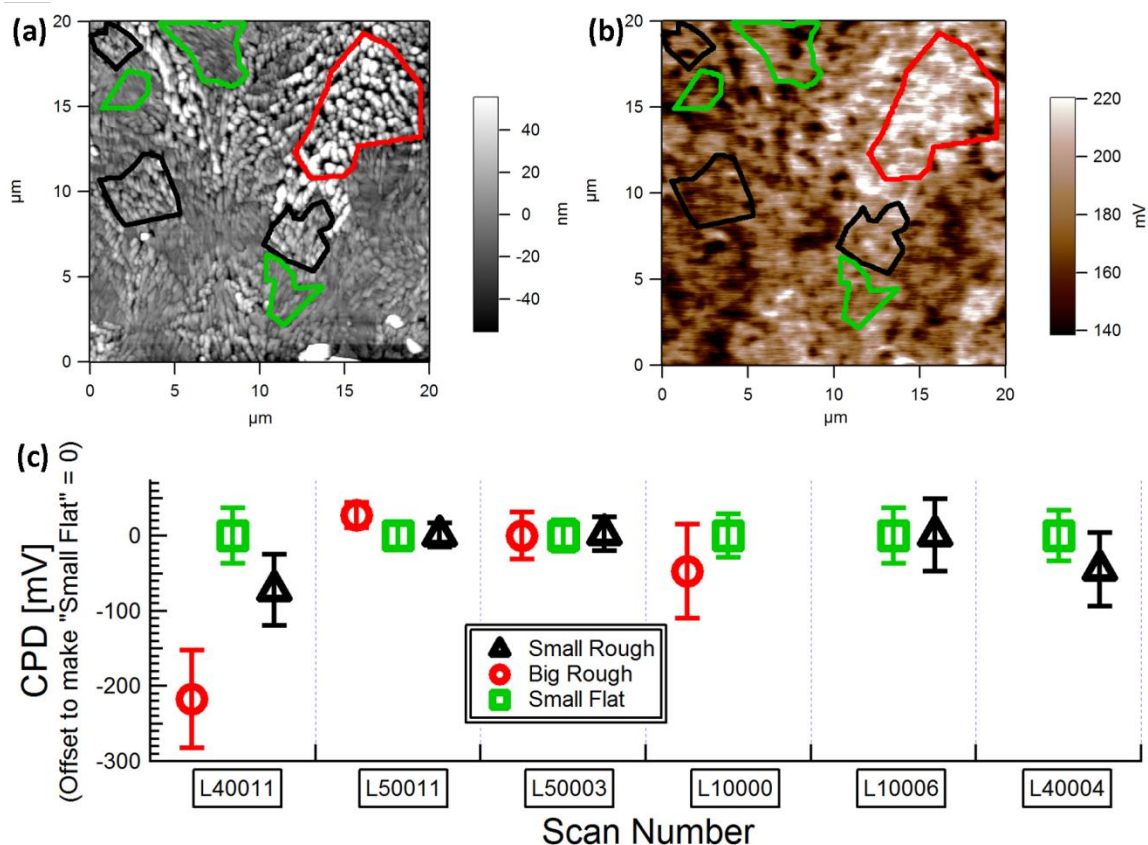


Figure 6.3 KPFM of Beta CuPc Thin Film. AFM data, shown in part (a), collected simultaneously with KPFM, shown in part (b), on 100 nm CuPc / Glass, annealed at 320°C for 3 hours. In agreement with the GIWAXS data, three distinct topographies are identified from the AFM. The average surface potential for these domains is shown in part (c), indicating no measureable difference between the three crystal orientations.

Identification of the three observed crystal domains for surface roughness and electric potential measurements was performed by manually masking the topography data based on the unique characteristics of each crystal, as shown in figure 6.2 (a) for one of the scans. Figure 6.2 (b) shows the KPFM surface potential for the topography shown in figure 6.2 (a). Using the same masks identified from the topography, the average surface potential was calculated for each of the three observed domain types. The average surface potential statistics for six scans, taken at three different macroscopic locations on the sample, are shown in figure 6.2 (c). Remarkably, there was no measureable difference in the surface potential for the three domain types.

Standard Uv-Vis absorption spectroscopy was performed on the as-grown sample and again after annealing. As expected, the Uv-Vis absorption spectra for the as-grown, alpha phase, film and the post annealed, beta phase, film agreed with previous reports in the literature¹¹⁸. While the as-grown films were featureless in the visual light microscope, the annealed film formed visible domains, as shown in figure 6.3 (a). Since the absorption profile of a material depends not only on the crystal phase, but on the orientation of the crystal as well, micro Uv-Vis was employed on individual domains. The absorption spectra was found to vary drastically depending on which domain type was measured, as shown in figure 6.3 (b). For comparison, the standard, bulk averaged, Uv-Vis absorption spectra is also plotted in figure 6.3 (b).

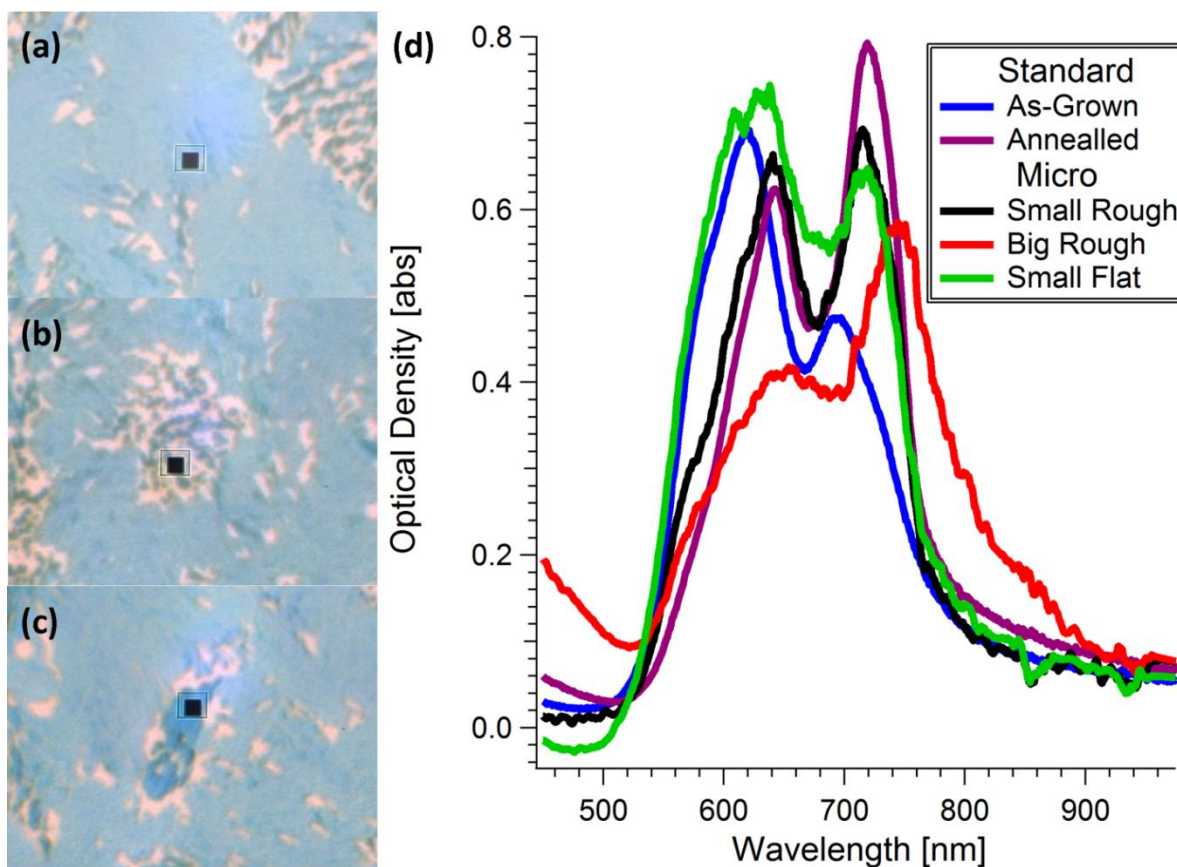


Figure 6.4 Visual Light Spectroscopy. Visual Light Microscope on 100 nm CuPc / Glass, annealed at 320° C for 3 hours, with location where micro Uv-Vis spectra was collected for (a) Small Rough, (b) Big Rough, and (c) Small Flat domains. Uv-Visible spectroscopy spectra shown in (d) on locations indicated in (a),(b), and (c), as well as standard, bulk average, spectra on the As-Grown and 320° C annealed films.

6.6 Discussion

Despite the coexistence of three different beta herringbone crystal orientations, each with significantly different absorption spectra, the average absorption spectra agreed with the literature. This indicates that the coexistence of multiple orientations may be quite common for beta CuPc films. A recent publication using inert gas flow, temperature gradient physical

vapor deposition, reported the growth of three distinct 3D Beta CuPc crystal shapes, each with unique Uv-Vis absorption, dependent on the formation temperature.¹¹⁹

Interestingly, the (1 0 1), (-1 0 5), and (-5 0 2) crystal orientations observe in our films have their b-axis aligned parallel to the substrate, yet are very different cross sections of the a-axis and c-axis of the crystal, as shown in figure 6.2. Figure 6.3 and 6.4 clearly demonstrate that each crystal orientation exhibits significantly different morphological and optical properties. The variation in morphology between each domain type, as well as the large RMS roughness, exhibited by the beta CuPc film may be detrimental for organic electronics applications. The abundance of grain boundaries in the film, in particular, would inhibit charge transport in the plane of the film, making it less suitable for TFT applications. In contrast, the large surface roughness exhibit in the “small rough” and “big rough” domains could provide better exciton dissociation if employed in a bilayer OPV due to increase interfacial area between the donor and acceptor materials.

Given that at least eight different orientations of beta herringbone CuPc have been reported in the literature, none of which were present in our films, it seems pertinent to discuss the ease of misidentification of crystal orientation by XRD. The (-1 0 5) and (-5 0 2) orientations observed in our films do not have a scattering peak on the q_z axis ($q_{xy} = 0$), meaning that these orientations would not result in a diffraction peak in standard XRD if the crystals are well ordered on a flat substrate. Orientation disorder resulting from crystals formed on a rough substrate, such as glass and ITO, results in peaks near $q_{xy} = 0$ to broaden enough to include scattering along the q_z axis. As such, scattering peaks observed in a

standard Θ - 2Θ XRD may detect peaks on the q_z axis which are actually broadened tails of scattering peaks located off of the q_z axis. For example, the [0 0 1] reflection at $q_{xy} = 0.070 \text{ \AA}^{-1}$, $q_z = 0.496 \text{ \AA}^{-1}$ of an (-1 0 5) oriented crystal could be easily mistaken for the [0 0 1] reflection of an (0 0 1) oriented crystal, which has a diffraction peak at $q_{xy} = 0 \text{ \AA}^{-1}$, $q_z = 0.50 \text{ \AA}^{-1}$. Similarly, the [2 0 1] reflection of a (-5 0 2) oriented crystal, at $q_{xy} = 0.095 \text{ \AA}^{-1}$, $q_z = 0.650 \text{ \AA}^{-1}$, could be mistaken for the [2 0 1] reflection of an (2 0 -1) oriented crystal, which has a diffraction peak at $q_{xy} = 0 \text{ \AA}^{-1}$, $q_z = 0.66 \text{ \AA}^{-1}$. Thus, the correct identification beta herringbone crystal orientation in thin films may be difficult by XRD alone, especially for films grown on rough substrates. The asymmetric charge mobility and optical absorption properties of Beta-CuPc implies that a device with uniformly oriented (1 0 1), (-1 0 5), or (-5 0 2) crystallites would each have very different the optical and electrical properties.

Since all observed crystal orientations have their b-axis, corresponding to the high charge mobility Pi-Pi stacking direction, parallel to the substrate, they are all good candidates for TFT devices. The presence of grain boundaries within a uniformly oriented film or the coexistence of multiple crystal orientations would, however, be detrimental to TFT device performance. The large RMS roughness is indicative of 3D growth of separate crystallites within a domain, which is particularly evident in the “big rough” domains, resulting in excessive grain boundaries leading to poor charge mobility. As such, we assert a film composed of only “small flat” crystals would be the best candidate for a CuPc based TFT.

6.7 Summary and Conclusions

In this paper we report on the coexistence of three distinct crystal domain types present in a 100 nm CuPc / glass film annealed at 320° C for three hours. Using GIWAXS, we determined three crystal domains to be (1 0 1), (-1 0 5), or (-5 0 2) orientations of the beta herringbone crystal structure, which to our knowledge have not been previously reported for any beta CuPc thin film. AFM and Uv-Vis absorption measurements performed on individual crystal domains reveals each of the three crystal domain types have very different morphological and optical absorption properties, yet the electrical surface potential is indistinguishable by KPFM.

Since the crystal structure and orientation is known to have a significant impact on the performance of organic electronic devices, the identification and manipulation of crystal species within the active layer of devices is very beneficial. We assert that standard Θ -2 Θ XRD is not sufficient for determination of Beta-CuPc crystal orientation. It may be beneficial to revisit previous Beta CuPc thin film device studies where standard Θ -2 Θ XRD was used to determine the crystal orientation, especially in cases where (-2 0 1) or (0 0 1) orientations were reported for films grown on rough substrates such as ITO.

Overall, the coexistence of three different crystal domain types within the beta CuPc film is detrimental for organic electronic applications. The abundance of grain boundaries between domain types, as well as within the two rougher domain types, in particular, would decrease charge mobility. By further investigation of the temperature dependence of Beta CuPc it may be possible to achieve thin films of uniformly oriented crystallites.

6.8 Acknowledgements

This work was equally supported by the U. S. Department of Energy (DE-FG02-98ER45737) and NSF CAREER award DMR-1056861 for characterization and growth, respectively. TM was partially supported by GAANN Fellowships.

CHAPTER 7

Conclusions and Outlook

In an effort to focus my research on advancing the understanding of the fundamental processes that occur within an OPV device, I have chosen to study pure and bilayer films of CuPc and C₆₀ grown by OMBD. The work reported in chapters 3,4,5, and 6 each report new morphological properties of C₆₀ and/or CuPc thin films as well as implications for use of these properties for organic electronic device applications. The films studied in these chapters are directly related to films used for OPV and/or TFT devices. The observation of dewetting of C₆₀ in chapter 3, for example, not only revealed the propensity for C₆₀ to aggregate due to low temperature annealing, but also provided a new mechanism for fabricating a BHJ morphology with controlled C₆₀ domain sizes.

The work performed in chapters 4 and 5 provides a method of creating a single crystal bilayer photovoltaic device. Rather than adopting a BHJ morphology to decrease the path length of the exciton to a D/A interface, the exciton diffusion length can be increased by providing a path to the D/A interface within a single, defect free, crystal. To my knowledge, my work in chapters 4 and 5 demonstrates, for the first time, the feasibility of creating a bilayer OPV where a single crystal acceptor domain forms co-facially on top of a single crystal donor domain. In contrast to the low temperature dewetting of C₆₀ thin films on “standing” CuPc in chapter 3, C₆₀ films grown on “flat-lying” CuPc in Chapter 5 are

thermally stable up to 150° C. This indicates a relatively stronger interaction at the D/A interface which may allow for improved exciton dissociation.

In addition to the alpha herringbone and brickstone crystal structures adopted in CuPc thin films studied in chapters 3,4 and 5, the thin film morphology of the beta herringbone crystal structure and orientation is investigated in chapter 6. Three distinct orientations were observed to coexist, each of which exhibited different morphological and optical absorption properties.

Collectively, the work in chapters 3,4, and 6 investigated the structure and control of the most common crystal structures and orientations of CuPc used in organic devices.

REFERENCES

1. *Organic Photovoltaics: Materials, Device Physics, and Manufacturing Technologies*. 2 ed.; Wiley-VCH Verlag GmbH & Co. KGaA: Weinheim, 2014.
2. Chen, C.-C.; Chang, W.-H.; Yoshimura, K.; Ohya, K.; You, J.; Gao, J.; Hong, Z.; Yang, Y., An Efficient Triple-Junction Polymer Solar Cell Having a Power Conversion Efficiency Exceeding 11%. *Advanced Materials* 2014, 26 (32), 5670-5677.
3. Liu, F.; Ferdous, S.; Schaible, E.; Hexemer, A.; Church, M.; Ding, X.; Wang, C.; Russell, T. P., Fast Printing and In Situ Morphology Observation of Organic Photovoltaics Using Slot-Die Coating. *Advanced Materials* 2015, 27 (5), 886-891.
4. Engmann, S.; Bokel, F. A.; Herzing, A. A.; Ro, H. W.; Girotto, C.; Caputo, B.; Hoven, C. V.; Schaible, E.; Hexemer, A.; DeLongchamp, D. M.; Richter, L. J., Real-time X-ray scattering studies of film evolution in high performing small-molecule-fullerene organic solar cells. *Journal of Materials Chemistry A* 2015, 3 (16), 8764-8771.
5. Rand, B. P.; Richter, H., *Organic Solar Cells Fundamentals, Devices, and Upscaling*. Pan Stanford: Florida, 2014.
6. Gregg, B. A.; Hanna, M. C., Comparing organic to inorganic photovoltaic cells: Theory, experiment, and simulation. *Journal of Applied Physics* 2003, 93 (6), 3605-3614.
7. Bergemann, K. J.; Forrest, S. R., Measurement of exciton diffusion lengths in optically thin organic films. *Applied Physics Letters* 2011, 99 (24).
8. Lunt, R. R.; Benziger, J. B.; Forrest, S. R., Relationship between Crystalline Order and Exciton Diffusion Length in Molecular Organic Semiconductors. *Advanced Materials* 2010, 22 (11), 1233-+.

9. Lunt, R. R.; Giebink, N. C.; Belak, A. A.; Benziger, J. B.; Forrest, S. R., Exciton diffusion lengths of organic semiconductor thin films measured by spectrally resolved photoluminescence quenching. *Journal of Applied Physics* 2009, *105* (5).
10. Deibel, C.; Dyakonov, V., Polymer-fullerene bulk heterojunction solar cells. *Reports on Progress in Physics* 2010, *73* (9).

11. (a) Peumans, P.; Uchida, S.; Forrest, S. R., Efficient bulk heterojunction photovoltaic cells using small-molecular-weight organic thin films. *Nature* 2003, *425* (6954), 158-162; (b) Yang, F.; Shtein, M.; Forrest, S. R., Controlled growth of a molecular bulk heterojunction photovoltaic cell. *Nature Materials* 2005, *4* (1), 37-41.

12. Tang, C. W., 2-LAYER ORGANIC PHOTOVOLTAIC CELL. *Applied Physics Letters* 1986, *48* (2), 183-185.

13. Yu, G.; Gao, J.; Hummelen, J. C.; Wudl, F.; Heeger, A. J., POLYMER PHOTOVOLTAIC CELLS - ENHANCED EFFICIENCIES VIA A NETWORK OF INTERNAL DONOR-ACCEPTOR HETEROJUNCTIONS. *Science* 1995, *270* (5243), 1789-1791.

14. Peumans, P.; Forrest, S. R., Very-high-efficiency double-heterostructure copper phthalocyanine/C-60 photovoltaic cells. *Applied Physics Letters* 2001, *79* (1), 126-128.

15. Aernouts, T.; Geens, W.; Poortmans, J.; Heremans, P.; Borghs, S.; Mertens, R., Extraction of bulk and contact components of the series resistance in organic bulk donor-acceptor-heterojunctions. *Thin Solid Films* 2002, *403*, 297-301.

16. Padinger, F.; Rittberger, R. S.; Sariciftci, N. S., Effects of postproduction treatment on plastic solar cells. *Advanced Functional Materials* 2003, *13* (1), 85-88.

17. Ma, W. L.; Yang, C. Y.; Gong, X.; Lee, K.; Heeger, A. J., Thermally stable, efficient polymer solar cells with nanoscale control of the interpenetrating network morphology. *Advanced Functional Materials* 2005, *15* (10), 1617-1622.

18. Xue, J. G.; Rand, B. P.; Uchida, S.; Forrest, S. R., A hybrid planar-mixed molecular heterojunction photovoltaic cell. *Advanced Materials* 2005, 17 (1), 66-+.

19. Chen, Y.-H.; Lin, L.-Y.; Lu, C.-W.; Lin, F.; Huang, Z.-Y.; Lin, H.-W.; Wang, P.-H.; Liu, Y.-H.; Wong, K.-T.; Wen, J.; Miller, D. J.; Darling, S. B., Vacuum-Deposited Small-Molecule Organic Solar Cells with High Power Conversion Efficiencies by Judicious Molecular Design and Device Optimization. *Journal of the American Chemical Society* 2012, 134 (33), 13616-13623.

20. Liu, Y. S.; Chen, C. C.; Hong, Z. R.; Gao, J.; Yang, Y.; Zhou, H. P.; Dou, L. T.; Li, G., Solution-processed small-molecule solar cells: breaking the 10% power conversion efficiency. *Scientific Reports* 2013, 3.

21. Kan, B.; Li, M. M.; Zhang, Q.; Liu, F.; Wan, X. J.; Wang, Y. C.; Ni, W.; Long, G. K.; Yang, X.; Feng, H. R.; Zuo, Y.; Zhang, M. T.; Huang, F.; Cao, Y.; Russell, T. P.; Chen, Y. S., A Series of Simple Oligomer-like Small Molecules Based on Oligothiophenes for Solution-Processed Solar Cells with High Efficiency. *Journal of the American Chemical Society* 2015, 137 (11), 3886-3893.
22. Rand, B. P.; Burk, D. P.; Forrest, S. R., Offset energies at organic semiconductor heterojunctions and their influence on the open-circuit voltage of thin-film solar cells. *Physical Review B* 2007, 75 (11).

23. Mukherjee, S.; Proctor, C. M.; Bazan, G. C.; Nguyen, T.-Q.; Ade, H., Significance of Average Domain Purity and Mixed Domains on the Photovoltaic Performance of High-Efficiency Solution-Processed Small-Molecule BHJ Solar Cells. *Advanced Energy Materials* 2015, n/a-n/a.

24. Groves, C., Developing understanding of organic photovoltaic devices: kinetic Monte Carlo models of geminate and non-geminate recombination, charge transport and charge extraction. *Energy & Environmental Science* 2013, 6 (11), 3202-3217.

25. Love, J. A.; Proctor, C. M.; Liu, J.; Takacs, C. J.; Sharenko, A.; van der Poll, T. S.; Heeger, A. J.; Bazan, G. C.; Nguyen, T.-Q., Film Morphology of High Efficiency Solution-Processed Small-Molecule Solar Cells. *Advanced Functional Materials* 2013, 23 (40), 5019-5026.

26. Takacs, C. J.; Collins, S. D.; Love, J. A.; Mikhailovsky, A. A.; Wynands, D.; Bazan, G. C.; Thuc-Quyen, N.; Heeger, A. J., Mapping Orientational Order in a Bulk Heterojunction Solar Cell with Polarization-Dependent Photoconductive Atomic Force Microscopy. *ACS Nano* 2014, 8 (8), 8141-8151.
27. Yin, W.; Dadmun, M., A New Model for the Morphology of P3HT/PCBM Organic Photovoltaics from Small-Angle Neutron Scattering: Rivers and Streams. *ACS Nano* 2011, 5 (6), 4756-4768.
28. Rivnay, J.; Mannsfeld, S. C.; Miller, C. E.; Salleo, A.; Toney, M. F., Quantitative determination of organic semiconductor microstructure from the molecular to device scale. *Chem Rev* 2012, 112 (10), 5488-519.
29. (a) Carpenter, J. H.; Hunt, A.; Ade, H., Characterizing morphology in organic systems with resonant soft X-ray scattering. *Journal of Electron Spectroscopy and Related Phenomena* 2015; (b) Collins, B. A.; Cochran, J. E.; Yan, H.; Gann, E.; Hub, C.; Fink, R.; Wang, C.; Schuettfort, T.; McNeill, C. R.; Chabynyc, M. L.; Ade, H., Polarized X-ray scattering reveals non-crystalline orientational ordering in organic films. *Nat Mater* 2012, 11 (6), 536-543.
30. Wang, J. Scanning Probe Microscopy of Intrinsic and Extrinsic Disorder in Organic Semiconductors. Ph.D, North Carolina State University, Raleigh, 2014.
31. Jones, J. E., On the determination of molecular fields - II From the equation of state of a gas. *Proceedings of the Royal Society of London Series a-Containing Papers of a Mathematical and Physical Character* 1924, 106 (738), 463-477.
32. Hexemer, A.; Bras, W.; Glossinger, J.; Schaible, E.; Gann, E.; Kirian, R.; MacDowell, A.; Church, M.; Rude, B.; Padmore, H., A SAXS/WAXS/GISAXS Beamline with Multilayer Monochromator. In *Xiv International Conference on Small-Angle Scattering*, Ungar, G., Ed. 2010; Vol. 247.
33. Riede, M.; Mueller, T.; Tress, W.; Schueppel, R.; Leo, K., Small-molecule solar cells - status and perspectives. *Nanotechnology* 2008, 19 (42), 424001.

34. Deibel, C.; Dyakonov, V., Polymer-fullerene bulk heterojunction solar cells. *Reports on Progress in Physics* 2010, 73 (9), 096401.
35. Xue, J. G.; Uchida, S.; Rand, B. P.; Forrest, S. R., Asymmetric tandem organic photovoltaic cells with hybrid planar-mixed molecular heterojunctions. *Applied Physics Letters* 2004, 85 (23), 5757-5759.
36. (a) Verlaak, S.; Beljonne, D.; Cheyins, D.; Rolin, C.; Linares, M.; Castet, F.; Cornil, J.; Heremans, P., Electronic Structure and Geminate Pair Energetics at Organic–Organic Interfaces: The Case of Pentacene/C60 Heterojunctions. *Adv. Funct. Mater.* 2009, 19 (23), 3809-3814; (b) Rand, B. P.; Cheyins, D.; Vasseur, K.; Giebink, N. C.; Mothy, S.; Yi, Y.; Coropceanu, V.; Beljonne, D.; Cornil, J.; Brédas, J.-L.; Genoe, J., The Impact of Molecular Orientation on the Photovoltaic Properties of a Phthalocyanine/Fullerene Heterojunction. *Adv. Funct. Mater.* 2012, 22 (14), 2987-2995.
37. Pandey, R.; Holmes, R. J., Graded Donor-Acceptor Heterojunctions for Efficient Organic Photovoltaic Cells. *Advanced Materials* 2010, 22 (46), 5301-5305.
38. Opitz, A.; Wagner, J.; Brutting, W.; Hinderhofer, A.; Schreiber, F., Molecular semiconductor blends: Microstructure, charge carrier transport, and application in photovoltaic cells. *Physica Status Solidi a-Applications and Materials Science* 2009, 206 (12), 2683-2694.
39. Chen, G.; Sasabe, H.; Wang, Z. Q.; Wang, X. F.; Hong, Z. R.; Yang, Y.; Kido, J. J., Co-Evaporated Bulk Heterojunction Solar Cells with > 6.0% Efficiency. *Advanced Materials* 2012, 24 (20), 2768.
40. (a) Thomas, M.; Worfolk, B. J.; Rider, D. A.; Taschuk, M. T.; Buriak, J. M.; Brett, M. J., C60 Fullerene Nanocolumns–Polythiophene Heterojunctions for Inverted Organic Photovoltaic Cells. *ACS Applied Materials & Interfaces* 2011, 3 (6), 1887; (b) Yang, F.; Forrest, S. R., Photocurrent Generation in Nanostructured Organic Solar Cells. *ACS Nano* 2008, 2 (5), 1022.

41. Wei, H. X.; Li, J.; Xu, Z. Q.; Cai, Y.; Tang, J. X.; Li, Y. Q., Thermal annealing-induced vertical phase separation of copper phthalocyanine: Fullerene bulk heterojunction in organic photovoltaic cells. *Applied Physics Letters* 2010, 97 (8), 083302.
42. (a) Fitzner, R.; Mena-Osteritz, E.; Mishra, A.; Schulz, G.; Reinold, E.; Weil, M.; Köhner, C.; Ziehlke, H.; Elschner, C.; Leo, K.; Riede, M.; Pfeiffer, M.; Urich, C.; Bäuerle, P., Correlation of π -Conjugated Oligomer Structure with Film Morphology and Organic Solar Cell Performance. *Journal of the American Chemical Society* 2012, 134 (27), 11064; (b) Schultes, S. M.; Sullivan, P.; Heutz, S.; Sanderson, B. M.; Jones, T. S., The role of molecular architecture and layer composition on the properties and performance of CuPc-C60 photovoltaic devices. *Materials Science and Engineering: C* 2005, 25, 858; (c) Suemori, K.; Miyata, T.; Hiramoto, M.; Yokoyama, M., Enhanced Photovoltaic Performance in Fullerene:Phthalocyanine Codeposited Films Deposited on Heated Substrate. *Japanese Journal of Applied Physics* 2004, 43, L1014.
43. Conrad, B. R.; Tosado, J.; Dutton, G.; Dougherty, D. B.; Jin, W.; Bonnen, T.; Schuldenfrei, A.; Cullen, W. G.; Williams, E. D.; Reutt-Robey, J. E.; Robey, S. W., C-60 cluster formation at interfaces with pentacene thin-film phases. *Applied Physics Letters* 2009, 95 (21), 213302.
44. Miller, C. W.; Sharoni, A.; Liu, G.; Colesniuc, C. N.; Fruhberger, B.; Schuller, I. K., Quantitative structural analysis of organic thin films: An x-ray diffraction study. *Physical Review B* 2005, 72 (10), 104113.
45. De Francesco, R.; Stener, M.; Fronzoni, G., Theoretical Study of Near-Edge X-ray Absorption Fine Structure Spectra of Metal Phthalocyanines at C and N K-Edges. *Journal of Physical Chemistry A* 2012, 116 (11), 2885.
46. (a) Chakraverty, B. K., GRAIN SIZE DISTRIBUTION IN THIN FILMS .1. CONSERVATIVE SYSTEMS. *Journal of Physics and Chemistry of Solids* 1967, 28 (12), 2401; (b) Lifshitz, I. M.; Slyozov, V. V., THE KINETICS OF PRECIPITATION FROM SUPERSATURATED SOLID SOLUTIONS. *Journal of Physics and Chemistry of Solids* 1961, 19 (1-2), 35.

47. Kowarik, S.; Gerlach, A.; Sellner, S.; Cavalcanti, L.; Schreiber, F., Dewetting of an Organic Semiconductor Thin Film Observed in Real-time. *Advanced Engineering Materials* 2009, *11* (4), 291-294.
48. Cantrell, R. A.; Clancy, P., A New Kinetic Monte Carlo Algorithm for Heteroepitactical Growth: Case Study of C-60 Growth on Pentacene. *Journal of Chemical Theory and Computation* 2012, *8* (3), 1048.
49. Zimmerman, J. D.; Xiao, X.; Renshaw, C. K.; Wang, S. Y.; Diev, V. V.; Thompson, M. E.; Forrest, S. R., Independent Control of Bulk and Interfacial Morphologies of Small Molecular Weight Organic Heterojunction Solar Cells. *Nano Letters* 2012, *12* (8), 4366.
50. Weickert, J.; Dunbar, R. B.; Hesse, H. C.; Wiedemann, W.; Schmidt-Mende, L., Nanostructured Organic and Hybrid Solar Cells. *Advanced Materials* 2011, *23* (16), 1810.
51. Xue, J.; Rand, B. P.; Uchida, S.; Forrest, S. R., A Hybrid Planar–Mixed Molecular Heterojunction Photovoltaic Cell. *Advanced Materials* 2005, *17* (1), 66-71.
52. Chen, L.; Tang, Y.; Fan, X.; Zhang, C.; Chu, Z.; Wang, D.; Zou, D., Improvement of the efficiency of CuPc/C60-based photovoltaic cells using a multistep structure. *Organic Electronics* 2009, *10* (4), 724-728.
53. Hesse, H. C.; Weickert, J.; Al-Hussein, M.; Dossel, L.; Feng, X.; Mullen, K.; Schmidt-Mende, L., Discotic materials for organic solar cells: Effects of chemical structure on assembly and performance. *Solar Energy Materials and Solar Cells* 2010, *94* (3), 560-567.
54. Collins, B. A.; Gann, E.; Guignard, L.; He, X.; McNeill, C. R.; Ade, H., Molecular Miscibility of Polymer-Fullerene Blends. *The Journal of Physical Chemistry Letters* 2010, *1* (21), 3160.
55. Chen, L.-M.; Hong, Z.; Li, G.; Yang, Y., Recent Progress in Polymer Solar Cells: Manipulation of Polymer:Fullerene Morphology and the Formation of Efficient Inverted Polymer Solar Cells. *Advanced Materials* 2009, *21* (14-15), 1434.

56. (a) Gao, J.; Asadi, K.; Xu, J. B.; An, J., Controlling of the surface energy of the gate dielectric in organic field-effect transistors by polymer blend. *Applied Physics Letters* 2009, 94 (9); (b) Tajima, Y.; Matsuura, T.; Numata, Y.; Yamazaki, D.; Kawamura, H.; Osedo, H., Surface free energy and wettability determination of various fullerene derivative films on amorphous carbon wafer. *Japanese Journal of Applied Physics* 2008, 47 (7), 5730-5733; (c) Gomez De Arco, L.; Zhang, Y.; Schlenker, C. W.; Ryu, K.; Thompson, M. E.; Zhou, C., Continuous, Highly Flexible, and Transparent Graphene Films by Chemical Vapor Deposition for Organic Photovoltaics. *ACS Nano* 2010, 4 (5), 2865-2873.
57. (a) Minami, T., Transparent conducting oxide semiconductors for transparent electrodes. *Semiconductor Science and Technology* 2005, 20 (4), S35-S44; (b) Bernede, J. C.; Berredjem, Y.; Cattin, L.; Morsli, M., Improvement of organic solar cell performances using a zinc oxide anode coated by an ultrathin metallic layer. *Applied Physics Letters* 2008, 92 (8); (c) Izaki, M.; Omi, T., Transparent zinc oxide films prepared by electrochemical reaction. *Applied Physics Letters* 1996, 68 (17), 2439-2440.
58. (a) Hau, S. K.; Yip, H. L.; Zou, J. Y.; Jen, A. K. Y., Indium tin oxide-free semi-transparent inverted polymer solar cells using conducting polymer as both bottom and top electrodes. *Organic Electronics* 2009, 10 (7), 1401-1407; (b) Zhou, Y. H.; Zhang, F. L.; Tvingstedt, K.; Barrau, S.; Li, F. H.; Tian, W. J.; Inganäs, O., Investigation on polymer anode design for flexible polymer solar cells. *Applied Physics Letters* 2008, 92 (23); (c) Ahlswede, E.; Muhleisen, W.; Wahi, M.; Hanisch, J.; Powalla, M., Highly efficient organic solar cells with printable low-cost transparent contacts. *Applied Physics Letters* 2008, 92 (14); (d) Na, S. I.; Kim, S. S.; Jo, J.; Kim, D. Y., Efficient and Flexible ITO-Free Organic Solar Cells Using Highly Conductive Polymer Anodes. *Advanced Materials* 2008, 20 (21), 4061-+.
59. Wu, J. B.; Becerril, H. A.; Bao, Z. N.; Liu, Z. F.; Chen, Y. S.; Peumans, P., Organic solar cells with solution-processed graphene transparent electrodes. *Applied Physics Letters* 2008, 92 (26).
60. Xiao, K.; Deng, W.; Keum, J. K.; Yoon, M.; Vlassiuk, I. V.; Clark, K. W.; Li, A. P.; Kravchenko, I.; Gu, G.; Payzant, E. A.; Sumpter, B. G.; Smith, S. C.; Browning, J. F.; Geohegan, D. B., Surface-Induced Orientation Control of CuPc Molecules for the Epitaxial Growth of Highly Ordered Organic Crystals on Graphene. *Journal of the American Chemical Society* 2013, 135 (9), 3680-3687.

61. Mativetsky, J. M.; Wang, H.; Lee, S. S.; Whittaker-Brooks, L.; Loo, Y.-L., Face-on stacking and enhanced out-of-plane hole mobility in graphene-templated copper phthalocyanine. *Chemical Communications* 2014.
62. (a) Hoshino, A.; Takenaka, Y.; Miyaji, H., Redetermination of the crystal structure of alpha-copper phthalocyanine grown on KCl. *Acta Crystallographica Section B-Structural Science* 2003, *59*, 393-403; (b) Cruickshank, A. C.; Dotzler, C. J.; Din, S.; Heutz, S.; Toney, M. F.; Ryan, M. P., The Crystalline Structure of Copper Phthalocyanine Films on ZnO(1(1)over-bar00). *Journal of the American Chemical Society* 2012, *134* (35), 14302-14305.
63. Kinder, L.; Kanicki, J.; Petroff, P., Structural ordering and enhanced carrier mobility in organic polymer thin film transistors. *Synthetic Metals* 2004, *146* (2), 181-185.
64. Chen, W.; Qi, D. C.; Huang, Y. L.; Huang, H.; Wang, Y. Z.; Chen, S.; Gao, X. Y.; Wee, A. T. S., Molecular Orientation Dependent Energy Level Alignment at Organic-Organic Heterojunction Interfaces. *Journal of Physical Chemistry C* 2009, *113* (29), 12832-12839.
65. Yook, K. S.; Chin, B. D.; Lee, J. Y.; Lassiter, B. E.; Forrest, S. R., Vertical orientation of copper phthalocyanine in organic solar cells using a small molecular weight organic templating layer. *Applied Physics Letters* 2011, *99* (4).
66. Peisert, H.; Schwieger, T.; Auerhammer, J. M.; Knupfer, M.; Golden, M. S.; Fink, J.; Bressler, P. R.; Mast, M., Order on disorder: Copper phthalocyanine thin films on technical substrates. *Journal of Applied Physics* 2001, *90* (1), 466-469.
67. Debe, M. K.; Poirier, R. J.; Kam, K. K., ORGANIC-THIN-FILM-INDUCED MOLECULAR EPITAXY FROM THE VAPOR-PHASE. *Thin Solid Films* 1991, *197* (1-2), 335-347.
68. Ashida, M., ORIENTATION OVERGROWTH OF METAL-PHTHALOCYANINES ON SURFACE OF SINGLE CRYSTALS .2. VACUUM-CONDENSED FILMS OF COPPER-PHTHALOCYANINE ON ALKALI HALIDES. *Bulletin of the Chemical Society of Japan* 1966, *39* (12), 2632-&.

69. Rand, B. P.; Cheyins, D.; Vasseur, K.; Giebink, N. C.; Mothy, S.; Yi, Y. P.; Coropceanu, V.; Beljonne, D.; Cornil, J.; Bredas, J. L.; Genoe, J., The Impact of Molecular Orientation on the Photovoltaic Properties of a Phthalocyanine/Fullerene Heterojunction. *Advanced Functional Materials* 2012, 22 (14), 2987-2995.
70. Sandin, A.; Rowe, J. E.; Dougherty, D. B., Improved graphene growth in UHV: Pit-free surfaces by selective Si etching of SiC(0001)-Si with atomic hydrogen. *Surface Science* 2013, 611, 25-31.
71. Wang, S. D.; Dong, X.; Lee, C. S.; Lee, S. T., Orderly growth of copper phthalocyanine on highly oriented pyrolytic graphite (HOPG) at high substrate temperatures. *Journal of Physical Chemistry B* 2004, 108 (5), 1529-1532.
72. Gopakumar, T. G.; Lackinger, M.; Hackert, M.; Müller, F.; Hietschold, M., Adsorption of Palladium Phthalocyanine on Graphite: STM and LEED Study. *The Journal of Physical Chemistry B* 2004, 108 (23), 7839-7843.
73. Sandin, A. Tunneling Spectroscopy Studies of Epitaxial Graphene and its Interfaces. North Carolina State University, 2012.
74. Tersoff, J.; Tromp, R. M., Shape transition in growth of strained islands: Spontaneous formation of quantum wires. *Physical Review Letters* 1993, 70 (18), 2782-2785.
75. Jesson, D. E.; Chen, G.; Chen, K. M.; Pennycook, S. J., Self-Limiting Growth of Strained Faceted Islands. *Physical Review Letters* 1998, 80 (23), 5156-5159.
76. Ren, J.; Meng, S.; Wang, Y.-L.; Ma, X.-C.; Xue, Q.-K.; Kaxiras, E., Properties of copper (fluoro-)phthalocyanine layers deposited on epitaxial graphene. *The Journal of Chemical Physics* 2011, 134 (19), -.
77. Dou, W. D.; Yang, Q. D.; Lee, C. S., Influences of Ion-Induced Defects on Growth of Copper-Phthalocyanine Film on Graphene Substrates. *Journal of Physical Chemistry C* 2012, 116 (36), 19278-19284.

78. Breuer, T.; Salzmann, I.; Gotzen, J.; Oehzelt, M.; Morherr, A.; Koch, N.; Witte, G., Interrelation between Substrate Roughness and Thin-Film Structure of Functionalized Acenes on Graphite. *Crystal Growth & Design* 2011, *11* (11), 4996-5001.
79. Bae, S.; Kim, H.; Lee, Y.; Xu, X. F.; Park, J. S.; Zheng, Y.; Balakrishnan, J.; Lei, T.; Kim, H. R.; Song, Y. I.; Kim, Y. J.; Kim, K. S.; Ozyilmaz, B.; Ahn, J. H.; Hong, B. H.; Iijima, S., Roll-to-roll production of 30-inch graphene films for transparent electrodes. *Nature Nanotechnology* 2010, *5* (8), 574-578.
80. Mao, H. Y.; Lu, Y. H.; Lin, J. D.; Zhong, S.; Wee, A. T. S.; Chen, W., Manipulating the electronic and chemical properties of graphene via molecular functionalization. *Progress in Surface Science* 2013, *88* (2), 132-159.
81. Wu, J.; Becerril, H. A.; Bao, Z.; Liu, Z.; Chen, Y.; Peumans, P., Organic solar cells with solution-processed graphene transparent electrodes. *Applied Physics Letters* 2008, *92* (26), -.
82. de Heer, W. A., Epitaxial graphene: A new electronic material for the 21st century. *Mrs Bulletin* 2011, *36* (8), 632-639.
83. Smilgies, D. M.; Blasini, D. R., Indexation scheme for oriented molecular thin films studied with grazing-incidence reciprocal-space mapping. *Journal of Applied Crystallography* 2007, *40*, 716-718.
84. Peumans, P.; Yakimov, A.; Forrest, S. R., Small molecular weight organic thin-film photodetectors and solar cells. *Journal of Applied Physics* 2003, *93* (7), 3693-3723.
85. Chen, Y. H.; Lin, L. Y.; Lu, C. W.; Lin, F.; Huang, Z. Y.; Lin, H. W.; Wang, P. H.; Liu, Y. H.; Wong, K. T.; Wen, J. G.; Miller, D. J.; Darling, S. B., Vacuum-Deposited Small-Molecule Organic Solar Cells with High Power Conversion Efficiencies by Judicious Molecular Design and Device Optimization. *Journal of the American Chemical Society* 2012, *134* (33), 13616-13623.

86. Che, X. Z.; Xiao, X.; Zimmerman, J. D.; Fan, D. J.; Forrest, S. R., High-Efficiency, Vacuum-Deposited, Small-Molecule Organic Tandem and Triple-Junction Photovoltaic Cells. *Advanced Energy Materials* 2014, 4 (18).
87. (a) Riede, M.; Mueller, T.; Tress, W.; Schueppel, R.; Leo, K., Small-molecule solar cells - status and perspectives. *Nanotechnology* 2008, 19 (42); (b) Schueppel, R.; Timmreck, R.; Allinger, N.; Mueller, T.; Furno, M.; Urich, C.; Leo, K.; Riede, M., Controlled current matching in small molecule organic tandem solar cells using doped spacer layers. *Journal of Applied Physics* 2010, 107 (4).
88. (a) Sanchez-Diaz, A.; Burtone, L.; Riede, M.; Palomares, E., Measurements of Efficiency Losses in Blend and Bilayer-Type Zinc Phthalocyanine/C-60 High-Vacuum-Processed Organic Solar Cells. *Journal of Physical Chemistry C* 2012, 116 (31), 16384-16390; (b) Credginton, D.; Liu, S. W.; Nelson, J.; Durrant, J. R., In Situ Measurement of Energy Level Shifts and Recombination Rates in Subphthalocyanine/C-60 Bilayer Solar Cells. *Journal of Physical Chemistry C* 2014, 118 (40), 22858-22864.
89. Kowarik, S.; Gerlach, A.; Schreiber, F., Organic molecular beam deposition: fundamentals, growth dynamics, and in situ studies. *Journal of Physics-Condensed Matter* 2008, 20 (18), 184005.
90. (a) Li, X.; Chen, Y.; Sang, J.; Mi, B. X.; Mu, D. H.; Li, Z. G.; Zhang, H.; Gao, Z. Q.; Huang, W., CuPc/C60 bulk heterojunction photovoltaic cells with evidence of phase segregation. *Organic Electronics* 2013, 14 (1), 250-254; (b) Piersimoni, F.; Degutis, G.; Bertho, S.; Vandewal, K.; Spoltore, D.; Vangerven, T.; Drijkoningen, J.; Van Bael, M. K.; Hardy, A.; D'Haen, J.; Maes, W.; Vanderzande, D.; Nesladek, M.; Manca, J., Influence of fullerene photodimerization on the PCBM crystallization in polymer: Fullerene bulk heterojunctions under thermal stress. *Journal of Polymer Science Part B-Polymer Physics* 2013, 51 (16), 1209-1214.
91. Hinderhofer, A.; Schreiber, F., Organic-Organic Heterostructures: Concepts and Applications. *Chemphyschem* 2012, 13 (3), 628-643.
92. McAfee, T.; Gann, E.; Ade, H.; Dougherty, D. B., Thermally Induced Dewetting in Ultrathin C-60 Films on Copper Phthalocyanine. *Journal of Physical Chemistry C* 2013, 117 (49), 26007-26012.

93. (a) Jailaubekov, A. E.; Willard, A. P.; Tritsch, J. R.; Chan, W. L.; Sai, N.; Gearba, R.; Kaake, L. G.; Williams, K. J.; Leung, K.; Rosky, P. J.; Zhu, X. Y., Hot charge-transfer excitons set the time limit for charge separation at donor/acceptor interfaces in organic photovoltaics. *Nature Materials* 2013, 12 (1), 66-73; (b) Ayzner, A. L.; Nordlund, D.; Kim, D. H.; Bao, Z. N.; Toney, M. F., Ultrafast Electron Transfer at Organic Semiconductor Interfaces: Importance of Molecular Orientation. *Journal of Physical Chemistry Letters* 2015, 6 (1), 6-12.
94. Zimmerman, J. D.; Lassiter, B. E.; Xiao, X.; Sun, K.; Dolocan, A.; Gearba, R.; Vanden Bout, D. A.; Stevenson, K. J.; Wickramasinghe, P.; Thompson, M. E.; Forrest, S. R., Control of Interface Order by Inverse Quasi-Epitaxial Growth of Squaraine/Fullerene Thin Film Photovoltaics. *Acs Nano* 2013, 7 (10), 9268-9275.
95. Fu, Y. T.; Risko, C.; Bredas, J. L., Intermixing at the Pentacene-Fullerene Bilayer Interface: A Molecular Dynamics Study. *Advanced Materials* 2013, 25 (6), 878-882.
96. McAfee, T.; Gann, E.; Guan, T. S.; Stuart, S. C.; Rowe, J.; Dougherty, D. B.; Ade, H., Toward Single-Crystal Hybrid-Carbon Electronics: Impact of Graphene Substrate Defect Density on Copper Phthalocyanine Film Growth. *Crystal Growth & Design* 2014, 14 (9), 4394-4401.
97. Zhang, L. S.; Roy, S. S.; Hamers, R. J.; Arnold, M. S.; Andrew, T. L., Molecular Orientation-Dependent Interfacial Energetics and Built-in Voltage Tuned by a Template Graphene Monolayer. *Journal of Physical Chemistry C* 2015, 119 (1), 45-54.
98. Distler, A.; Sauermann, T.; Egelhaaf, H. J.; Rodman, S.; Waller, D.; Cheon, K. S.; Lee, M.; Drolet, N.; Guldi, D. M., The Effect of PCBM Dimerization on the Performance of Bulk Heterojunction Solar Cells (vol 4, 1300693, 2014). *Advanced Energy Materials* 2014, 4 (4), 1400171.
99. Conings, B.; Bertho, S.; Vandewal, K.; Senes, A.; D'Haen, J.; Manca, J.; Janssen, R. A. J., Modeling the temperature induced degradation kinetics of the short circuit current in organic bulk heterojunction solar cells. *Applied Physics Letters* 2010, 96 (16), 163301.

100. Gould, R. D.; Hassan, A. K., HIGH-FIELD ELECTRONIC CONDUCTION PROCESSES IN COPPER PHTHALOCYANINE THIN-FILMS USING LEAD AND GOLD ELECTRODE COMBINATIONS. *Thin Solid Films* 1990, *193* (1-2), 895-904.
101. Yuan, J. F.; Zhang, J.; Wang, J.; Yan, X. J.; Yan, D. H.; Xu, W., Bottom-contact organic field-effect transistors having low-dielectric layer under source and drain electrodes. *Applied Physics Letters* 2003, *82* (22), 3967-3969.
102. Antohe, S.; Tugulea, L., ELECTRICAL AND PHOTOVOLTAIC PROPERTIES OF A 2-LAYER ORGANIC PHOTOVOLTAIC CELL. *Physica Status Solidi a-Applied Research* 1991, *128* (1), 253-260.
103. Lee, S. T.; Wang, Y. M.; Hou, X. Y.; Tang, C. W., Interfacial electronic structures in an organic light-emitting diode. *Applied Physics Letters* 1999, *74* (5), 670-672.
104. Farooq, A.; Karimov, K. S.; Ahmed, N.; Ali, T.; Alamgir, M. K.; Usman, M., Copper phthalocyanine and metal free phthalocyanine bulk heterojunction photodetector. *Physica B-Condensed Matter* 2015, *457*, 17-21.
105. Chowdhury, A.; Biswas, B.; Sanyal, M. K.; Mallik, B., Organic Rectifiers Grown from Metal Phthalocyanines Seeds: Effects of Grain Growth and Grain Orientation on the Rectification. *Science of Advanced Materials* 2013, *5* (12), 1857-1866.
106. Farooq, A.; Karimov, K. S.; Wahab, F.; Ali, T.; Abbas, S. Z., Copper phthalocyanine and metal free phthalocyanine bulk heterojunction for temperature sensing. *Journal of Optoelectronics and Advanced Materials* 2015, *17* (5-6), 822-826.
107. Arshak, K.; Arshak, A.; Zleetni, S.; Korostynska, O., Thin and thick films of metal oxides and metal phthalocyanines as gamma radiation dosimeters. *Ieee Transactions on Nuclear Science* 2004, *51* (5), 2250-2255.

108. (a) Li, M. T.; Yang, R. S.; Yu, L. Y., The fiber optic biosensor for noradrenaline concentration detection based on CuPc catalysis. In *Functional Materials and Nanotechnology*, Xu, B.; Li, H. Y., Eds. Trans Tech Publications Ltd: Stafa-Zurich, 2012; Vol. 496, pp 439-442; (b) Mensing, J. P.; Kerdcharoen, T.; Sriprachuabwong, C.; Wisitsoraat, A.; Phokharatkul, D.; Lomas, T.; Tuantranont, A., Facile preparation of graphene-metal phthalocyanine hybrid material by electrolytic exfoliation. *Journal of Materials Chemistry* 2012, 22 (33), 17094-17099.
109. (a) Ostrick, J. R.; Dodabalapur, A.; Torsi, L.; Lovinger, A. J.; Kwock, E. W.; Miller, T. M.; Galvin, M.; Berggren, M.; Katz, H. E., Conductivity-type anisotropy in molecular solids. *Journal of Applied Physics* 1997, 81 (10), 6804-6808; (b) Chowdhury, A.; Biswas, B.; Mallik, B., Effects of Substrate on the Asymmetric Grain Growth and Observation of Conductivity Anisotropy in Nanostructured Organic Thin Films. *Science of Advanced Materials* 2013, 5 (9), 1297-1306.
110. Ashida, M.; Uyeda, N.; Suito, E., UNIT CELL METASTABLE-FORM CONSTANTS OF VARIOUS PHTHALOCYANINES. *Bulletin of the Chemical Society of Japan* 1966, 39 (12), 2616-+.
111. Brown, C. J., CRYSTAL STRUCTURE OF BETA-COPPER PHTHALOCYANINE. *Journal of the Chemical Society a -Inorganic Physical Theoretical* 1968, (10), 2488-&.
112. (a) Xiao, Y.; Li, Y.; Zhang, M.; Wang, F. X.; Pan, G. B., Single-crystal Copper-Phthalocyanine Nanorods Self-assembled by a Solvent Evaporation Method. *Chemistry Letters* 2011, 40 (5), 544-545; (b) Xiao, K.; Li, R. J.; Tao, J.; Payzant, E. A.; Ivanov, I. N.; Puretzky, A. A.; Hu, W. P.; Geohegan, D. B., Metastable Copper-Phthalocyanine Single-Crystal Nanowires and Their Use in Fabricating High-Performance Field-Effect Transistors. *Advanced Functional Materials* 2009, 19 (23), 3776-3780.
113. (a) Padma, N.; Sawant, S. N.; Sen, S.; Gupta, S. K., Effect of post deposition annealing on the performance of copper phthalocyanine based organic thin film transistor. In *Solid State Physics, Vol 57*, Chauhan, A. K.; Murli, C.; Gadkari, S. C., Eds. Amer Inst Physics: Melville, 2013; Vol. 1512, pp 786-787; (b) Berger, O.; Fischer, W. J.; Adolphi, B.; Tierbach, S.; Melev, V.; Schreiber, J., Studies on phase transformations of Cu-phthalocyanine thin films. *Journal of Materials Science-Materials in Electronics* 2000, 11 (4), 331-346; (c) Chintakula, G.; Rajaputra, S.; Singh, V. P., Schottky diodes on nanowires of copper phthalocyanine. *Solar Energy Materials and Solar Cells* 2010, 94 (1), 34-39.

114. Jung, J. S.; Lee, J. W.; Kim, K.; Cho, M. Y.; Jo, S. G.; Joo, J., Rectangular Nanotubes of Copper Phthalocyanine: Application to a Single Nanotube Transistor. *Chemistry of Materials* 2010, 22 (7), 2219-2225.

115. (a) Hassan, A. K.; Gould, R. D., STRUCTURAL STUDIES OF THERMALLY EVAPORATED THIN-FILMS OF COPPER PHTHALOCYANINE. *Physica Status Solidi a-Applied Research* 1992, 132 (1), 91-101; (b) Wang, C. Y.; Cho, C. P.; Perng, T. P., Structural transformation and crystallization of amorphous copper phthalocyanine nanostructures. *Thin Solid Films* 2010, 518 (23), 6720-6728; (c) Basova, T. V.; Kol'tsov, E. K.; Igumenov, I. K., Spectral investigation of interaction of copper phthalocyanine with nitrogen dioxide. *Sensors and Actuators B-Chemical* 2005, 105 (2), 259-265.

116. (a) Liu, S. H.; Wang, W. C. M.; Briseno, A. L.; Mannsfeld, S. C. E.; Bao, Z. N., Controlled Deposition of Crystalline Organic Semiconductors for Field-Effect-Transistor Applications. *Advanced Materials* 2009, 21 (12), 1217-1232; (b) Yang, J. L.; Yan, D. H., Weak epitaxy growth of organic semiconductor thin films. *Chemical Society Reviews* 2009, 38 (9), 2634-2645; (c) Vakhshouri, K.; Kesava, S. V.; Kozub, D. R.; Gomez, E. D., Characterization of the mesoscopic structure in the photoactive layer of organic solar cells: A focused review. *Materials Letters* 2013, 90, 97-102.

117. Bao, Z.; Lovinger, A. J.; Dodabalapur, A., Organic field-effect transistors with high mobility based on copper phthalocyanine. *Applied Physics Letters* 1996, 69 (20), 3066-3068.

118. (a) Farag, A. A. M., Optical absorption studies of copper phthalocyanine thin films. *Optics and Laser Technology* 2007, 39 (4), 728-732; (b) Karan, S.; Mallik, B., Effects of annealing on the morphology and optical property of copper(II) phthalocyanine nanostructured thin films. *Solid State Communications* 2007, 143 (6-7), 289-294; (c) E, J. Y.; Kim, S.; Lim, E. J.; Lee, K. J.; Cha, D. J.; Friedman, B., Effects of substrate temperature on copper(II) phthalocyanine thin films. *Applied Surface Science* 2003, 205 (1-4), 274-279.

119. Liu, F. M.; Sun, J.; Xiao, S.; Huang, W. L.; Tao, S. H.; Zhang, Y.; Gao, Y. L.; Yang, J. L., Controllable fabrication of copper phthalocyanine nanostructure crystals. *Nanotechnology* 2015, 26 (22).

120. Smilgies, D.-M.; Blasini, D. R., Indexation scheme for oriented molecular thin films studied with grazing-incidence reciprocal-space mapping. *Journal of Applied Crystallography* 2007, 40, 716-718.

121. Oura, K. L., V.G.; Saranin, A.A.; Zotov, A.V.; Katayama, M., *Surface Science*. Springer-Verlag Berlin Heidelberg: 2010.

APPENDICES

Appendix A

Simulating GIWAXS Peak Locations

Due to crystal orientation variation as well as polymorphism within organic thin films, it can be challenging to identify and index the reflections observed with GIWAXS measurements. The crystal structure and orientation of a film can be identified from GIWAXS data by implementing a reciprocal-space mapping scheme. By specifying the crystal structure and orientation, GIWAXS reflections can be simulated and compared with the measured data. Using computational methods, the crystal structure and orientation can be perturbed until the simulated reflection locations match the measured GIWAXS data. Even though the theory for calculating the reciprocal-space maps is well known, I could not find an open source program for simulating GIWAXS scattering patterns. Smilges and Blasine¹²⁰ published a derivation for reciprocal-space mapping of thin films measured by GIWAXS in 2007. Although this paper is well written in my opinion, they seemed to have made a mathematical error since I could not reproduce their derivation, nor did it produce reciprocal space maps which agreed with the literature.

I have included my derivation for calculating reciprocal-space maps. The following equations are intended to be easily incorporated by future experiments into any software they wish to use for data analysis. This is the basic math that needs to be programmed to simulate reciprocal-space maps. Those implementing these equations should reference the Smilges and Blasine paper mentioned above as well as Introduction to Solid State Physics by Kittel to understand the theory behind the calculations.

The first step in determining the reciprocal-space scattering peaks is to define the crystal structure you wish to simulate. If the crystal structure is not known, they can be used as input parameters for a guess and check method. For now, assume the crystal structure is known, and follow convention, is described by the lattice vector lengths a , b , c and angles between lattice vectors α , β , γ . The lattice vectors can be express in component form, as shown in the following three equations.

$$\mathbf{A} = [A_x, A_y, A_z] = [a, 0, 0]$$

$$\mathbf{B} = [B_x, B_y, B_z] = [b * \cos(\gamma), b(1 - \cos^2(\gamma))^{\frac{1}{2}}, 0]$$

$$\mathbf{C} = [C_x, C_y, C_z] = [c * \cos(\beta), \frac{b * c * \cos(\alpha) - B_x * C_x}{B_y}, (c^2 + C_y^2 - C_x^2)^{\frac{1}{2}}]$$

Given these lattice vectors, the reciprocal lattice vectors can be calculated using dot products, (\cdot), and cross products, (\times), of the lattice vectors as follows:

$$\mathbf{A}^* = \frac{2 * \pi * \mathbf{B} \times \mathbf{C}}{\mathbf{A} \cdot \mathbf{B} \times \mathbf{C}}$$

$$\mathbf{B}^* = \frac{2 * \pi * \mathbf{C} \times \mathbf{A}}{\mathbf{A} \cdot \mathbf{B} \times \mathbf{C}}$$

$$\mathbf{C}^* = \frac{2 * \pi * \mathbf{A} \times \mathbf{B}}{\mathbf{A} \cdot \mathbf{B} \times \mathbf{C}}$$

Now that the reciprocal lattice vectors are known for the crystal we must specify the orientation of the crystal, conventionally express as (HKL), with respect to the substrate, as shown in the following equation.

$$\mathbf{G}_{HKL} = H * \mathbf{A}^* + K * \mathbf{B}^* + L * \mathbf{C}^*$$

The values for (HKL) must be specified, but if they what you are trying to determine, (HKL) values may also be used as input parameters for a guess and check method. Next we must choose which crystal refraction we are calculating, conventionally described by (h k l), as the reciprocal-space vector in the following equation.

$$\mathbf{g}_{hkl} = h * \mathbf{A}^* + k * \mathbf{B}^* + l * \mathbf{C}^*$$

We can now calculate the location in reciprocal space for a given crystal reflection:

$$q_z = \mathbf{g}_{hkl} \cdot \mathbf{G}_{HKL}$$

$$q_{xy} = ((\mathbf{g}_{hkl} \times \mathbf{G}_{HKL}) \cdot (\mathbf{g}_{hkl} \times \mathbf{G}_{HKL}))^{\frac{1}{2}}$$

Where q_z is perpendicular to the sample substrate, and q_{xy} is parallel to the substrate. If the sample has a specific orientation in the x-y plane, as often occurs with epitaxial growth, q_x

and q_y can be calculated separately as:

$$q_x = \frac{\mathbf{A}^* \cdot \mathbf{g}_{hkl} \times \mathbf{G}_{HKL}}{|\mathbf{A}^*|}$$

$$q_y = \left(\frac{\mathbf{G}_{HKL} \times \mathbf{A}^*}{|\mathbf{A}^*|} \right) \cdot (\mathbf{g}_{hkl} \times \mathbf{G}_{HKL})$$

The calculated q_{xy} and q_z values can then be compared to the peak location measured by GIWAXS. It is important to note that this calculation only determines the location of the reflection peaks, not the intensity of the peaks. Depending on the space group of the crystal, many of the reflection peaks may be forbidden.

Determining the lattice parameters a, b, c, α , β , γ from GIWAXS data would involve extensive guess and check work since there is a continuum of choices for each parameter. I

recommend writing a program to perform the “guess and check” method if the goal is to determine the lattice parameters. If the goal is to determine the crystal orientation, (HKL), for a known crystal structure, a “guess and check” method can be easily by the experimenter. Simply calculate the first ~20 reflections for every combination of (HKL) until you find the one that matches the GIWAXS data. To save time, start with small values of (HKL) first, i.e.

(100),(010)....(110).... etc.

Appendix B

Quantitative correlation of TEY NEXAFS signal composition with C₆₀ dewetting measured by AFM

To ensure the interpretation of the AFM data in Figure 3.1 is in quantitative agreement with the surface composition measured by TEY NEXAFS in figure 3.3, calculations of the TEY NEXAFS signal for the 5 hour and 48 hour annealed samples are estimated. We will assume all C₆₀ molecules in the As-grown sample, as well as residual C₆₀ not incorporated in dewetted mounds in the 5 Hour and 48 Hour annealed samples, form a uniform layer on top of the CuPc, as shown in Figure A1. For the carbon K-edge, the TEY NEXAFS signal is largely due to Auger electrons. We approximate the signal to be due solely to Auger electrons and use analysis methods used for Auger spectroscopy. We note that TEY NEXAFS creates core holes using photons, where electrons are used in Auger spectroscopy. For a quantitative analysis using this method, several further approximations will need to be made. Equations for the Auger signal intensity are given by¹²¹:

$$(1) \quad I_A(\theta) = I_A^\infty \left(\frac{1+r_B}{1+r_A} \right) * \left(1 - e^{-\frac{d}{\lambda_A * \text{Cos}[\theta]}} \right)$$

$$(2) \quad I_B(\theta) = I_B^\infty * e^{-\frac{d}{\lambda_A * \text{Cos}[\theta]}}$$

I_i^∞ is the signal intensity of pure materials, which accounts for molecules having variation in average auger yield per core hole created. Both materials are primarily carbon and have similar density, so we assume $I_A^\infty = I_B^\infty$. We are interested in the ratio of signals which will cause these terms to cancel. Thus, we set $I_A^\infty = I_B^\infty = 1$. The $(1 + r_i)$ terms in

equation (1) are to account for backscatter of incident electrons, which we assume to be similar for both materials allowing us to approximate $r_A = r_B$. For simplicity we will only consider electrons leaving at normal incidence, thus let $\theta = 0$. λ_A is the electron attenuation constant which we must determine. The C_{60} layer thickness is given by d , which is now the only functional dependence remaining in the signal intensity equations.

Equations (1) and (2) now simplify to:

$$(3) \quad I_A(d) = 1 - e^{-\frac{d}{\lambda_A}}$$

$$(4) \quad I_B(d) = e^{-\frac{d}{\lambda_A}}$$

The fraction of the TEY signal from CuPc is given by :

$$(5) \quad \frac{I_B(d)}{I_B(d) + I_A(d)}$$

The C_{60} layer thickness is calculated using the C_{60} Volume deposited = $7.6 \times 10^{-21} m^3$, measured by QCM , and the volume and 2D projected surface area of dewetted C_{60} mounds, measured by AFM. The volume of the dewetted C_{60} mounds is calculated using the measured heights and assuming the mounds are hemispheres. λ_A is calculated from the as-grown data by setting equation 5 equal to the measured CuPc composition by TEY NEXAFS, resulting in $\lambda_A = 1.76 \times 10^{-9} m$. λ_A and the estimated C_{60} layer thickness is then used to estimate the TEY NEXAFS signal for the 5 hour and 48 hour annealed samples, assuming that the dewetted C_{60} mounds have no CuPc signal contribution to the TEY NEXAFS signal. The results are in reasonable agreement with the measured values and are shown in Table B1.

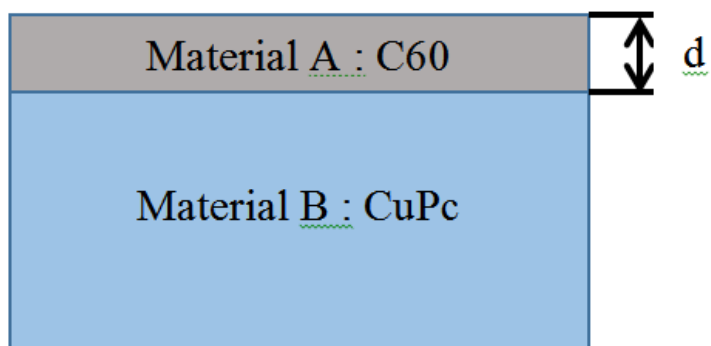


Figure B1 Illustration of Bilayer Film. Illustration of assumed sample geometry in regions not occupied by large dewetted C_{60} mounds

Table B1. Comparison of calculated and measured CuPc component of TEY NEXAFS signal

Sample	Thickness of C ₆₀ wetting layer [nm]	Fraction of Surface Area Covered by dewetted C ₆₀ mounds	Calculated CuPc TEY NEXAFS signal fraction from inter-region (using equation 5)	Calculated Average CuPc TEY NEXAFS signal fraction from the surface	Measured CuPc TEY NEXAFS signal fraction
As-Grown	1.9	0.00	N/A	N/A	0.34
5 Hour anneal	1.6	0.06	.40	0.38	0.38
48 Hour anneal	0.81	0.11	.63	0.56	0.52